University of Alberta

Optical tunneling in metal-dielectric multilayers and its application to optical filters

by

Minchang Zhang

A thesis submitted to the Faculty of Graduate Studies and Research
in partial fulfillment of the requirements for the degree of

Master of Science

in

Microsystems and Nanodevices

Department of Electrical and Computer Engineering

Fall 2013

Edmonton, Alberta

Abstract

Metal-dielectric thin film multilayers are of significant interest as transparent conductors, band-pass filters, and metamaterials. This thesis describes an experimental study of optical tunnelling through periodic metal-dielectric (MD) multilayers with the goal of optimizing the transmittance for either propagating or evanescent waves. Surface-plasmon mediated tunnelling was studied in structures with a symmetric SiO_2-Ag-SiO_2 unit cell. Tunneling of TE-polarized propagating waves was studied in structures with a symmetric TiO_2-Ag-TiO_2 unit cell. In both cases, reasonable agreement between experimental results and theoretical predictions was obtained, indicating that potential transmittance theory and admittance-matching concepts can be used to optimize the transmittance of such structures. However, more predictable and stable results were obtained for the SiO_2-based structures compared to the TiO_2-based structures, which was attributed to oxidation of the Ag layers in the latter case. This motivated a study on alternative termination strategies to improve the peak transmittance of Ag/SiO_2-based multilayers.

Acknowledgements

Finally, this thesis was done with approximately three months of hard work. I am grateful to the help and support that many people have given me throughout my degree. Without you, I would not finish my MSc. degree with rich achievements in two years. If I missed you in this list, please understand that your help was very meaningful to me and was greatly appreciated.

I would like to first and foremost thank my supervisor Dr. Ray DeCorby, for his wise guidance, constructive advice, financial support, hard work and great patience. Your understanding and helping throughout my degree was invaluable and I feel very lucky for being your student.

Thanks to Dr. Trevor Allen, for his strong advice and kindness of never declining the requests for help.

Thanks to all the lab members, past and present, for being kind, easy, and pleasure to work with. Your help and advice were essential to my work. Many thanks to Brian Drobot, Aaron Melnyk, Clinton Potts, Trevor Olsen, Min Choi, Mohammadhossein Bitarafan, Seyed Azmayesh, and Azhruil Islam.

Thanks to Dr. Al Meldrum and his research group for their support and assistance with my work.

Thanks to Don Mullin and Greg Popowich for their enthusiastic assistance and clear guidance for the fabrication of samples.

Thanks to Dr. Robert Fedosejevs and his research group for their generosity of sharing the fume hood and great assistance throughout my research.

Thanks to the Nanofab staff for training me and solving the problems I was facing.

Thanks to the administrative staff for preparing administrative documents and other assistance for my grad studies.

Thanks to all my friends for your accompany and encouragement during my study. Our friendship will last forever.

Finally, thanks to my parents for the support and special encouragements when I was upset and passive. Special thanks to my beautiful girlfriend Yun Peng, who saved me from lonely days, cheered me up when I lost confidence, and made me happy everyday.

Table of Contents

List of Tables

List of Figures

List of Symbols and Abbreviations

Symbols

A	Absorptance
c	Speed of light in vacuum
d_M	Metal layer thickness [nm]
d_f	Film thickness [nm]
E	Electric field [V/m]
E_{out}	Electric field exiting film [V/m]
H	Magnetic field [A/m]
H_{out}	Magnetic field exiting film [A/m]
J	Electric current density [A/m^2]
K	Complex wave number [m^{-1}]
m	Electron mass [kg]
n_c	Complex refractive index
n_{in}	Refractive index of the material at the incoming side
n_{out}	Refractive index of the material at the exiting side
n_M	Refractive index of metal
N_M	Complex refractive index for the absorbing (metal) layer
N	Integer
N	Number of conduction electrons per unit volume [m^{-3}] (Chapter 2)
P	Electric polarization [C/m^2]
q_e	Electron charge [C]
PT	Potential transmittance
PT_{MAX}	Maximum potential transmittance
T	Transmittance

R	Reflectance
X	Displacement of the electrons [m]
X_{op}	Real component of optimal admittance [S]
V	Velocity [m/s]
Y_0	Admittance of free space [S]
Y_{in}	Admittance of input structure [S]
Y_{out}	Admittance of output structure [S]
Y_{op}	Optimal exit admittance [S]
Z_{op}	Imaginary component of optimal admittance [S]
γ	Damping coefficient [s^{-1}]
Γ	Interface toughness [Jm^{-2}]
δ	Skin depth [m]
δ_m	Effective pahse thickness of the metal layer
δ_f	Phase thickness of the film
ε_0	Permitivity of the vacuum [F/m]
η_m	Tilted optical admittance
η_R	Real part of the ‘tilted’ optical admittance
η_I	Imaginary part of the ‘tilted’ optical admittance
θ_2	Incident and exit angle
θ_m	Complex angle of propagation in the absorbing (metal) layer
κ	Extinction coefficient
κ_M	Extinction coefficient of metal
λ	Wavelength [nm]
μ_c	Complex phase thickness of the absorbing (metal) layer
μ_0	Permeability of the vacuum [H/m]

ρ	Net charge density [C/m^3]
σ	Static conductivity [$\Omega^{-1}m^{-1}$]
τ	Relaxation time [s]
ω	Angular frequency [rad/s]
ω_0	Resonant frequency [rad/s]
ω_p	Plasma frequency of metal [rad/s]

Abbreviations

AR	Anti-reflection
ATO	Antimony-doped tin oxide
DMD	Dielectric metal dielectric
FTO	Fluorine-doped tin oxide
IT	Induced-transmission
ITO	Tin-doped indium oxide
LED	Light emitting diode
LD	Lorentz-Drude
MD	Metal dielectric
NIM	Negative index material
PR	Photoriesist
PT	Potential transmittance
SPP	Surface plasmon polariton
TC	Transparent conductor
TE	Transverse electric
TEM	Transmission electron microscopy
TFT	Thin film transistor
TIR	Total internal reflection

TM	Transverse magnetic

Chapter 1 Introduction

This thesis describes an experimental study of optical transmission filters based on periodic, metal-dielectric thin-film stacks. The following sections provide a brief overview on the historical development of optical thin-film filters. Moreover, a brief review of the primary applications for metal-dielectric filters is provided.

1.1 Introduction to optical coatings

Optical coatings are widely used to improve the optical performance of optical and photonic devices. They play an important role in a wide range of applications, from daily consumer goods to state-of-art scientific research. Some examples of daily consumer goods are cell phones, digital cameras, CDs and DVDs, thin-film transistor (TFT) LCD displays, eyeglasses and sunglasses, light-emitting diodes (LEDs), solar cells, and smart windows. For scientific research, some examples include fluorescence analysis, plasmonics and biosensors, lasers, nonlinear optics, laser fusion, nanotechnologies, optical filters and metamaterials. The spectral ranges of interest span from the far-infrared to the soft X-ray region. In our research, we focus on thin-film coatings such as antireflection coatings, transparent conductive coatings, and optical filters [1].

Many of the fabrication techniques for thin-film coatings were developed for the needs of best performance in optics and photonics. Macleod [2] described some aspects of progress in coatings from the early days of the 16th Century to the present day, along with some current demanding applications and discussion of the latest innovations. He also outlined the important events in the development of optical coatings [3]. Challenging requirements arose from both consumer needs and scientific research interests, and continue to drive the research of thin-film optical coatings.

The systematic research in optical thin films started when Isaac Newton explained the so-called ‘Newton rings’ in the early 1700s. However, the theory of thin films was not established until the wave characteristic of light was demonstrated by Thomas Young's double slit experiment in 1801. Based on the wave theory, Fresnel derived the coefficients (widely known as Fresnel coefficient) that quantify the reflection at a boundary between two media in 1821. In addition, he and Poisson derived the condition for the quarter-wave antireflection coating [2]. Antireflection coatings can be applied to the elements of optical instruments such as optical lenses. Furthermore, quarter-wave stack is the basic structure for high reflection mirrors and laser cavity mirrors, due to the fact that it provides the highest and broadest reflection zone. Plus, the quarter-wave stack used as admittance matching assembly for induced transmission design is further introduced in Chapter 4.

1.2 Metal-dielectric multilayer coatings

Compared to conventional all-dielectric multilayers, metal-dielectric (MD) multilayers offer several distinct features.

1. MD multilayers are able to give better out of band rejection over a large spectral range due to the large difference in permittivity between metals and dielectrics [4, 5]. In particular, metals are characterized by highly dispersive optical constants, especially near their plasma frequency. For example, in the design of a long-wavelength cutoff filter, the rejection on the long-wavelength side can be extended beyond 20 μm, which is mostly due to the high reflection of Ag in this range, and to a less extent due to the absorption in the Ag [6].
2. In MD multilayers, the oscillating electrons within a metal may couple to photons at a planar metal-dielectric surface, creating so-called surface-plasmon

plaritons (SPPs), leading to electromagnetic fields confined to the metallic surface [7, 8]. SPPs are widely used in the design of the so-called 'superlens', in which the evanescent waves can propagate through the superlens and thus create a sub-diffraction image.

3. MD multilayers enable designs in which the transmittance and reflectance are independently controlled. This is not possible with all-dielectric filters since in that case T + R = 1 for every wavelength. With absorbing layers introduced, however, the fact that T + R + A = 1 allows for an extra degree of freedom, so that low transmittance and low reflectance can be achieved simultaneously. Several applications such as 'one-way mirrored' sunglasses were given [9, 10, 11] in the literature based on the absorptive feature of the metal layer in the metal-dielectric filters.

In the following sub-sections, a brief overview of some historical applications for MD stacks is provided.

1.2.1 Thermal windows

Thermal windows, otherwise known as heat-reflecting coatings or simply heat mirrors, are widely used in thermophotovoltaic designs for solar cells. It is known that the efficiency of a solar cell is strongly dependent on the operating temperature [12]. A spectral separation between solar radiation and the thermal radiation emitted by objects can greatly increase the efficiency. By blocking (i.e. absorbing or reflecting) the IR portion of the spectrum, the solar cell can operate at low temperature while thermal energy from the IR spectrum can be diverted to another device and converted into electrical energy (i.e. using generators such as a steam turbine). The basic functionality is shown in Figure 1.1. MD multilayers can satisfy the needs for the visible bands. The

metallic layer plays the part of a heat-reflection layer and it must be thick enough to reflect the IR radiation, while the dielectric layers are acting as a matching or antireflection coatings for visible band light. This structure gives high transmission in the visible region while providing high reflection for wavelengths longer than the visible region [13]. For instance, Figure 1.2 shows an example of a three-layer DMD stack designed as a transparent heat mirror.

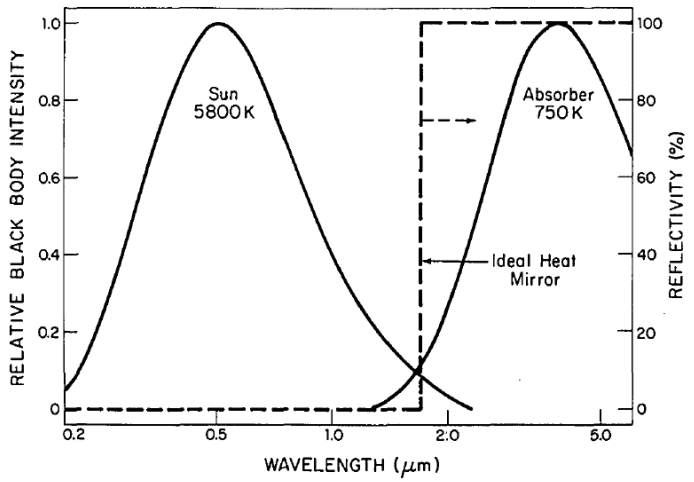

Figure 1.1 Black body radiation curves representing the sun at 5800 K and an absorber at 750 K (i.e. temperature assumed to achieve reasonable thermal-electric conversion efficiency). The dashed line shows the reflectivity of an ideal heat mirror that is able to block the heat from IR radiation and pass the visible light [14].

1.2.2 Transparent conductors

Transparent conductors (TCs) are typically required to provide high optical transparency in the visible region, and of course high electrical conductivity. Traditionally, TCs have been made using wide band gap (greater than 3 eV), non-stoichiometric oxides such as antimony-doped tin oxide (ATO), fluorine-doped tin oxide (FTO), and tin-doped indium oxide (ITO). However, these oxides have problems such as scarcity of supply [15], high resistivities (three orders of magnitude larger than those for metals) [16], and a ceramic nature (i.e. brittle, easily damaged films) [17].

Transparent conductors made of MD multilayers can be designed to have high transmission comparable with ITO conductors, while offering low electrical resistance and high durability. For example, a design similar to Figure 1.2 (i.e. 2.5 periods of Ag/MgF_2) was measured to have a sheet resistance of 0.2 ohms/sq. compared with 250 ohms/sq. for the ITO films [16]. This builds on the pioneering work of Berning and Turner [18], who proposed the potential transmittance theory to show that higher transmittance for a given total thickness of metal is possible when the metal is stratified with proper spacer layers. This theory is valid for both propagating [16] and evanescent [19] waves, and is further discussed in Chapters 2 – 5. Such ability to enhance transmission of light through metals is the foundation for MD-stack-based TCs, facilitating their use in solar cells, smart windows, electrodes for displays, and TC coatings [13].

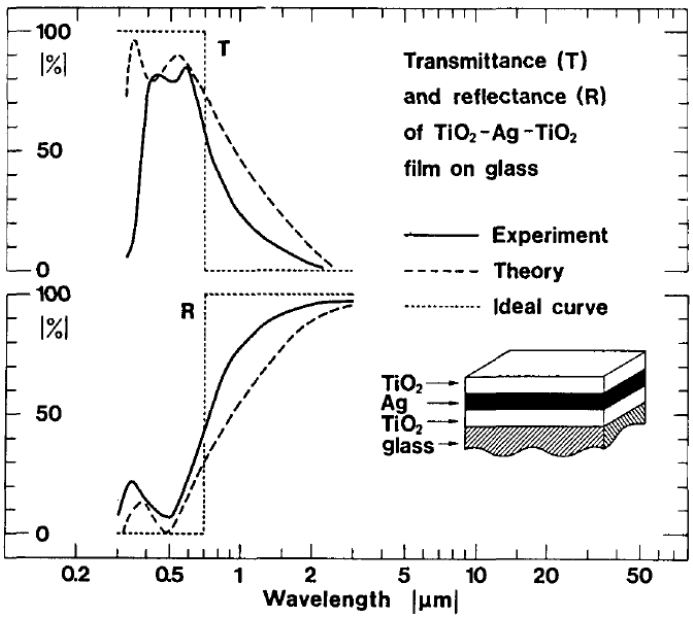

Figure 1.2 Predicted and measured transmittance and reflectance of a $TiO_2/Ag/TiO_2$ multilayer thin film designed as a transparent heat mirror [20].

1.2.3 Superlens and hyperlens

The concept of a 'superlens' (and in the ideal limit, the perfect lens) was first suggested by Pendry [21], who predicted that the negative-index-material (NIM) based superlens can have a resolution beyond the diffraction limit. Unlike conventional lenses, which are able to transmit only propagating waves and thereby suffer from the diffraction limit due to a fast exponential decay of evanescent wave components, a superlens can capture evanescent waves [21] from an object and transmit them to the image plane. The superlens thus can enable resolution below the conventional diffraction limit. Subsequent experimental verification of superlenses was reported both at microwave frequencies [22] and at terahertz and infrared frequencies [23]. However, since the superlens only works in the near-field, the concept of a hyperlens was subsequently introduced independently [24, 25] for far-field performance.

In the near field, since the electric and magnetic responses of materials are decoupled, only the permittivity needs to be considered for transverse magnetic (TM) waves [21]. Therefore, silver and other noble metals are good candidates for superlensing since they inherently provide a negative (real part of) permittivity in the frequency range below their plasma frequency [26]. The thin metal layer is designed such that the permittivity of the metal film and that of the adjacent medium are equal and of opposite sign. Thus, evanescent waves from the object are able to resonantly excite SPPs, and are thereby transferred to the opposite side of the metal film. By using sub-wavelength sheets of silver, near-field focusing for TM-polarized light was obtained and illustrated by Zhang *et al.* [26] (see Figure 1.3). In addition, Zhang also showed that the silver superlens can image arbitrary nanostructures with sub-diffraction-limited resolution. For example, the fine features from the mask shown in Figure 1.4 (A) could be reproduced (see Figure 1.4 (B)) with good fidelity.

A drawback to the superlens is that it does not support magnification of subwavelength features into the farfield. In order to project a sub-diffraction-limited image into the far field, a magnifying superlens, also known as hyperlens, was proposed to be constructed by using cylindrical metamaterials [27, 28] (see Figure 1.5). The metamaterial was designed such that the radial and tangential permittivities have different signs to enable evanescent waves to propagate along the radial direction of the MD stack [29, 30, 31]. A magnified image was thus produced at the outer boundary of the hyperlens due to the conservation of angular momentum [29, 32]. Once all the components are converted to propagating waves (i.e. magnified feature is larger than the diffraction limit), a conventional lens can be used for imaging in the far field.

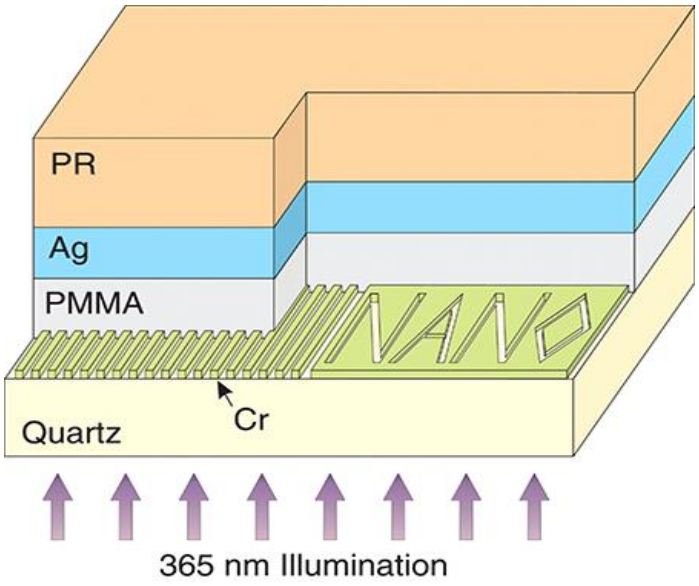

Figure 1.3 Optical superlensing experiment to image the embedded objects inscribed onto the chrome (Cr) to the photoresist (PR) on the other side of the silver superlens. [26]

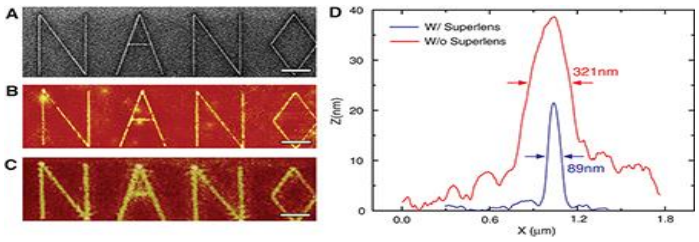

Figure 1.4 Superlensing experiment for an arbitrary object "NANO" with a silver superlens (B) compare to the focused ion beam (FIB) lithography image of the object (A) and a control experiment without superlens (C). (D) A comparison of the exposed line width for the averaged cross section of letter "A" between the image taken with the superlens (blue line) and without the superlens (red line). [26]

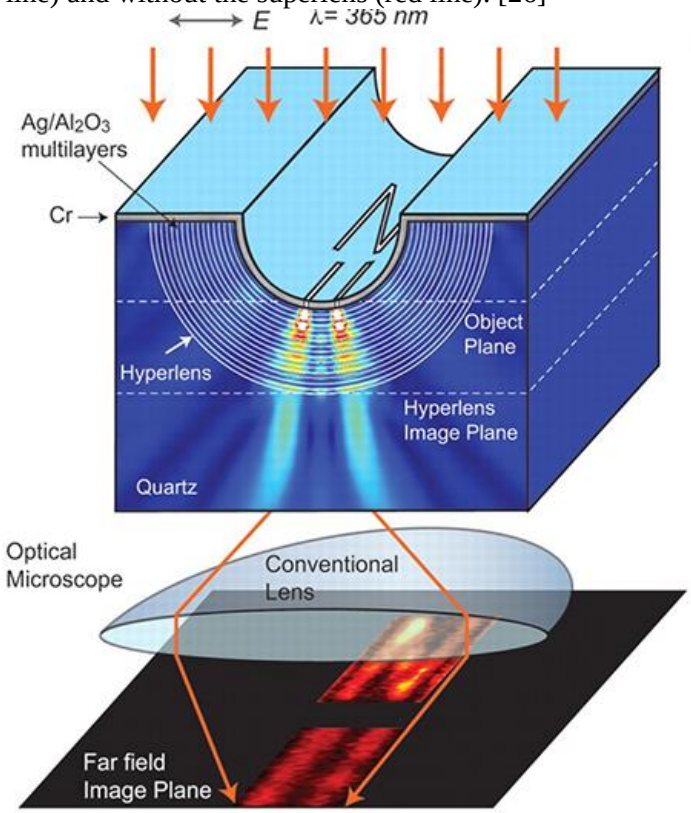

Figure 1.5 Schematic illustration for a hyperlens and numerical simulation of an image from sub-diffraction-limited objects. [33]

1.3 Outline of Thesis

This thesis focuses on the experimental examination of optical properties of DMD multilayer samples for both propagating and evanescent waves. It also provides some insights into the potential applications of the DMD structures for optical filtering.

Chapter 1 briefly introduces the historical progress of optical coatings, including some notable developments. Furthermore, it provides an overview of the historical development and applications of metal-dielectric multilayer coatings.

Chapter 2 provides some pertinent background theory and a description of sample fabrication techniques, to facilitate the following chapters. This begins with a discussion of the potential transmittance theory and conditions for admittance-matched tunneling. Since the optical properties of metals are critical to the optical performance of these samples, an overview of the optical properties of metals is given, along with the discussion of some Ag models used in Chapters 3, 4, and 5. Furthermore, this chapter describes the deposition techniques and the materials used for the fabrication of these samples.

Chapters 3 and 4 describe experimental studies of periodic DMD multilayers designed using the theories detailed in Chapter 2. Based on the conditions that match the admittance of the DMD stack to an ambient medium, we designed and fabricated samples to achieve the maximum transmittance of light through the multilayers. Samples were prepared for both TE and TM polarized incident light, and for either propagating or evanescent waves.

Chapter 5 describes an experimental study for the design of a DMD stack that enables TE-polarized incident light to tunnel through a potential barrier. Furthermore, such design was investigated for modifying the spontaneous emission from different types of fluorescent dyes. This latter work is potentially applicable to fluorescence biosensors.

Chapter 6 summarizes the design steps and fabrication techniques used to realize the target DMD multilayers, and provides conclusions regarding the optical performance of the samples. Some speculation on possible future work is also presented.

References

[1] T. W. Allen and R. G. DeCorby, "Conditions for admittance-matched tunneling through symmetric metal-dielectric stacks," *Optics Express*, vol. 20, no. 55, pp. A578-A588, (2012).

[2] H. A. Macleod, "Progress in optical coatings," *Proc.SPIE*, vol. 7107, p. 710102, (2008).

[3] H. A. Macleod, "Optical coating today," in *International Photonics Conference*, 8-10 December 2011.

[4] S. H. Fan, P. R. Villeneuve and J. D. Joannopoulos, "Large omnidirectional band gaps in metallodielectric photonic crystals," *Phys. Rev. B*, vol. 54, pp. 11245-11251, (1996).

[5] J. G. Fleming, S. Y. Lin, I. El-Kady, R. Biswas and K. M. Ho, "All-metallic three-dimensional photonic crystals with a large infrared bandgap," *Nature*, vol. 417, pp. 52-55, (2002).

[6] P. Ma, F. Lin and J. A. Dobrowolski, "Design and manufacture of metal/dielectric long-wavelength cutoff filters," *Applied Optics*, vol. 50, no. 9, pp. C201-C209, (2011).

[7] T. W. Oates, H. Wormeester and H. Arwin, "Characterization of plasmonic effects in thin films and metamaterials using spectroscopic ellipsometry," *Progress in Surface Science*, vol. 86, pp. 328-376, (2011).

[8] S. A. Maier and H. A. Atwater, "Plasmonics: Localization and guiding of electromagnetic energy in metal/dielectric structures," *J. Appl. Phys.*, vol. 98, p.

011101, (2005).

[9] J. A. Dobrowolski, L. Li and R. A. Kemp, "Metal/dielectric transmission interference filters with low reflectance. 1. Design," *Applied Optics,* vol. 34, no. 25, pp. 5673-5683, (1995).

[10] B. T. Sullivan and K. L. Byrt, "Metal/dielectric transmission interference filters with low reflectance. 2. Experimental results," *Applied Optics,* vol. 34, no. 25, pp. 5684-5694, (1995).

[11] F. Lemarquis and G. Marchand, "Analytical Achromatic Design of Metal–Dielectric Absorbers," *Applied Optics,* vol. 38, no. 22, pp. 4876-4884, (1999).

[12] F. Demichelis, E. Minetti-Mezzetti and V. Perotto, "Optical studies of multilayer dielectric-metal-dielectric coatings as applied to solar cells," *Solar Cells,* vol. 6, pp. 323-333, (1982).

[13] C. C. Granqvist, "Transparent conductors as solar energy materials: A panoramic review," in *Solar Energy Materials & Solar Cells*, (2007).

[14] J. C. Fan and F. Bachner, "Transparent heat mirrors for solar-energy applications," *Applied Optics,* vol. 15, pp. 1012-1017, (1976).

[15] D. S. Hecht, L. Hu and G. Irvin, "Emerging Transparent Electrodes Based on Thin Films of Carbon Nanotubes, Graphene, and Metallic Nanostructures," *Adv. Mater.,* vol. 23, p. 1482–1513, (2011).

[16] M. J. Bolemer and M. Scalora, "Transmissive properties of Ag/MgF_2 photonic band gaps," *Appl. Phys. Lett.,* vol. 72, pp. 1676-1678, (1998).

[17] D. R. Cairns, R. P. Witte, D. K. Sparacin, S. M. Sachsman, D. C. Paine, G. P. Crawford and R. R. Newton, "Strain-dependent electrical resistance of tin-doped

indium oxide on polymer substrates," *Appl. Phys. Lett.,* vol. 76, p. 1425, (2000).

[18] P. H. Berning and A. F. Turner, "Induced transmission in absorbing films applied to band pass filter design," *J. Opt. Soc. Am.,* vol. 47, pp. 230-239, (1957).

[19] S. A. Ramakrishna, J. B. Pendry, M. C. Wiltshire and W. J. Stewart, "Imaging the near field," *J. Mod. Opt.,* vol. 50, pp. 1419-1430, (2003).

[20] C. C. Granqvist, "Radiative heating and cooling with spectrally selective surfaces," *Applied Optics,* vol. 20, pp. 2606-2615, (1981).

[21] J. B. Pendry, "Negative refraction makes a perfect lens," *Phys. Rev. Lett.,* vol. 85, pp. 3966-3969, (2000).

[22] M. C. Wiltshire, J. B. Pendry, I. R. Young, D. J. Larkman, D. J. Gilderdale and J. V. Hajnal, "Microstructured Magnetic Materials for RF Flux Guides in Magnetic Resonance Imaging," *Science,* vol. 291, pp. 849-851, (2001).

[23] T. J. Yen, W. J. Padilla, N. Fang, D. C. Vier, D. R. Smith, J. B. Pendry, D. N. Basov and X. Zhang, "Terahertz Magnetic Response from Artificial Materials," *Science,* vol. 303, pp. 1494-1496, (2004).

[24] Z. Jacob, L. V. Alekseyev and E. Narimanov, "Optical Hyperlens: Far-field imaging beyond the diffraction limit," *Optical Express,* vol. 14, pp. 8247-8256, (2006).

[25] A. Salandrino and N. Engheta, "Far-field subdiffraction optical microscopy using metamaterial crystals: Theory and simulations," *Phys. Rev. B,* vol. 74, p. 075103, (2006).

[26] N. Fang, H. Lee, C. Sun and X. Zhang, "Sub–Diffraction-Limited Optical Imaging with a Silver Superlens," *Science,* vol. 308, pp. 534-537, (2005).

[27] J. B. Pendry and S. A. Ramakrishna, "Near-field lenses in two dimensions," *J. Phys.*

Condens. Matter, vol. 14, p. 8463, (2002).

[28] J. B. Pendry, "Perfect cylindrical lenses," *Optics Express*, vol. 11, pp. 755-760, (2003).

[29] V. A. Podolskiy and E. E. Narimanov, "Strongly anisotropic waveguide as a nonmagnetic left-handed system," *Phys. Rev. B*, vol. 71, pp. 201101(R)-1-4, (2005).

[30] V. A. Podolskiy, L. Alekseyev and E. E. Narimanov, "Strongly anisotropic media: the THz perspectives of left-handed materials," *J. Mod. Opt.*, vol. 52, p. 2343, (2005).

[31] R. Wangberg, J. Elser, E. E. Narimanov and V. A. Podolskiy, "Non-magnetic nano-composites for optical and infrared negative refraction index media," *J. Opt. Soc. Am. B.*, vol. 23, p. 498, (2006).

[32] A. A. Govyadinov and V. A. Podolskiy, "Metamaterials photonic funnels for sub-diffraction light compression and propagation," *Phys. Rev. B*, vol. 73, p. 155108, (2006).

[33] Z. Liu, H. Lee, Y. Xiong, C. Sun and X. Zhang, "Far-Field Optical Hyperlens Magnifying Sub-Diffraction-Limited Objects," *Science*, vol. 315, p. 1686, (2007).

Chapter 2 Theory

This chapter describes the previously mentioned PT theory, as well as conditions for admittance-matched tunneling through DMD multilayers. It also contains a brief introduction to optical properties of metals and a discussion of different Ag models used in the subsequent chapters.

2.1 PT Theory

Metal-dielectric (MD) multilayers have been extensively studied during the past decade. This interest is driven by the unique optical properties of metals, especially near the plasma frequency of a given metal. For propagating waves inside the dielectric layers, the MD stack functions as a series of coupled Fabry-Perot cavities. This type of structure is studied for use as transparent conductors [1] and nonlinear media [2]. For propagation of evanescent waves through MD stacks, the waves are transferred by excitation of coupled surface-plasmon resonances at the MD boundaries [3, 4]. This phenomena is widely explored for metamaterial and superlens [5] applications.

For both propagating [1] and evanescent [6] waves and for an arbitrary total thickness of metal, it has been shown that higher transmittance is possible when the metal is subdivided into a series of thin films. This fact was explained by Berning and Turner in 1957 [7], as part of their potential transmittance (PT) theory. PT theory indicates that low transmittance for a thin metal film is mainly caused by an admittance mismatch between the film and the surrounding media, instead of absorption by the metal. More recently, Bloemer *et al.* [1] showed that MD stacks can have a high transmission band in the visible region and remain opaque for all other frequencies. The opacity is thus mainly caused by an admittance mismatch between the incident medium and the multilayer. Similarly, high transmittance can be viewed as a band-limited admittance-matching

condition, determined by a particular combination of refractive indices and thicknesses of the dielectric layers separating the adjacent metal layers. Therefore, the maximum PT for a given metal film can be achieved by adding appropriate admittance-matching assemblies to the entrance and exit media of the film.

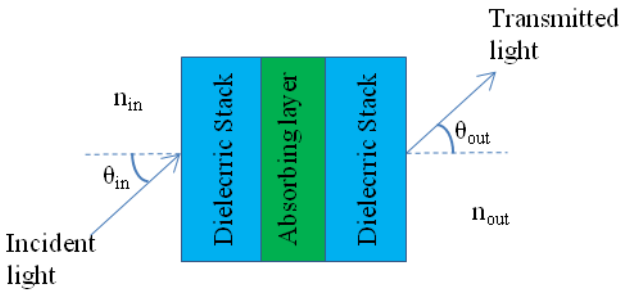

Figure 2.1 Schematic illustration of a stack containing one absorbing layer, bounded by dielectric matching layers. θ_{in} is the incident angle and θ_{out} is the exit angle, n_{in} is the refractive index of the material at the incoming side, and n_{out} is the refractive index of the material at the exiting side.

For a multilayer containing an absorbing layer (or multiple absorbing layers), as illustrated in Figure 2.1, *PT* is defined as the ratio of the transmitted intensity to the intensity entering the front surface:

$$PT = \frac{T}{1-R} = \frac{T}{T+A}, \tag{2.1}$$

where *T*, *R*, and *A* are the transmittance, reflectance, and absorbance of the layer, respectively. For a perfect reflectionless case (i.e. $R = 0$), the transmittance is equal to the *PT*. Equation (2.1) shows that *PT* is independent of reflections at the front surfaces (i.e. *R*) and therefore is determined solely by the properties of the absorbing layer and the exit media. For a given absorbing layer, *PT* has an upper limit (PT_{MAX}), useful for assessing the transparency of MD stacks. $PT = PT_{MAX}$ corresponds to conditions of minimum possible absorption by the lossy layer. PT_{MAX} is attained by properly matching the admittance of the exit layer to the absorbing layer [8, 7, 9, 10, 11] to reduce the

reflectance (i.e. for incidence from the right) to zero. A generalized expression for PT_{MAX} that allows for arbitrary values of the in-plane wave vector is as follows [12]:

$$PT_{MAX} = \sigma - (\sigma^2 - 1)^{\frac{1}{2}}, \tag{2.2}$$

where

$$\sigma = \frac{\cosh(2\mu_i) + \Gamma^2 \cos(2\mu_r)}{1 + \Gamma^2}. \tag{2.3}$$

For TE- and TM-polarized waves, Γ is unique and is given as:

$$\begin{cases} \Gamma_{TE} = \dfrac{\mathrm{Im}(N_M b)}{\mathrm{Re}(N_M b)} & [\mathrm{TE}] \\ \Gamma_{TM} = \dfrac{\mathrm{Im}(N_M / b)}{\mathrm{Re}(N_M / b)} & [\mathrm{TM}] \end{cases}, \tag{2.4}$$

where $b = \cos(\theta_M)$, θ_M is the complex angle of propagation in the absorbing (metal) layer, and $N_M = n_M - i\kappa_M$ is the complex refractive index for the absorbing (metal) layer. The complex phase thickness of the absorbing (metal) layer is defined as:

$$\delta_m = \mu_r + i\mu_i = \left(\frac{2\pi}{\lambda}\right) N_M d_M \cos(\theta_M), \tag{2.5}$$

where d_M is the metal thickness.

For a layered sequence of N absorbing films with PT_1, PT_2,…,PT_N, the overall PT is the product of that for each film [12], i.e. $PT_{total} = PT_1 \cdot PT_2 \cdot \ldots PT_N$, and it follows the same way for PT_{MAX}. Therefore, the PT_{MAX} of a multilayer can be predicted based on each of the absorbing layers within the structure. Consequently, the transmittance of the multilayer depends on the properties of the media (refractive index, thickness, and order of layers) surrounding the absorbing layers. In order to obtain a maximum transmittance (i.e. $T = PT_{MAX}$), the system containing absorbing layers must be perfectly anti-reflection

coated for both left and right incidence (i.e. the system is optimally admittance matched to both the incident and exit media).

2.2 Conditions for admittance-matched tunneling

It is assumed in all case below that the bulk refractive index $N_m = n_m - i\kappa_m$ for a metal remains valid when describing the optical properties of the thin metal film [13]. However, for very thin metal films, optical properties that are different than the bulk values are usually expected due to electron scattering at grain boundaries or quantum confinement effects. Since the minimum thickness of Ag films to exhibit bulk properties was reported to be about 10 - 12 nm [14, 15], we assume that the films with thickness greater than 10 nm can still exhibit bulk properties for our theoretical analysis.

The aforementioned potential transmittance ($PT = T/(1-R)$) of an arbitrary single absorbing film depends both on its properties and on the exit optical admittance (Y_{out}). The exit admittance determines the ratio of the magnetic to electric field on the exit side of the absorbing layer ($Y_{out} = H_{out}/E_{out}$). In order to achieve PT_{MAX}, the exit admittance (Y_{out}) should be set to an optimal value $Y_{op} = X_{op}+iZ_{op}$. As previously reported [16], the closed-form expressions for X_{op} and Z_{op} for non-normal incidence are given as follows:

$$X_{op} = \left(\frac{\left(\eta_R^2 + \eta_I^2\right)\left(\eta_R \sinh\beta\cosh\beta + \eta_I \sin\alpha\cos\alpha\right)}{\left(\eta_R \sinh\beta\cosh\beta - \eta_I \sin\alpha\cos\alpha\right)} - \frac{\eta_R^2\eta_I^2\left(\sin^2\alpha\cosh^2\beta + \cos^2\alpha\sinh^2\beta\right)^2}{\left(\eta_R \sinh\beta\cosh\beta - \eta_I \sin\alpha\cos\alpha\right)^2} \right)^{1/2}$$
$$Z_{op} = \frac{\eta_R\eta_I\left(\sin^2\alpha\cosh^2\beta + \cos^2\alpha\sinh^2\beta\right)}{\left(\eta_R \sinh\beta\cosh\beta - \eta_I \sin\alpha\cos\alpha\right)}, \qquad (2.6)$$

where η_R and η_I are real and imaginary parts of the 'tilted' optical admittance (η_m) [10] of the metal layer. η_m is unique for TE and TM polarization and is defined as follows:

$$\eta_m = \eta_R - i\eta_I = \begin{cases} (n_m - i\kappa_m)\cdot\cos\theta_m & [\text{TE}] \\ (n_m - i\kappa_m)/\cos\theta_m & [\text{TM}] \end{cases}, \tag{2.7}$$

where θ_m is the complex angle for light inside the metal layer, as predicted by Snell's law. A and β are defined based on the effective phase thickness (i.e. see equation (2.5)) as follows:

$$\alpha - i\beta = \left(\frac{2\pi}{\lambda}\right)(n_m - i\kappa_m)d_m\cos\theta_m. \tag{2.8}$$

Since $PT=PT_{MAX}$ occurs when $Y_{out}=Y_{op}$ and $T=PT_{MAX}$ ($R=0$) occurs when $Y_{in}=Y_{op}$, it follows that in order to achieve PT_{MAX} we must designate the conditions when $Y_{in}=Y_{out}=Y_{op}$ is obtained for a given periodic DMD multilayer.

Consider a symmetric DMD unit cell surrounded by media with refractive index n_1. In our earlier work [16], we found that conditions (i.e. particular combinations of λ, n_1, d_1, N_m, d_m, n_2, and θ_2) for attaining the maximum transmittance (i.e. $T=PT_{MAX}$) are identical regardless of whether the structure is a unit cell or a periodic multilayer based on that unit cell. The admittance matching equation is described as follows:

$$X_{op} = \frac{2\eta_2}{\pm\cos\left[\sin^{-1}\left\{\dfrac{2Z_{op}}{X_{op}(\eta_1/\eta_2 - \eta_2/\eta_1)}\right\}\right]\left(1-\dfrac{\eta_2^2}{\eta_1^2}\right)+\left(1+\dfrac{\eta_2^2}{\eta_1^2}\right)}. \tag{2.9}$$

η_1 and η_2, defined as $\eta_i = n_i\cos\theta_i$ for TE polarization and $\eta_i = n_i/\cos\theta_i$ for TM polarization, represent the tilted optical admittances of the dielectric layer and the ambient medium, respectively. n_i is the refractive index of medium i, while θ_i is the propagation angle (from Snell's law) in medium i. As reported [16], the modifier (+/-) in the denominator of equation (2.9) is a result of the two-argument feature of the arcsine. Note that X_{op}, Z_{op}, and η_2 are all real numbers for all cases considered in this thesis (i.e. lossless ambient media with real incident angle for both TE and TM polarized light).

With the solution from equation (2.9), the thickness of the dielectric layer n_1 that enables the admittance match can be calculated as follows [16]:

$$d_{1,m} = \left(\frac{\lambda}{4\pi n_1 \cos\theta_{1,m}} \right) \sin^{-1} \left\{ \frac{2Z_{op}}{X_{op}\left(\eta_{1,m}/\eta_{2,m} - \eta_{2,m}/\eta_{1,m}\right)} \right\}. \tag{2.10}$$

2.3 Optical properties of metals

2.3.1 Introduction

Since light is electromagnetic radiation, the study of optical properties of metals is mainly the study of how these fields interact with or travel inside metals. In most metals, optical properties are determined mainly by the motion of 'free' carriers (which are also responsible for conductivity) under the driving force of the electric field. Conductivity is a frequency dependent parameter due to the inertia of conduction electrons. Therefore, the index of refraction for metals predicts different characteristics for wave propagation at different frequencies. To further illustrate, let us start from fundamental theory with the Maxwell equations for a medium:

$$\begin{cases} \nabla \times \mathbf{H} = \mathbf{J} + \varepsilon_0 \dfrac{\partial \mathbf{E}}{\partial t} + \dfrac{\partial \mathbf{P}}{\partial t} \\ \nabla \times \mathbf{E} = -\mu_0 \dfrac{\partial \mathbf{H}}{\partial t} \\ \nabla \bullet \mathbf{E} = \dfrac{\rho}{\varepsilon_0} \\ \nabla \bullet \mathbf{H} = 0 \end{cases}, \tag{2.11}$$

where **J** is the electric current density, **E** is the electric field, **H** is the magnetic field, **P** is the electric polarization, μ_0 is the permeability of the vacuum, ε_0 is the permittivity of the vacuum, and ρ is the net charge density. By taking the curl of Ampere's law and Faraday's law and using vector identities, after some algebraic manipulation, the general wave equation is derived:

$$\nabla^2\mathbf{E} = \frac{1}{c^2}\frac{\partial^2\mathbf{E}}{\partial t^2} + \mu_0\frac{\partial^2\mathbf{P}}{\partial t^2} + \mu_0\frac{\partial\mathbf{J}}{\partial t}, \tag{2.12}$$

where c is the speed of light in vacuum. Since the medium response in metals is dominated by conduction electrons, the polarization term is dropped and the general wave equation is reduced to

$$\nabla^2\mathbf{E} = \frac{1}{c^2}\frac{\partial^2\mathbf{E}}{\partial t^2} + \mu_0\frac{\partial\mathbf{J}}{\partial t}. \tag{2.13}$$

Now, consider a uniform electric field **E** with linear polarization. In this field, electrons are modeled as harmonic oscillators (i.e. as if they were bound to an equilibrium position by a quasi-elastic restoring force **F**). Then the equation of motion of the electrons is

$$\mathbf{F} = -q_e\mathbf{E} = m\left(\frac{\partial^2\mathbf{X}}{\partial t^2} + \gamma\frac{\partial\mathbf{X}}{\partial t} + \omega_0^2\mathbf{X}\right), \tag{2.14}$$

where m is the electron mass, **X** is the displacement of the electrons, γ is the damping coefficient, ω_0 is the resonant frequency, and q_e is the electron charge. There are two types of electrons in an arbitrary material inside an electric field: free electrons that conduct current, and electrons that are bound to a particular atomic site. For free electrons, $\omega_0 = 0$ because there is no restoring force, so the above equation reduces to

$$-q_e\mathbf{E} = m\left(\frac{\partial^2\mathbf{X}}{\partial t^2} + \gamma\frac{\partial\mathbf{X}}{\partial t}\right). \tag{2.15}$$

When free electrons start to move, they conduct current. Each of the oscillating electrons contributes a current equal to its charge $-q_e$, times its velocity **V**. With N such electrons per unit volume, the current density **J** is

$$\mathbf{J} = Nq_e\mathbf{V}. \tag{2.16}$$

Taking the derivative with respect to time on both sides of the above equation gives us

$$\frac{\partial \mathbf{J}}{\partial t} = Nq_e \frac{\partial \mathbf{V}}{\partial t}. \tag{2.17}$$

Since we know that **V** = d**X**/dt, we can substitute equation (2.17) into equation (2.15) and simplify to get

$$\frac{\partial \mathbf{J}}{\partial t} + \gamma \mathbf{J} = \frac{Nq_e^2}{m} \mathbf{E}. \tag{2.18}$$

Assume a harmonic time dependence for the driving **E** field (i.e. **E** = **E**$e^{i\omega t}$). The above equation becomes

$$(i\omega + \gamma)\mathbf{J} = \frac{Nq_e^2}{m} \mathbf{E}, \tag{2.19}$$

which gives a dynamic general expression for **J**:

$$\mathbf{J} = \frac{Nq_e^2}{m} \frac{1}{i\omega + \gamma} \mathbf{E}. \tag{2.20}$$

Since γ is equal to the inverse of the relaxation time τ, which is the average time between collisions of free electrons, and by introducing the static conductivity σ as

$$\sigma = \frac{Nq_e^2}{m} \tau, \tag{2.21}$$

equation (2.20) is further reduced to

$$\mathbf{J} = \frac{\sigma}{1 + i\omega\tau} \mathbf{E}. \tag{2.22}$$

Substituting equation (2.22) into equation (2.13), we obtain

$$\nabla^2 \mathbf{E} = \frac{1}{c^2} \frac{\partial^2 \mathbf{E}}{\partial t^2} + \frac{\mu_0 \sigma}{1 + i\omega\tau} \frac{\partial \mathbf{E}}{\partial t}. \tag{2.23}$$

This equation has homogeneous plane wave solutions of the form:

$$\mathbf{E} = \mathbf{E_0} e^{i(\omega t - Kz)}, \tag{2.24}$$

where the complex wave number *K* is given as:

$$K^2 = \frac{\omega^2}{c^2} - \frac{i\omega\mu_0\sigma}{1+i\omega\tau}. \tag{2.25}$$

Since $K = k_0 \cdot n_c = \omega/c \cdot n_c$, the complex refractive index n_c is given as

$$n_c^2 = 1 - \frac{c^2}{\omega}\frac{i\mu_0\sigma}{1+i\omega\tau}. \tag{2.26}$$

The speed of light c in vacuum can be expressed as:

$$c = \frac{1}{\sqrt{\varepsilon_0\mu_0}}. \tag{2.27}$$

If we substitute equation (2.27) into equation (2.26), we can obtain a general expression for the complex refractive index:

$$n_c^2 = 1 - \frac{\sigma}{\varepsilon_0\omega}\frac{i}{1+i\omega\tau}. \tag{2.28}$$

As mentioned earlier, characteristics of wave propagation change at different frequencies. At very low frequency, equation (2.28) can be approximated as

$$n_c^2 \approx -\frac{\sigma}{\varepsilon_0\omega}i. \tag{2.29}$$

Since $-i = \left(\frac{1-i}{\sqrt{2}}\right)^2$, we can manipulate the above equation to the form:

$$n_c = \sqrt{\frac{\sigma}{2\varepsilon_0\omega}}(1-i). \tag{2.30}$$

As well known, $n_c = n - i\kappa$, where n is the refractive index and κ is the extinction coefficient and both are positive numbers. The real and imaginary components of n_c at low frequencies are thus given as

$$n \approx \kappa \approx \sqrt{\frac{\sigma}{2\varepsilon_0\omega}}. \tag{2.31}$$

Thus, at low frequencies, the real and imaginary parts of the refractive index of a metal have approximately the same magnitude. With such a large imaginary part to the index, the wave is rapidly attenuated in the metal. If equation (2.30) is expressed in terms of K and substituted into equation (2.24) and simplified, we can see that the amplitude of a wave going in the z-direction decreases as:

$$e^{-\sqrt{\frac{\omega\sigma\mu_0}{2}}z}. \tag{2.32}$$

The above equation can be rewritten as $e^{-z/\delta}$, where δ is the distance in which the electric field or intensity of a normally-incident plane wave (i.e. the wave amplitude) decreases to e^{-1} (i.e. roughly one-third) of its initial value. The amplitude of such a wave as a function of z is shown in Figure 2.2.

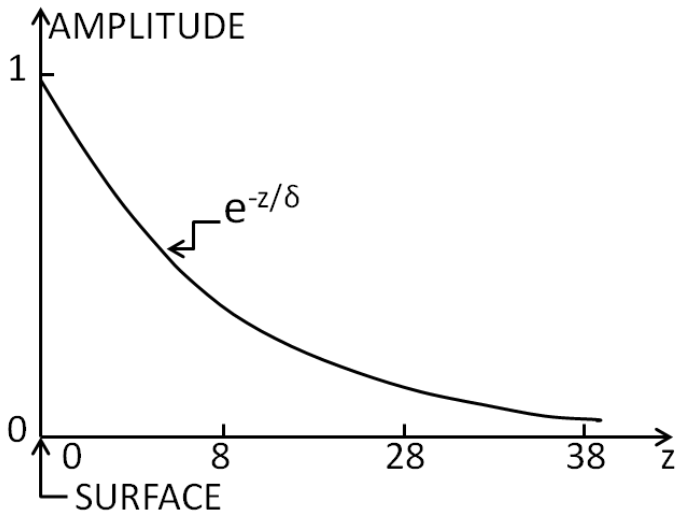

Figure 2.2 The amplitude of a transverse electromagnetic wave as a function of distance into a metal. [17]

As electromagnetic waves will penetrate into a metal only this distance, δ is called the skin depth and is given by:

$$\delta = \sqrt{\frac{2}{\omega\sigma\mu_0}}. \tag{2.33}$$

The skin depth is a measure of the characteristic distance that an electromagnetic wave travels in a conductor. For a metal to be partially transparent, the skin depth must be large in comparison to its thickness.

In a high frequency region, equation (2.28) can be simplified by getting rid of the complex number in the denominator:

$$n_c^2 = 1 - \frac{\sigma\tau}{\varepsilon_0}\frac{1}{1+\omega^2\tau^2} - \frac{\sigma}{\varepsilon_0\omega}\frac{1}{1+\omega^2\tau^2}i\,. \tag{2.34}$$

By substituting equation (2.21) into equation (2.34) and simplifying, we get

$$n_c^2 = 1 - \frac{\omega_p^2}{\omega^2+\tau^{-2}} - \frac{\omega_p^2}{\omega^2+\tau^{-2}}\left(\frac{1}{\omega\tau}\right)i\,. \tag{2.35}$$

where $\omega_p = \sqrt{\frac{Nq_e^2}{m\varepsilon_0}}$ is the plasma frequency of the metal. This equation is also known as the Drude model. The plasma frequency is the natural frequency of density oscillations of the free electrons inside the conductor, where the oscillation is due to the repulsion (by electric forces) and inertia of the ensemble of electrons. It is a kind of 'critical' frequency below which the index of a metal has an imaginary part and thus waves are attenuated, but above which the index is approximately real and the metal becomes transparent for sufficiently high frequencies.

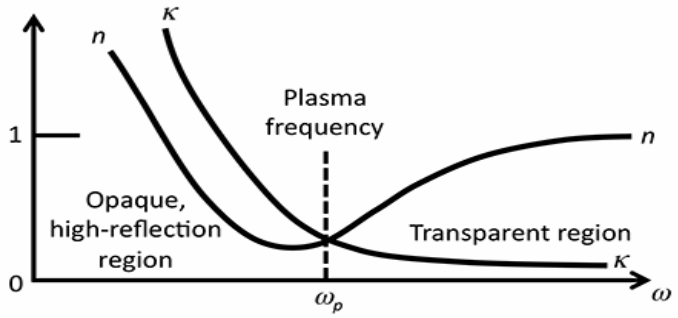

Figure 2.3 Plot of index of refraction *n* and extinction coefficient *κ* for a metal versus frequency. [18]

Referring to equation (2.35), we can find the expressions for n and κ:

$$n^2 - \kappa^2 = 1 - \frac{\omega_p^2}{\omega^2 + \tau^{-2}}, \tag{2.36}$$

$$2n\kappa = \frac{\omega_p^2}{\omega^2 + \tau^{-2}}\left(\frac{1}{\omega\tau}\right). \tag{2.37}$$

Figure 2.3 illustrates a good summary of the characteristics of n and κ, whose relation to frequency was given above in detail. This model describes many real metals remarkably well for approximations of ω_p on the order of 10^{16} rad/s and τ^{-1} on the order of 10^{13} s^{-1}.

Since the absorption of electromagnetic waves by metal is mainly due to the collisions of free electrons with the atomic lattice, a lossless metal approximation (i.e. an ideal case) assumes that there are no collisions inside the metal. This means that the relaxation time $\tau \to \infty$, and $\sigma \to \infty$ in the static case, which means the lossless metal has infinite conductivity at DC. However, at high frequencies the inertial effects of electrons cannot be neglected. Therefore, equation (2.35) can be further simplified for a lossless metal case as:

$$n_c^2 = \varepsilon_r = 1 - \frac{\omega_p^2}{\omega^2}. \tag{2.38}$$

This equation is called the lossless Drude model. For frequencies less than the plasma frequency, ε_r is negative, and the refractive index ($n_c = i\kappa$) and corresponding wavenumber ($K = n_c k_0$) are both purely imaginary, leading to a pure evanescent decay of the field and a complete reflection of the energy of the incident wave at the metal boundary. For frequencies above the plasma frequency, ε_r is positive but less than one, the refractive index and corresponding wavenumber become purely real, leading to a lossless propagation of EM waves inside the metal. However, the medium is highly

dispersive for frequencies just above the plasma frequency and n varies rapidly with frequency.

In conclusion, knowing the skin depth and plasma frequency of a particular metal enables us to understand how a metal behaves within multilayers, and thus evaluate the design of these multilayers. For example, it is sometimes assumed that any structures containing metal of total thickness more than a few skin depths will reflect light of all frequencies and operate as a thick metal shield. In this thesis, however, with the assistance of the aforementioned PT theory and admittance matching concepts, we verify that metal-dielectric (MD) multilayers containing many skin depths of metal can exhibit bands of high transparency when resonant tunneling conditions are satisfied.

2.3.2 Propagating and evanescent waves

Throughout this thesis, the terms propagating waves and evanescent waves are used extensively. The meaning behind these terms is most simply illustrated by considering an interface between two lossless media, as shown in Figure 2.4, where the incident medium is assumed to have the higher refractive index. Consider a plane wave incident on the interface; the plane wave is a propagating wave and has the form described by equation (2.24). The transmitted wave vector can be decomposed into the x-and z-direction ($Kt^2 = Kt_z^2 + Kt_x^2$), as shown in the figure. Therefore, the wave equation in medium n_2 becomes

$$\mathbf{E} = \mathbf{E_0} e^{i(\omega t - Kt_z z - Kt_x x)}, \tag{2.39}$$

For the incident angle smaller than the critical angle, there will be a propagating wave in medium n_2, where Kt_x and Kt_z are both real. When the incident angle is greater than the critical angle, Kt_z will still be real, but will be greater than $Kt = n_2 K_0$, and thus the Kt_x component becomes imaginary. This situation will result in an evanescent wave inside the medium n_2. The evanescent wave decays quickly away from the boundary, and does

not carry energy into the second medium (i.e. that is what is meant by 'total internal reflection'). For a conventional lens, wave components (i.e. from an object) that have an imaginary Kt_x are not collected. In other words, part of the information necessary to reconstruct the object at the image plane is lost due the fast exponential decay of the evanescent waves in the near field of the object.

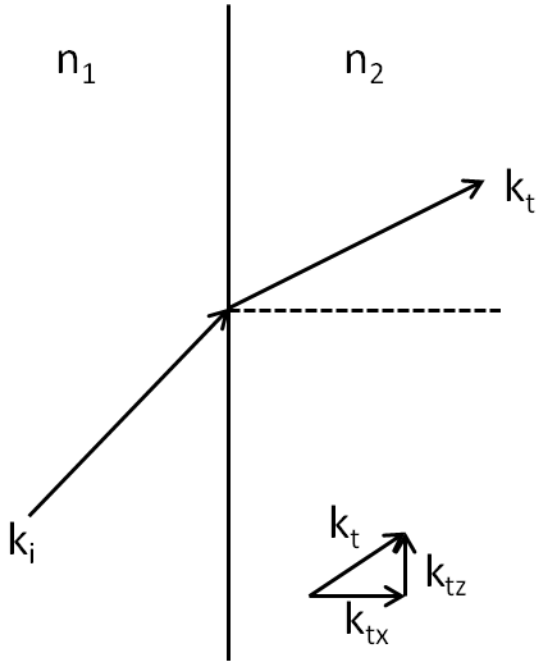

Figure 2.4 Schematic illustration of the wave propagation at the interface of two materials with $n_1 > n_2$.

2.3.3 Ag model employed for simulations

Silver is commonly used in metal-dielectric photonic crystals because the interband absorption peaks lie energetically above the visible spectrum, opening up the possibility of a broad range of applications in the visible portion of the spectrum [1, 19, 20, 21, 22].

The Lorentz-Drude (LD) oscillator model, based on a damped harmonic oscillator approximation, is widely used to describe optical properties of an arbitrary solid [23, 24, 25, 26]. The LD model separates explicitly the intraband effects (i.e. free-electron effects) from interband effects (i.e. bound-electron effects) [27, 28]. The intraband effects are

described by the Drude model [29, 30], while the interband effects are described by the simple semiquantum model resembling the Lorentz result for insulators. The LD model is a simple addition of the intraband effects and interband effects. Rakic *et al.* [31] reported a useful LD model for Ag, based on fitting to published experimental data. The closed-form expressions from reference [31] were encoded in MatLab, and produce the optical constants plotted in Figure 2.5. This model was used extensively for the transfer matrix simulations detailed in later chapters.

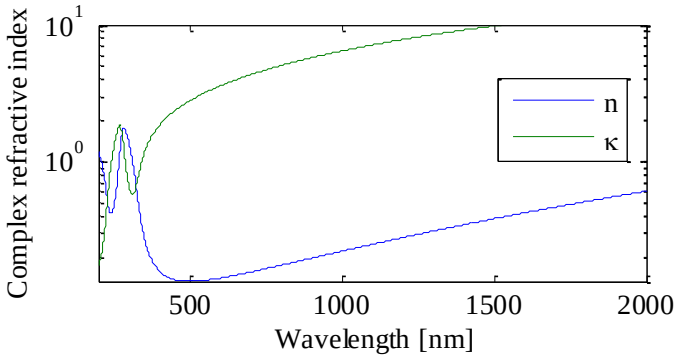

Figure 2.5 A plot for Ag optical constants in the visible to near IR region using the Lorentz-Drude model from reference [31].

2.4 Sample fabrication

2.4.1 Fabrication

Samples were prepared using physical vapor deposition in a six pocket electron-beam evaporator (see Figure 2.6) with a base pressure of ~ 10^{-7} Torr. The material to be deposited is bombarded with a beam of electrons, which conducts heat and melts the material to a boiling liquid that then produces vapor. The atoms or molecules of material gain velocity due to high temperature, travel through vacuum space, and then condense and solidify on the cold (i.e. normally about room temperature) substrate surface. The high vacuum assures that the atoms or molecules have a long mean free path, such that they do not collide with each other before reaching the substrate. The materials are

contained in a resistive heat crucible, which is commonly called the liner. Liners usually are constructed from materials with high melting temperature, such as W (3380^{o}C), Ta (2980^{o}C), Mo (2630^{o}C) and graphite (3730^{o}C). The electron bombardment induces very high temperature (i.e. exceeding 5000^{o}C), the hearth is water cooled to avoid contamination problems. Since the electron-beam evaporator has six pockets (i.e. six hearths to contain liners), layers are sequentially deposited without breaking the vacuum. More details for the deposition can be found in Appendix A.

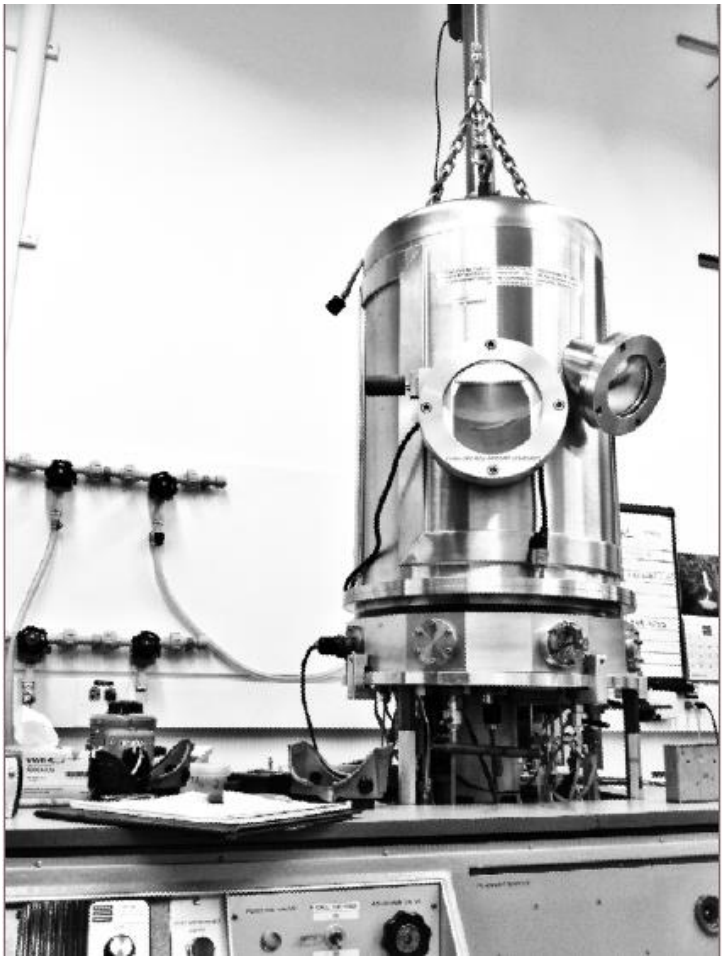

Figure 2.6 A camera picture of the six-pocket electron beam evaporator.

2.4.2 Materials

In this thesis work, three materials – Ag, SiO_2 and TiO_2 - were used for the theoretical and experimental study. SiO_2 and TiO_2 are chosen to form a high- and low-index periodic structure, which is essentially a Bragg reflector. The Ag is chosen due to its excellent optical properties and potential for low loss in the visible spectrum, and its optical constants were modeled as described above.

Silicon dioxide is a low refractive index material that is commonly used in combination with high refractive index oxide layer coatings to operate in different ranges of the optical spectrum. Due to its long-term stability, amorphous nature, high density, and low particulate contamination, SiO_2 has many applications such as high-reflection coatings, antireflection coatings, dielectric mirrors, beam-splitters, optical filters, and polarizers. In this thesis, the refractive index of SiO_2 was mainly approximated using a standard Sellmeier model, and a plot is shown in Figure 2.7.

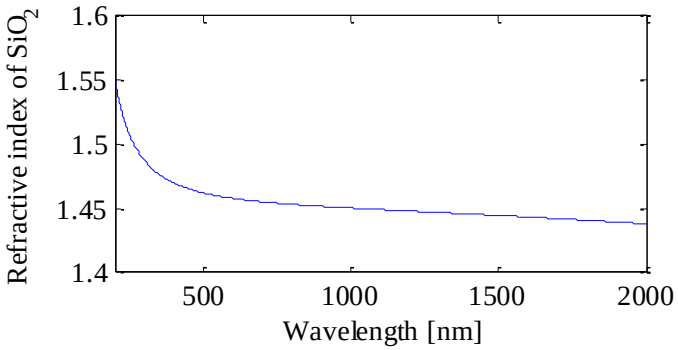

Figure 2.7 A plot for the refractive index of SiO_2 calculated from a standard Sellmeier model.

Titanium dioxide is widely used due to its high refractive index and low optical loss in the UV-VIS-NIR spectral range. The use of this high refractive index oxide in MD multilayers can reduce the electric field density within the absorptive metal layers and thereby enhance the transparency of the metal. This is discussed in greater detail in chapters 3 – 5. However, an oxygen environment (i.e. ~10^{-5} Torr) is normally required

during deposition because TiO_2 dissociates during evaporation. This can lead to the potential of oxygen diffusion and the eventual corrosion of the metal layers in the multilayers [32]. In this thesis, the optical constants of e-beam evaporated TiO_2 was modeled using a Forohi-Bloomi model from Kim *et al.* [33], and a plot for the refractive index model is shown in Figure 2.8.

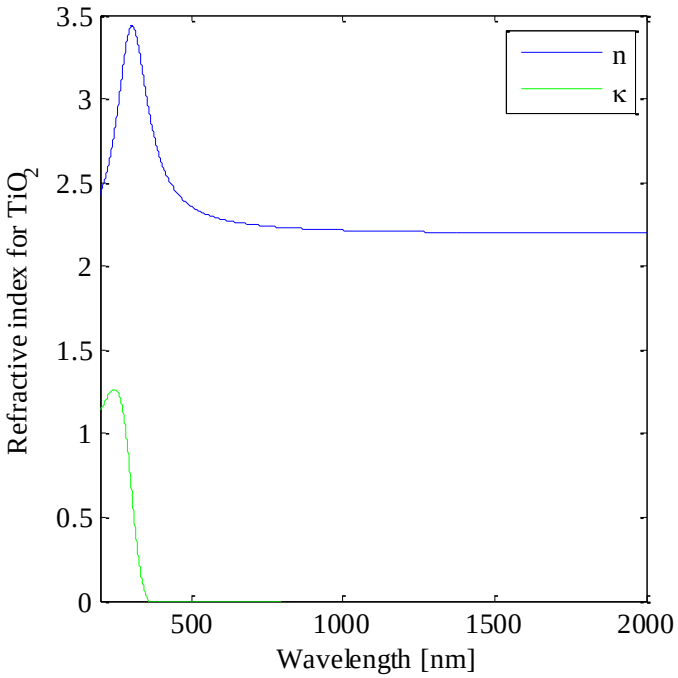

Figure 2.8 A plot for the optical constants of TiO_2 in the visible to near IR region using Forohi-Bloomer model.

References

[1] M. J. Bolemer and M. Scalora, "Transmissive properties of Ag/MgF2 photonic band gaps," *Appl. Phys. Lett.*, vol. 72, pp. 1676-1678, (1998).

[2] R. S. Bennink, Y. K. Yoon, R. W. Boyd and J. E. Sipe, "Accessing the optical

nonlinearity of metals with metal- dielectric photonic bandgap structures," *Opt. Lett.*, vol. 24, pp. 1416-1418, (1999).

[3] R. Dragila, B. Luther-Davies and S. Vukovic, "High transparency of classically opaque metallic films," *Phys. Rev. Lett.*, vol. 55, p. 1117–1120, (1985).

[4] S. Hayashi, H. Kurokawa and H. Oga, "Observation of resonant photon tunneling in photonic double barrier structures," *Optical Review*, vol. 6, pp. 204-210, (1999).

[5] M. J. Bloemer, G. D'Aguanno, N. Mattiucci, M. Scalora and N. Akozbek, "Broadband super-resolving lens with high transparency in the visible range," *Appl. Phys. Lett.*, vol. 90, p. 174113, (2007).

[6] S. A. Ramakrishna, J. B. Pendry, M. C. Wiltshire and W. J. Stewart, "Imaging the near field," *J. Mod. Opt.*, vol. 50, pp. 1419-1430, (2003).

[7] P. H. Berning and A. F. Turner, "Induced transmission in absorbing films applied to band pass filter design," *J. Opt. Soc. Am.*, vol. 47, pp. 230-239, (1957).

[8] P. W. Baumeister, "Radiant power flow and absorptance in thin films," *Appl. Opt.*, vol. 8, pp. 423-436, (1969).

[9] H. A. Macleod, "A New Approach to the Design of Metal-dielectric Thin-film Optical Coatings," *Optica Acta: International Journal of Optics,* vol. 25, pp. 93-106, (1978).

[10] H. A. Macleod, "Thin-Film Optical Filters," in *Chapter 8*, 3 ed., Institute of Physics Publishing, 2010.

[11] B. V. Landau and P. H. Lissberger, "Theory of Induced-Transmission Filters in Terms of the Concept of Equivalent Layers," *J. Opt. Soc. Am.*, vol. 62, pp. 1258-1264, (1972).

[12] P. H. Lissberger, "Coatings with induced transmission," *Appl. Opt.*, vol. 20, pp. 95-104, (1981).

[13] T. W. Allen and R. G. DeCorby, "Conditions for admittance-matched tunneling through symmetric metal-dielectric stacks," *Optics Express*, vol. 20, no. 55, pp. A578-A588, (2012).

[14] W. Chen, M. D. Thoreson, S. Ishii, A. V. Kildishev and V. M. Shalaev, "Ultra-thin ultra-smooth and low-loss silver films on a germanium wetting layer," *Opt. Express*, vol. 18, pp. 5124-5134, (2010).

[15] D. Owens, C. Fuentes-Hernandez and B. Kippelen, "Optical properties of one-dimensional metal-dielectric photonic band-gap structures with low-index dielectrics," *Thin Sol. Films*, vol. 517, pp. 2736-2741, (2009).

[16] T. W. Allen and R. G. DeCorby, "Assessing the maximum transmittance of periodic metal-dielectric multilayers," *JOSA B*, vol. 28, no. 10, pp. 2529-2536, (2011).

[17] R. P. Feynman, R. B. Leighton and M. Sands, The Feynman Lectures on Physics, Addison-Wesley Publishing Company, Inc., (1964).

[18] G. R. Fowles, Introduction to Modern Optics, Second Edition ed., Dover Publications, Inc., (1975).

[19] M. C. Larciprete, C. Sibilia, S. Paoloni, M. Bertolotti, F. Sarto and M. Scalora, "Accessing the optical limiting properties of metallo-dielectric photonic band gap structures," *J. Appl. Phys.*, vol. 93, pp. 5013-5018, (2003).

[20] M. S. Sarto, F. Sarto, M. C. Larciprete, M. Scalora, M. D'Amore, C. Sibilia and M. Bertolotti, "Nanotechnology of transparent metals for radio frequency electromagnetic shielding," *IEEE Trans. Electromagn. Compat.*, vol. 45, p. 586,

(2003).

[21] M. Scalora, M. J. Bloemer, A. S. Pethel, J. P. Dowling, C. M. Bowden and A. S. Manka, "Transparent, metallo-dielectric, one-dimensional, photonic band-gap structures," *J. Appl. Phys.,* vol. 83, p. 2377, (1998).

[22] M. Scalor, N. Mattiucci, G. D'Aguanno, M. Larciprete and M. J. Bloemer, "Nonlinear pulse propagation in one-dimensional metal-dielectric multilayer stacks: ultrawide bandwidth optical limiting," *Phys. Rev. E,* vol. 73, p. 016603, (2006).

[23] C. J. Powell, "Analysis of Optical- and Inelastic-Electron-Scattering Data. II. Application to Al," *J. Opt. Soc. Am.*, vol. 60, pp. 78-93, (1970).

[24] C. M. Herzinger, H. Yao, P. G. Snyder, F. G. Celii, Y. C. Kao, B. Johs and J. A. Woollam, "Determination of AlAs optical constants by variable angle spectroscopic ellipsometry and a multisample analysis," *J. Appl. Phys.*, vol. 77, p. 4677–4687, (1995).

[25] M. Schubert, V. Gottschalch, C. M. Herzinger, H. Yao, P. G. Snyder and J. A. Woollam, "Optical-constants of GaxIn1-xP lattice-matched to GaAs," *J. Appl. Phys.*, vol. 77, p. 3416–3419, (1995).

[26] C. M. Herzinger, P. G. Snyder, F. G. Celii, Y. C. Kao, D. Chow, B. Johs and J. A. Woollam, "Studies of thin strained InAs, AlAs, and AlSb layers by spectroscopic ellipsometry," *J. Appl. Phys.*, vol. 79, p. 2663–2674, (1996).

[27] H. Ehrenreich and H. R. Philipp, "Optical properties of Ag and Cu," *Phys. Rev.*, vol. 128, p. 1622–1629, (1962).

[28] H. Ehrenreich, H. R. Philipp and B. Segall, "Optical properties of aluminum," *Phys. Rev.*, vol. 132, p. 1918–1928, (1963).

[29] M. I. Markovic and A. D. Rakic, "Determination of optical properties of aluminum including electron reradiation in the Lorentz–Drude model," *Opt. Laser Technol.*, vol. 22, p. 394–398, (1990).

[30] M. I. Markovic and A. D. Rakic, "Determination of the reflection coefficients of laser light of wavelengths lambda(0.22 microm,200 microm) from the surface of aluminum using the Lorentz-Drude model.," *Appl. Opt.*, vol. 29, p. 3479–3483, (1990).

[31] A. D. Rakic, A. B. Djurisic, J. M. Elazar and M. L. Majewski, "Optical Properties of Metallic Films for Vertical-Cavity Optoelectronic Devices," *Applied Optics*, vol. 37, no. 22, pp. 5271-5283, (1998).

[32] M. S. Sarto, R. L. Voti, F. Sarto and M. C. Larciprete, "Nanolayered lightweight flexible shields with multidirectional optical transparency," *IEEE Trans. Electromagn. Compat.*, vol. 47, pp. 602-611, (2005).

[33] S. Y. Kim, "Simultaneous determination of refractive index, extinction coefficient, and void distribution of titanium dioxide thin film by optical methods," *Appl. Opt.*, vol. 35, pp. 6703-6707, (1996).

Chapter 3 Experimental study of optimized surface-plasmon-mediated tunneling in metal-dielectric multilayers[1]

3.1 Introduction

Dielectric-metal-dielectric (DMD) coatings have been studied for many applications, including energy-efficient windows [1, 2] and transparent electrodes for displays [3]. Since the late 1990s, it has been widely recognized [4] that periodic DMD multilayers can exhibit bands of high transparency. This property is based on resonant photon tunneling through metal layers, which is analogous to quantum mechanical tunneling of electrons through potential barriers [5]. Tunneling through a one period dielectric-metal-dielectric (DMD) structure, facilitated by resonant excitation of surface plasmons, was originally reported by Dragila *et al.* [6] and later by Hayashi *et al.* [7] Plasmon-mediated tunneling through multi-period DMD stacks is a subject of significant current interest, motivated by applications to super-lensing [8, 9] and metamaterials [10]. Power flow in these structures remains a subject of ongoing research. For example, the multilayers described in the recent experimental studies by Tomita *et al.* [11, 12] were far from optimized in terms of their transmittance (T), and exhibited significant discrepancy between the theoretically predicted and experimentally measured transmittance [12]. A related theoretical study by Feng *et al.* [13] demonstrated the existence of a photonic tunneling band in symmetric DMD structures. However, that work was restricted to a lossless-metal-assumption, and thus did not provide insight on the actual transmittance that can be expected for multilayers containing realistic lossy metals.

Potential transmittance (PT) theory, which was first described by Berning and Turner [14], is a powerful tool for understanding and optimizing the tunneling efficiency of

[1] This chapter was published as a paper in *Applied Physics Letter*, vol. 103, pp. 071109, 2013

metal-dielectric stacks. For example, it readily explains the observation that transmittance can be increased by dividing a given thickness of metal into a number of thinner and properly spaced metal layers [4, 8]. In previous work [15, 16], we extended PT theory to include cases of photon tunneling mediated by surface plasmons. Furthermore, we developed an admittance matching theory to optimize the surface-plasmon-mediated tunneling (i.e. to maximize transmittance) in DMD multilayers containing real absorbing metal layers [15]. Here, we describe the fabrication and experimental characterization of theoretically optimized DMD multilayers with 1, 2, and 3 periods. The experimental results are in good agreement with theoretical predictions, verifying that PT theory is an indispensable tool for optimizing power flow through absorbing multilayers.

3.2 Sample design

The transparency of a thin absorbing film is influenced by its boundary conditions, and the maximum potential transmittance (PT_{MAX}) of a sufficiently thin absorbing film is much greater than the transmittance predicted by the bulk optical absorption coefficient for the same material [16]. To achieve $T=PT_{MAX}$ at a given wavelength, one must match the admittance of the absorbing film to the incident and exit media. Specifically, the optical admittance viewed from the absorbing film must attain a particular value $Y_{op}=X_{op}+iZ_{op}$, determined only by the optical constants and thickness of the absorbing film [15, 16]. Note that the admittance of a non-magnetic medium is given by nY_0, where n is refractive index and Y_0 is the admittance of free space. Thus, admittance matching is equivalent to matching the effective index of the multilayer to the index of the external medium.

Consider a one period DMD unit cell embedded between identical incident and exit media as shown in Figure 3.1 (a). Conditions (i.e. particular combinations of λ, n_1, d_1, N_m,

d_m, n_2, and θ_2) that maximize transmittance (i.e. that result in $T=PT_{MAX}$) for a DMD unit cell are identical to conditions that maximize transmittance through the periodic multilayer (Figure 3.1 (b)) based on the same unit cell [15, 16].

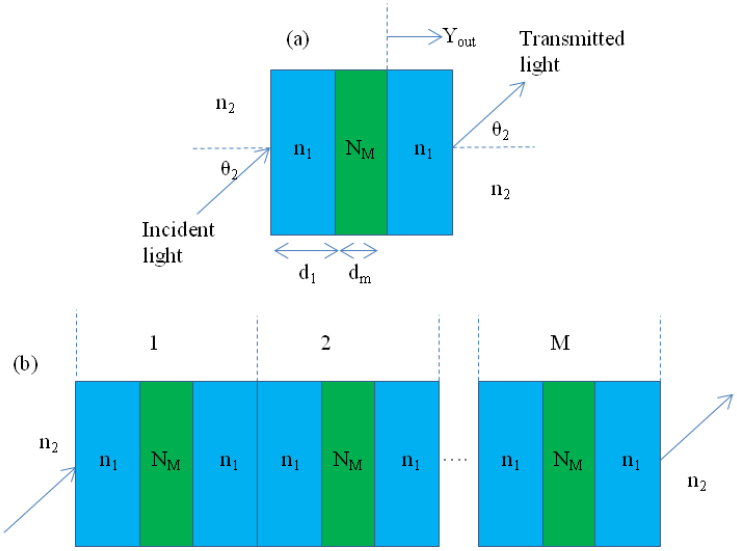

Figure 3.1 (a) Schematic illustration of a one period DMD unit cell. Note that the admittance viewed from the absorbing metal film and looking towards the exit medium (Y_{out}) is that of a thin dielectric film n_1 on a uniform exit medium n_2. (b) A schematic illustration of a multi-period DMD structure embedded between identical incident and exit media.

Plasmon-mediated tunneling can be studied by embedding the DMD structure between two high index prisms (ex. SF11 glass prisms) such that $n_2 > n_1$, enabling the incident propagating wave inside the prism to excite evanescent waves within the multilayer. For the work described below, we used SF11 glass prisms (n_2 ~ 1.778 at 632.8 nm wavelength) and SiO_2 thin films (modeled using a standard Sellmeier expression for fused silica, which predicts n_1 ~ 1.457 at 632.8 nm wavelength) as the dielectric spacer material in the DMD stacks. Furthermore, the metal layers are Ag, which we modeled using the Lorentz-Drude expressions from Rakic *et al.* [17], except where indicated otherwise below. That model predicts a complex refractive index N_m ~ 0.1436 - 3.8045i at 632.8 nm wavelength.

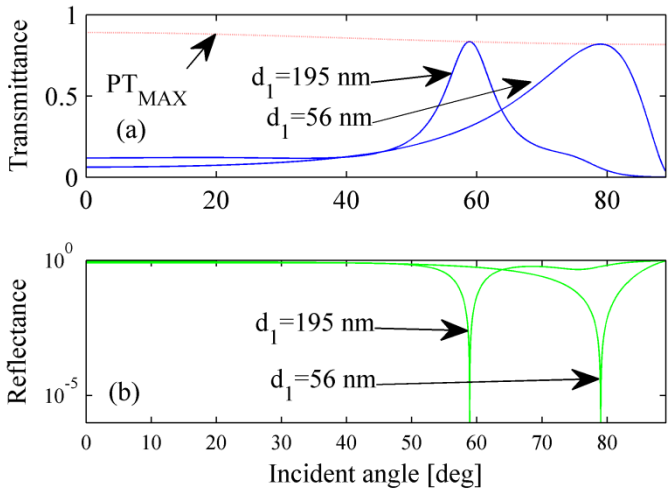

Figure 3.2 Predicted transmittance versus incident angle at 632.8 nm wavelength for a one period DMD stack with d_m = 40 nm, N_m = 0.1436 - 3.8045i, n_1 = 1.457 and n_2 = 1.778. The curves correspond to particular values of the dielectric layers thickness d_1 (as labeled), which were determined by solutions to (1). The red dashed curve indicates PT_{MAX} versus incident angle for the 40 nm Ag layer. The plots verify the existence of admittance-matched tunneling (i.e. $T = PT_{MAX}$) at the particular incident angles predicted by solutions to the admittance matching equation. (b) Predicted reflectance versus incident angle for the same conditions as in part (a). Note that the reflectance diverges at the two angles that produce a perfect admittance match.

As discussed elsewhere [15], the existence and number of discrete solutions to (2.2.4) is dependent on the particular dielectric indices, metal layer, and wavelength. This unpredictability is likely related to the large number of variables involved, but further physical insight is left for future work. For the Ag layer thickness (d_m = 40 nm), dielectric refractive indices (n_1 = 1.457, n_2 = 1.778), and wavelength (λ_0 = 632.8 nm) chosen here, two solutions were found for TM-polarized light. Specifically, admittance matched tunneling is predicted for θ_2 ~ 59 degrees (when d_1 ~ 195 nm) or ~ 79 degrees (when d_1 ~ 56 nm). Figure 3.2 (a) and (b) show the transmittance and reflectance plotted versus incident angle of TM polarized light, for each of these specific DMD structures. Consistent with a perfect admittance match, $T \sim PT_{MAX}$ and $R \sim 0$ are obtained for the incident angles mentioned above.

Note that the critical angle for total internal reflection (TIR) between SF11 glass and SiO_2, using the aforementioned indices, is approximately 55 degrees. Thus, both transmittance peaks shown in Figure 3.2 correspond to surface-plasmon-mediated tunneling conditions. To further illustrate this fact, Figure 3.3 shows the spatial distribution of the field intensity for 1-, 2- and 3-period multilayers, and for one of the admittance-matched conditions mentioned above. The field profiles reveal evanescent behaviour in both the Ag and SiO_2 layers, with resonant field enhancement at each metal-dielectric interface, which are hallmarks of surface-plasmon-mediated tunneling [6].

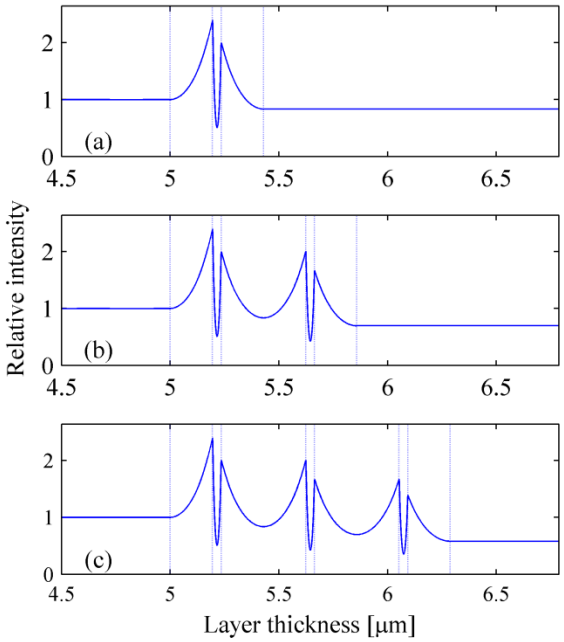

Figure 3.3 Theoretically predicted spatial intensity distribution for one (a), two (b), and three (c) period DMD multilayers, with n_2 = 1.778, n_1 = 1.457, N_m = 0.1436 - 3.8045i, d_1 = 194.5 nm, d_m = 40 nm, for 58.88 degrees incident angle at 632.8 nm wavelength.

Figure 3.4 shows the simulated transmittance versus incident angle and wavelength, for DMD multilayers having the same layer dimensions as assumed for Figure 3.3. For wavelengths greater than ~ 500 nm, the dominant tunneling features occur beyond the critical angle for TIR (i.e. ~ 55 degrees). Fabry Perot tunneling features are evident for

the 2- and 3-period structure, for wavelengths below ~ 650 nm. With an increasing number of periods, splitting of both the surface-plasmon and Fabry-Perot mediated tunneling bands is evident. In the evanescent range, this mode-splitting arises from coupling between the plasmonic super-modes of the isolated metal films, and is a well-known property of coupled resonator system [13]. Note that at the admittance-matched tunneling angle (~ 60 degrees), there exists a featureless "transparent band" [13] extending from ~ 580 – 680 nm in wavelength. For real metals, the peak transmittance of this band reduces with increasing number of periods, but its existence and essential features (absence of spectral ripples, etc.) are nonetheless consistent with the predictions in reference [13].

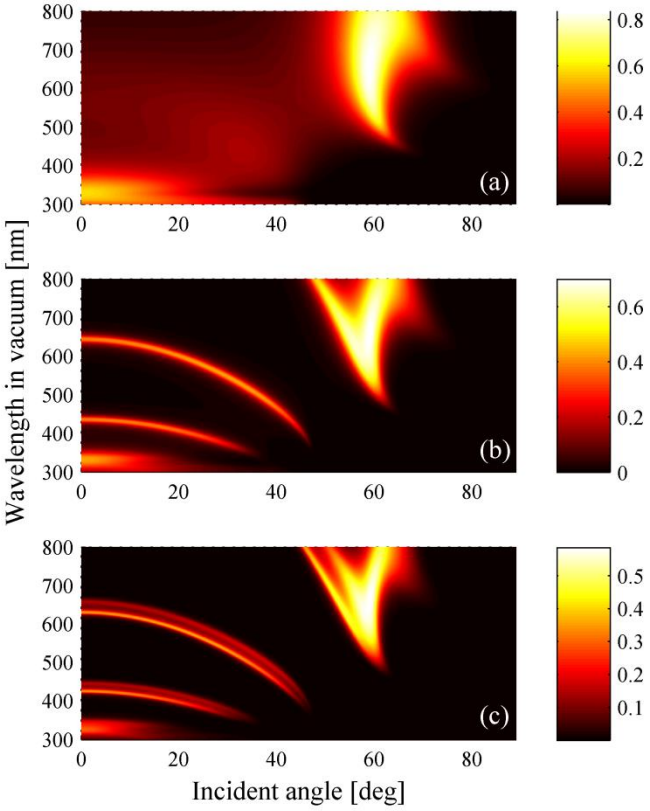

Figure 3.4 Simulated colormap plot of transmittance of TM-polarized light versus incident angle and wavelength, for one (a), two (b), and three (c) period DMD stacks. The layer thicknesses are the same as assumed in Figure 3.3.

3.3 Experimental study

For experimental studies, we focused on the first of the two admittance-matched cases described above (i.e. d_1 ~ 195 nm, d_m ~ 40 nm, producing a tunneling peak near ~ 59 degrees inside an SF11 glass incident medium). 1-, 2-, and 3-period SiO_2-Ag-SiO_2 samples were deposited on clean SF11 substrates using a six-pocket electron-beam evaporator. For each sample, the layers were sequentially deposited in the evaporator without breaking vacuum. During deposition, the thickness of each layer was obtained using the average value of readings from two thickness monitors. After deposition, the as-deposited thickness was first estimated using a scanning profilometer (Alpha Step IQ).

Subsequently, experimental reflectance versus wavelength was obtained for near-normal incidence from air (using a spectrophometer and an ellipsometer), and layer thicknesses were verified by fitting the experimental reflectance to that predicted by a standard transfer matrix method [18]. From these results (not shown), we estimated that the as-deposited thickness of the Ag layers was ~ 37-40 nm, while the as-deposited thickness of the SiO_2 layers was ~ 180-185nm. This level of error does not significantly impact the key features of the surface-plasmon-mediated tunneling peak of interest; simulations predict a slight shift (<1 degree) in the angular position of the tunneling peak and a slight increase (<5%) in the peak transmittance.

A custom-built, double-prism system was used to measure the transmittance of TM-polarized light as a function of incident angle (i.e. θ_2). A polarized, 632.8 nm wavelength He-Ne laser was used as a source. The sample holder consisted of two high index SF11 equilateral prisms (i.e. 60^o prisms) aligned face-to-face with the sample sitting in between as shown schematically in Figure 3.5 (a) and experimentally in Figure 3.5 (b). An index matching fluid (Diiodomethane) [12] was used between the sample and the prisms. The double-prism holder was placed on a customized plate, which was mounted on a rotation stage, to ensure the sample was centered accurately. Transmitted light was detected by an optical power meter connected to a sensing photodiode, which was mounted on a two axis stage to facilitate optimal alignment of the detected beam.

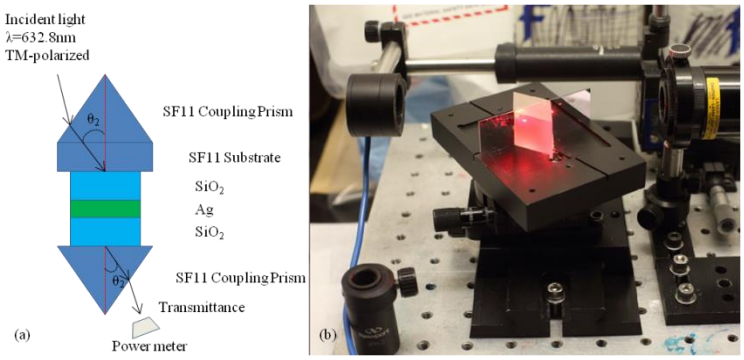

Figure 3.5 (a) A schematic illustration of the double-prism-coupler sample holder, with a 1 period DMD sample shown. (b) A picture of the experimental setup, including the double-prism-coupled sample illuminated by a 632.8nm incident beam from a He-Ne laser.

For calibration of the data, transmittance scans for the multilayer samples were normalized with respect to an angular transmittance scan of a plain SF11 substrate mounted in the same double-prism setup. The calibration plots (not shown) were relatively flat versus angle, with a typical transmittance of 0.83.

Figure 3.6 shows the measured and simulated transmittance of TM polarized light versus incident angle at a free-space wavelength of 632.8 nm. Due to limitations in the experimental setup, measured data is restricted to incident angles greater than ~ 45 degrees. For the simulations, the target thicknesses from above were used (i.e. 195 nm thick SiO_2 layers and 40 nm thick Ag layers). Furthermore, the plot includes simulated curves for two different values of the Ag index at this wavelength. The first is the value from the Rakic model [17] mentioned above (N_m ~ 0.1436 – 3.8045i) and the second is the value suggested by Dragila *et al.* [6] (N_m ~ 0.066 – 4i). As is well known, the optical constants of a thin metal film vary somewhat with thickness and deposition conditions, making it very difficult to extract a precisely accurate value for a particular sample. Moreover, the potential transmittance (and thus peak tunneling efficiency) of a metal film scales with the ratio of its extinction coefficient to its real part of refractive index. Because of this, the Dragila number results in a higher predicted peak transmittance as

shown in Figure 3.6. The red dotted curves in Figure 3.6 indicate the predicted PT_{MAX} for each case, using the Rakic index.

As shown in Figure 3.6 (a), the predicted tunneling peak is located at 58.9 degrees and the predicted maximum transmittance for the one period structure is ~0.83. The experimental results are in good agreement with these predictions, with a tunneling peak at ~58 degrees but a higher peak transmittance ~0.88. As mentioned above, an admittance-matched unit cell can be used to construct admittance-matched multilayers with an arbitrary number of periods. The results in Figure 3.6 provide good verification of this concept. For all three cases, the main tunneling peak occurs at ~58 degrees and the peak transmittance is near PT_{MAX}, which is indicative of a nearly optimal admittance match for all 3 cases. The experimental peak transmittance lies between the predictions based on the Dragila and Rakic indices. While a more accurate model for the film constants is left for future work, the results nevertheless suggest that the optical constants of our Ag films are within the range expected from the literature.

The experimental data also exhibit a secondary peak (i.e. a plateau) at ~ 68 degrees. The existence of two peaks within the evanescent regime is due to the presence of symmetric and anti-symmetric 'supermodes' associated with the coupled plasmons at each metal surface [6]. The symmetric mode lies at higher incident angle and is more heavily damped by metal absorption [6]. In fact, that peak is only weakly indicated by the theoretical predictions that employ the Rakic model. As above, the experimental data are intermediate with respect to these models.

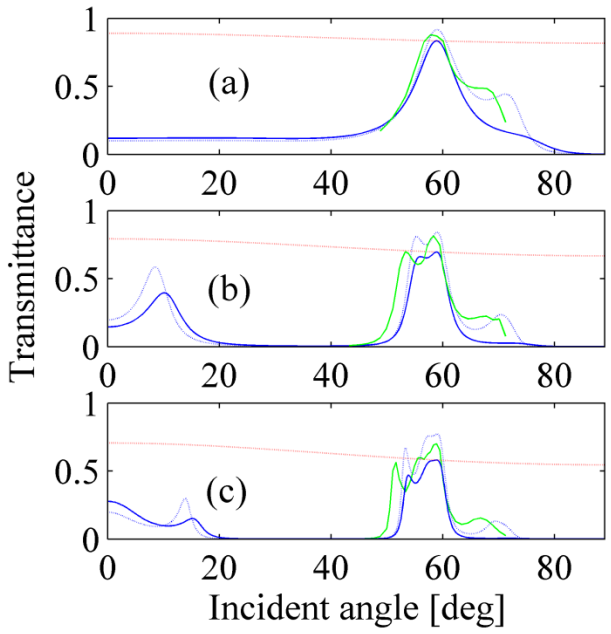

Figure 3.6 The experimental (green solid curves) and theoretical (blue curves) transmittance of TM-polarized light is plotted versus incident angle for one (a), two (b), and three (c) period samples, at a wavelength of 632.8 nm. The red dotted curve indicates PT_{MAX} for each case, using N_m = 0.1436 – 3.8045i. The blue solid curve is the predicted transmittance using this same value of metal index; note that $T = PT_{MAX}$ is predicted at the admittance-matched tunneling angle of ~ 59 degrees. The blue dotted curves are the predicted transmittance using N_m = 0.066-4i. Note that for the two and three period samples, Fabry-Perot transmittance peaks are predicted a low incidence angles (see Figure 3.4).

Discrepancies between theory and experiment can be attributed to several experimental uncertainties, as follows. First, it is very challenging to control and verify the thickness of such thin films as employed here, within accuracy better than ~5%. Second, precise determination of thin film optical constants is also challenging, particularly since these constants vary with thickness. The slightly wider bandwidth of the experimental tunneling features might indicate the Ag films are slightly thinner than targeted, but also could indicate disorder in the nominally periodic stacks. Finally, we estimate the angular accuracy of the experimental apparatus to be on the order of 1 degree. Nevertheless, the experimental data are in excellent overall agreement with

theoretical predictions, and provide verification of the expected trends related to the admittance-matched tunneling theory [15].

3.4 Summary and Conclusions

We deposited metallodielectric multilayers with a symmetric SiO_2-Ag-SiO_2 unit cell, in turn designed for admittance-matched tunneling in the evanescent wave regime. Experimental results were compared to the simulated results based on transfer matrix techniques, and the overall agreement is very good. These results provide experimental verification that potential transmittance theory and admittance-matching concepts can be used to optimize the transmittance of surface-plasmon-mediated tunneling through metal-dielectric multilayers. This approach might find application to related work on superlenses, thermal windows, transparent conductors, and optical filters.

References

[1] G. Leftheriotis, P. Yianoulis and D. Patrikios, "Design and optical properties of optimized ZnS/Ag/ZnS thin films for energy saving applications," *Thin Sol. Films*, vol. 306, pp. 92-99, (1997).

[2] C. C. Granqvist, "Transparent conductors for solar energy and energy efficiency: a broad-brush picture," *Int. J. Nanotechnol.*, vol. 6, pp. 785-797, (2009).

[3] X. Liu, X. Cai, J. Qiao, J. Mao and N. Jiang, "The design of ZnS/Ag/ZnS transparent conductive multilayer films," *Thin Sol. Films*, vol. 441, pp. 200-206, (2003).

[4] M. J. Bolemer and M. Scalora, "Transmissive properties of Ag/MgF2 photonic band gaps," *Appl. Phys. Lett.*, vol. 72, pp. 1676-1678, (1998).

[5] I. R. Hooper, T. W. Preist and J. R. Sambles, "Making Tunnel Barriers (Including Metals) Transparent," *Phys. Rev. Lett.*, vol. 97, p. 053902, (2006).

[6] R. Dragila, B. Luther-Davies and S. Vukovic, "High transparency of classically opaque metallic films," *Phys. Rev. Lett.*, vol. 55, p. 1117–1120, (1985).

[7] S. Hayashi, H. Kurokawa and H. Oga, "Observation of resonant photon tunneling in photonic double barrier structures," *Optical Review*, vol. 6, pp. 204-210, (1999).

[8] S. A. Ramakrishna, J. B. Pendry, M. C. Wiltshire and W. J. Stewart, "Imaging the near field," *J. Mod. Opt.*, vol. 50, pp. 1419-1430, (2003).

[9] Y. Xiong, Z. Liu, C. Sun and X. Zhang, "Two-dimensional imaging by far-field superlens at visible wavelengths," *Nano Lett.*, vol. 7, pp. 3360-3365, (2007).

[10] M. J. Bloemer, G. D'Aguanno, N. Mattiucci, M. Scalora and N. Akozbek, "Broadband super-resolving lens with high transparency in the visible range," *Appl. Phys. Lett.*, vol. 90, p. 174113, (2007).

[11] S. Tomita, T. Yokoyama, H. Yanagi, B. Wood, J. B. Pendry, M. Fujii and S. Hayashi, "Resonant photon tunneling via surface plasmon polaritons through one-dimensional metal-dielectric metamaterials," *Opt. Express*, vol. 16, pp. 9942-9950, (2008).

[12] M. Yoshida, S. Tomita, H. Yanagi and S. Hayashi, "Resonant photon transport through metal-insulator-metal multilayers consisting of Ag and SiO2," *Phys. Rev. B*, vol. 82, p. 045410, (2010).

[13] S. Feng, J. Merle Elson and P. L. Overfelt, "Optical properties of multilayer metal-dielectric nanofilms with all-evanescent modes," *Opt. Express*, vol. 13, pp. 4113-4124, (2005).

[14] P. H. Berning and A. F. Turner, "Induced transmission in absorbing films applied to band pass filter design," *J. Opt. Soc. Am.*, vol. 47, pp. 230-239, (1957).

[15] T. W. Allen and R. G. DeCorby, "Conditions for admittance-matched tunneling through symmetric metal-dielectric stacks," *Optics Express*, vol. 20, no. 55, pp. A578-A588, (2012).

[16] T. W. Allen and R. G. DeCorby, "Assessing the maximum transmittance of periodic metal-dielectric multilayers," *JOSA B*, vol. 28, no. 10, pp. 2529-2536, (2011).

[17] A. D. Rakic, A. B. Djurisic, J. M. Elazar and M. L. Majewski, "Optical Properties of Metallic Films for Vertical-Cavity Optoelectronic Devices," *Applied Optics*, vol. 37, no. 22, pp. 5271-5283, (1998).

[18] J. E. Gonzalez-Ramirez, J. Fuentes, L. C. Hernandez and L. Hernandez, "Evaluation of the Thickness in Nanolayers Using the Transfer Matrix Method for Modeling the Spectral Reflectivity," *Research Letters in Physics*, vol. 2009, p. 4 pages, 13 Feb. (2009).

Chapter 4 On the transparency and stability of Ag-based metal-dielectric multilayers[2]

4.1 Introduction and background

Metal-dielectric (MD) band-pass filters have been studied for many decades [1, 2], partly because of their potential for excellent out-of-band rejection over an extended spectral range [2, 3], and in spite of the fact that some absorptive loss within the pass-band is unavoidable. Historically, the induced-transmission (IT) filter of Berning and Turner [4, 5] has played a central role in this work. IT filters contain one or more [3] thin metal films, which are surrounded by a dielectric multilayer designed to admittance- (i.e. index-) match the entire assembly to the ambient media at a particular wavelength. Interest in MD band-pass filters was renewed by the work of Bloemer *et al*. [6] in the 1990s; they used a photonic band-gap formalism to design periodic MD filters exhibiting a broad transparency band in the visible range and opacity at most other wavelengths. These filters have potential as transparent conductors [7], heat-reflecting windows [8], nonlinear media [9], and as metamaterials and super-lenses [10].

Several features of periodic MD filters are now well understood. For example, the transparency band is due to the coupling of Fabry-Perot resonances associated with each pair of adjacent metal layers. The spectral position of these resonances is mainly controlled by the index and thickness of the dielectric spacer layers, while the width of the transparency band is related to the degree of coupling between the cavities. More specifically, thinner metal films lead to higher coupling, increased splitting of the isolated resonance features, and a wider band of transparency [11]. Moreover, dividing a given total thickness of metal into a higher number of thinner films allows for the possibility of

[2] This chapter was submitted for publication in the *Applied Optics*.

greater transparency [1]. It is also known [7] that high-index dielectric spacer layers enhance the transparency, bandwidth, and omnidirectionality of these stacks [12, 13]. In recent work [14, 15], we used potential transmittance (PT) theory to clarify the role of the dielectric index and verified that higher-index dielectric layers are able to provide an improved admittance match between the MD stack and the ambient media.

While high-index dielectrics provide advantages, they also present practical challenges in the context of MD filters. For example, dissociation of oxygen can occur during and after the deposition of TiO_2 and similar high-index films [12]. This can lead to oxidation of the metallic layers, particularly silver (Ag) [16], which otherwise has the most attractive properties for transparent MD stacks operating in the visible range. Low-index spacer layers are expected to provide simpler fabrication options and improved long-term stability but result in lower transparency. Owens *et al*. [17] showed that the transparency band can be enhanced by using an aperiodic, numerically optimized stack. Here, we consider periodic Ag/SiO_2-based multilayers, and show that appropriate termination of the stack can reduce the admittance mismatch with the external media, and thereby enhance the optical properties (such as peak transmittance and transparency bandwidth). In particular, we show that addition of a single high-index termination layer at each of the stack provides significant improvement in the optical properties.

4.2 Experimental and simulation details

MD multilayers were grown in a multi-pocket e-beam evaporation system. Target materials were Ag, SiO_2, and TiO_2, and films were deposited onto glass substrates that had been previously cleaned using a piranha solution. Chamber base pressure was ~10^{-7} Torr. TiO_2 films (only) were deposited in an oxygen environment at pressure ~$5x10^{-5}$ Torr, in order to ensure stoichiometry [18]. Normal-incidence transmittance curves were

obtained using a VASE instrument (J.A. Woollam Co. Inc.) and verified using a spectrophotometer (Perkin-Elmer Lambda 900). The transmittance in each case was normalized to that for a blank glass substrate. For design and transfer matrix simulations [19], we used Ag optical constants from the Lorentz-Drude model described by Rakic *et al.* [20], TiO_2 optical constants from the model of Kim *et al.* [18], and a fixed index n = 1.45 for SiO_2. The approximate validity of these models was verified by ellipsometric measurements (not shown) on Ag, TiO_2, and SiO_2 films.

As an illustration of the practical challenges associated with some Ag-based filters, consider the results shown in Figure 4.1 for a 3-period Ag/TiO_2 multilayer. The structure was designed with a DMD unit cell, so that the outermost TiO_2 layers act as 'anti-reflection' (AR) coatings [7, 10, 13] to reduce the admittance mismatch between the stack and the external media. Also plotted is the maximum potential transmittance (PT_{max}) [3, 14] for a stack containing three, 32 nm-thick Ag films. The peak theoretical transmittance (T_{max} ~ 0.65) is still well below PT_{max} (~0.8), because the refractive index of TiO_2 (~2.35) is not sufficiently high to enable a perfect admittance match. As we have described previously [15], to achieve $T_{max} \sim PT_{max}$ for a stack with a DMD unit cell would typically require that the dielectric refractive index is very high (> 4).

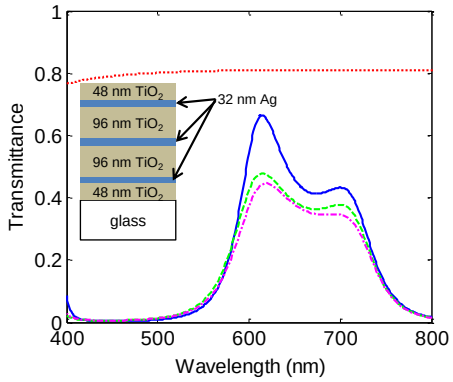

Figure 4.1 Theoretical versus experimental transmittance for a 3-period TiO_2/Ag-based MD stack is shown. Nominal layer thicknesses are indicated in the inset figure. The blue

solid curve is the theoretically predicted transmittance, and the red dotted curve is the theoretically predicted PT_{max} for a multilayer containing three, 32-nm-thick Ag films. Experimental transmittance is shown as measured 1 day (green dashed curve) and 6 months (magenta dashed-dotted curve) after deposition.

In terms of the shape and bandwidth of the transmission pass-band, the experimental results in Figure 4.1 are in good agreement with predictions, indicating that a good control over the layer thicknesses was achieved. However, the transmittance in the pass-band is well below the theoretical curve. This discrepancy is partly attributable to the oxidation of the Ag layers during the deposition of TiO_2, and the formation of an Ag-oxide layer at each interface [16, 17]. We observed similar, sub-optimal transparency for several other Ag/TiO_2-based multilayer samples. Moreover, we have observed that these multilayers degrade with time, as evidenced by the experimental curves in Figure 4.1 and discussed further below. These issues might be addressed by introduction of interlayers (such as Ti [12]) at each Ag-TiO_2 interface. However, that approach adds fabrication complexity and introduces some absorptive loss.

4.3 Admittance matching of Ag/SiO_2 –based multilayers

Ag/SiO_2-based multilayers can be deposited easily by various methods, and as discussed below exhibit relatively good stability. However, the low refractive index of SiO_2 implies a significant gap between T_{max} and PT_{max}. Our goal was to explore alternative strategies for improving the optical transparency band, while retaining the practical advantages mentioned above. As a case study, we designed and fabricated 5-period multilayers with the basic structure shown in Figure 4.2. A nominal target thickness of 25 nm was chosen for the Ag layers, while the SiO_2 spacer layers were chosen to be ~150 nm thick to produce a normal-incidence transmission peak near 530 nm wavelength.

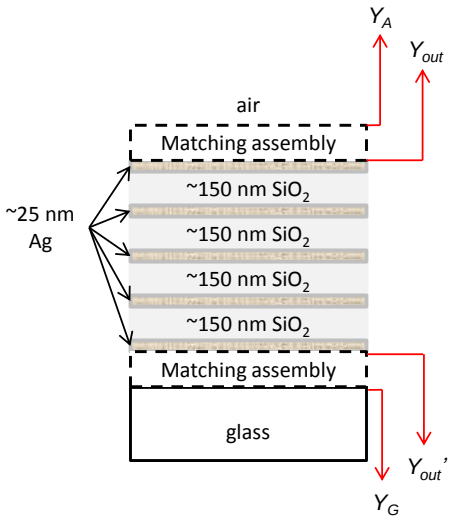

Figure 4.2 The schematic diagram represents the (5-period) Ag/SiO_2-based MD multilayers that were employed for the comparative study. Y_A is the admittance of the air ambient medium, Y_G is that for the glass ambient medium, and Y_{out} and Y_{out}' are the external admittances viewed from the perspective of the upper or lower Ag film in the multilayer, respectively. For experimental samples AR1 and AR2, each 'matching assembly' is a single 'anti-reflection' (AR) layer, either ~75 nm SiO_2 (sample AR1) or ~40 nm TiO_2 (sample AR2).

Consider the upper-most Ag film in the structure shown in Figure 4.2, and note that Ag has a refractive index of 0.133-3.01i at 530 nm wavelength (using the Ag model mentioned above). To eliminate reflectance from this film (while simultaneously maximizing transmittance), the optical admittance of the incident medium (from the perspective of the film) needs to attain a particular, optimal value $Y_{op} = X_{op}+iZ_{op}$. Expressions to calculate X_{op} and Z_{op} can be found elsewhere [3, 15], and for the 25 nm thick Ag film at a wavelength of 530 nm, and assuming normal incidence, the result is Y_{op} ~ 2.63+5.59i, where the admittance is expressed in free-space units (i.e. normalized to the admittance of free space). Note that at normal incidence, the normalized admittance is equal to the effective refractive index 'seen' by the layer at a particular wavelength. Thus, in the absence of a matching assembly we have $Y_{out} = 1$, which differs significantly from the optimal value and results in a significant front-surface reflectance. To maximize the

PT of the periodic multilayer, it is necessary that the exit admittance is matched to the same optimal value; i.e. $Y_{out}' = Y_{op}$. Moreover, maximal transmittance ($T = PT_{max}$) is possible when $Y_{out} = Y_{out}' = Y_{op}$ [3, 15], provided the inter-metal spacing is also optimized as described below.

As mentioned in Section 2, partial compensation of the admittance mismatch is possible by adding an AR layer of the same material as the inter-metal dielectric but with half the thickness [7, 13]. One of the samples (AR1) was terminated accordingly, with a 75 nm SiO_2 layer at each end of the multilayer. As shown below, this provides only modest improvement in the transparency of the sample. This prompted us to investigate the use of higher-index termination layers, while still employing SiO_2 as the inter-metal dielectric. Sample AR2 was fabricated with ~40 nm thick TiO_2 layers at each end of the multilayer. In order to evaluate Y_{out} for these samples, it is useful to recall that the normal-incidence admittance (in free space units) presented by a single homogeneous film with index n_f on a massive substrate with index n_{sub} can be expressed [3]:

$$Y_{fs} = \frac{n_{sub}\cos\delta_f + in_f \sin\delta_f}{\cos\delta_f + i\left(n_{sub}/n_f\right)\sin\delta_f} \quad , \tag{4.1}$$

where $\delta_f = (2\pi/\lambda)\cdot n_f d_f$ is the phase thickness of the film at wavelength λ, and d_f is the film thickness. For the two samples AR1 and AR2 described above, it follows that $Y_{out} = Y_{fs}$ where Y_{fs} is calculated using the appropriate values for n_{sub}, n_f, and d_f in each case. For AR1, with $n_f = 1.45$, $d_f = 75$ nm and $\lambda = 530$ nm, equation (4.1) predicts $Y_{out} = 1.94+0.39i$ and $Y_{out}' = 1.41-0.026i$ for $n_{sub} = 1$ (air) and $n_{sub} = 1.5$ (glass), respectively. For AR2, with $n_f = 2.35$, $d_f = 40$ nm and $\lambda = 530$ nm, equation (4.1) predicts $Y_{out} = 2.94+2.24i$ and $Y_{out}' = 2.87+1.05i$ for $n_{sub} = 1$ and $n_{sub} = 1.5$, respectively. Thus, for these samples a significant gap exists between Y_{out} (or Y_{out}') and Y_{op}, although the gap is smaller for AR2. In general,

the lower transmittance of MD stacks with low-index dielectric spacers is primarily caused by a greater admittance mismatch with the external media.

While the degree of admittance matching for a single AR layer is limited by the indices of available materials, it is possible to achieve a nearly perfect admittance match using a pair of materials and the well-known design principles developed for induced transmission (IT) filters [3]. IT filters are most commonly implemented using single metal layers [21], but the principles of IT filter design have also been extended to stacks comprising multiple, nominally identical, and evenly spaced metal films [2, 3], illustrating the close relationship between IT filters and the subsequently developed 'transparent metals' [6]. Consider the structure in Figure 4.3, which was designed as an induced transmission (IT) filter at ~530 nm wavelength. The 78 nm thick SiO_2 films are 'phase matching' layers, and the 91 nm thick SiO_2 films and 56 nm thick TiO_2 films are quarter-wave layers at 530 nm wavelength. The description of the IT design approach can be found elsewhere [3], but it is not difficult to verify the matching properties of this assembly. First, note that the two-period quarter-wave stack transforms the admittance according to $Y_A' \sim (1.45/2.35)^4 \cdot Y_A \sim 0.145$ (see Figure 4.3). The admittance Y_{out} is then given by equation (4.1) with $d_f = 78$ nm, $n_f = 1.45$, and $n_{sub} = Y_A' \sim 0.145$, resulting in $Y_{out} \sim 2.4+5.2i$, a value that is indeed close to the specified optimal value from above.

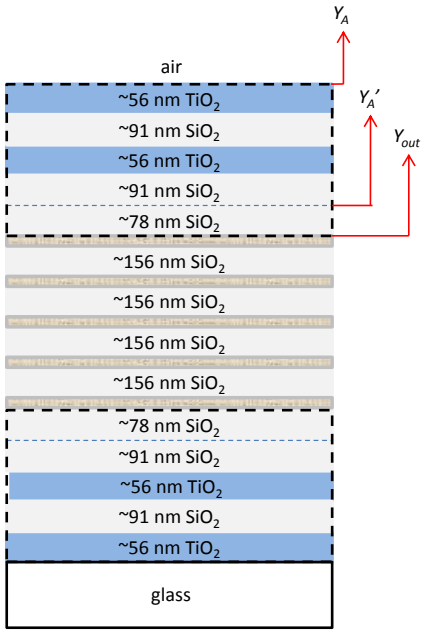

Figure 4.3 A schematic diagram representing experimental sample IT1 is shown. As for samples AR1 and AR2, the structure contains 5 Ag layers with nominal thickness ~25 nm each. The multilayer was designed as an 'induced transmission' filter with peak transmittance at ~530 nm wavelength.

For consistency with the other samples, we grew sample IT1 as a nominally symmetric structure. Since the exit medium is glass rather than air, this results in a slightly less optimal match at the output side (Y_{out}' ~ 2.95+4.2i), which could be improved by adjusting the phase matching layer. As shown below, the symmetric structure nevertheless provides $T \sim PT_{max}$ at the design wavelength. Finally, note that the individual Ag layers are spaced by SiO_2 layers with twice the thickness of the phase matching layer. This condition ensures that the admittance is optimized (at the design wavelength) for all of the metal films in the stack [3].

4.4 Results and discussion

Structures AR1, AR2, and IT1 were deposited using the evaporation system described in Section 2. Figure 4.4 (a) shows a cross-sectional TEM image of sample IT1, revealing good layer uniformity and dense microstructure. However, estimation of silver layer

thickness from TEM images was hindered by agglomeration of the silver into larger grains and void regions during the sample preparation, possibly during ion milling when locally elevated temperatures can be reached. This problem has previously been reported for thin silver films deposited on SiO_2 [22]. The estimated inter-metal SiO_2 layer thickness (~150 nm) is within typical 5% TEM magnification error of the target value (156 nm). All of the samples were observed and measured over the course of approximately 3 years. Samples AR1 and IT1 showed no significant change in appearance over that time, while sample AR2 developed a somewhat mottled and cloudy appearance (see Figure 4.4 (b)). We attribute this to the two Ag-TiO_2 interfaces present in sample AR2, which presumably led to gradual oxidation of the outermost Ag layers in the 5-period stack.

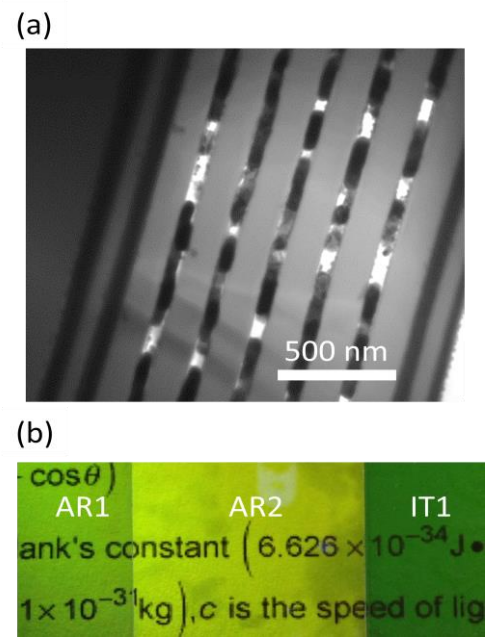

Figure 4.4 (a) Cross-sectional TEM image of structure IT1; the glass substrate is visible at the left part of the image. Note that sample polishing and preparation caused the Ag layers to appear erroneously thick. (b) Camera image showing the three aged samples in front of black text on a white sheet of paper. The mottled pattern on sample AR2 was not apparent immediately after deposition, but became more visible with time.

The transmittance of the samples was measured as described in Section 2, and typical results are plotted in Figure 4.5. Also plotted is the theoretically-predicted transmittance using the Ag model mentioned above, and for two different assumptions regarding the Ag film thickness (25 or 30 nm). As is well known, it is challenging to deposit (or measure the thickness of) such thin Ag films with an accuracy better than a few nanometers. Moreover, while we approximately verified the Ag optical constants model, the precise values are expected to vary with the film thickness [17].

Sample AR1 (Figure 4.5 (a)) exhibited a peak transmittance of ~0.55, in good agreement with the theoretical prediction based on the assumption of 25-nm-thick Ag films. However, the bandwidth and the shape of the transparency band are in better agreement with the theoretical curve that assumes 30-nm-thick Ag films. It is possible that the Ag model used in the simulations [20] overestimates the loss of our evaporated films, as we have speculated previously [23]. It is also likely that the experimental data is subject to random layer thickness errors, not taken into account by the simulation. In any case, sample AR1 is characterized by relatively low peak transmittance and significant ripple in the pass-band.

As shown in Figure 4.5 (b), using a higher-index AR layer for the matching assembly improves the peak transmittance, increases the transparency bandwidth, and reduces the pass-band ripple. As for sample AR1, theoretical fitting of the transparency band-width suggests that the as-fabricated Ag films are ~30 nm thick, while the level of transmittance suggests slightly thinner films. The comments regarding layer thickness errors and uncertainty in the Ag optical constants also apply to this sample. Nevertheless, it is interesting that some of the benefits of a high index dielectric [7, 13, 17] can be obtained by replacing only the SiO_2 'AR layers' (and not the inter-metal spacer layers) with TiO_2.

This illustrates the impedance matching issues discussed above, and might be a useful compromise for some applications.

Figure 4.5 (c) shows the results for sample IT1. The transfer matrix simulation (for the 25 nm thick Ag film assumption) confirms that $T_{max} \sim PT_{max}$ at the design wavelength as expected. The slight gap between the theoretical T_{max} and PT_{max} is due to the presence of the glass substrate, which was included in the transfer matrix simulation but neglected in the design of the matching assembly. Compared to sample AR2 in particular, note that the resonant nature of the IT matching assembly results in reduced transparency bandwidth. As for the first two samples, the experimental curve lies somewhat intermediate between the theoretical curves based on assumption of 25- and 30-nm-thick Ag films. The peak experimental transmittance (~0.7) is lower than the predicted peak transmittance (~0.79), which can partly be attributed to residual scattering by the films. Also, as evidenced by the two theoretical curves in Figure 4.5 (c), the IT design is quite sensitive to variations in layer thickness. Thus, it is likely that thickness errors also contribute to the discrepancy.

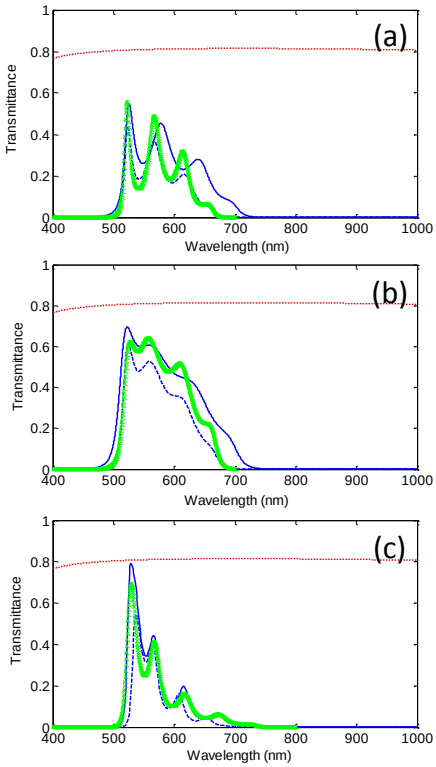

Figure 4.5 Comparison of experimental transmittance (green symbols) with theoretically predicted transmittance is shown for the three samples AR1, AR2, and IT1 described in the main text. In each plot, the red dotted curve is the predicted PT_{max} for a multilayer containing 5 Ag films each 25 nm thick. Also shown is the predicted transmittance as calculated assuming 25 nm (solid blue curves) or 30 nm (dashed blue curves) thick Ag films. (a) Results for sample AR1. (b) Results for sample AR2. (c) Results for sample IT1.

To summarize, the results confirm that it is possible, in principle, to add an admittance matching assembly that optimizes the transmittance of the Ag/SiO_2-based multilayer (i.e. $T_{max} \sim PT_{max}$) at a single wavelength. However, the resonant nature of the IT design implies bandwidth limitations and tight fabrication tolerances. On the other hand, the use of a single high-index AR layer provides significant improvement in optical properties over the basic design AR1, while not greatly increasing the complexity of the multilayer. Compared to the IT design, this approach is simpler and has improved fabrication tolerance, at the expense of only a slight reduction in peak transmittance. Overall, the experimental and theoretical results are in reasonable agreement. Slight

discrepancies are expected, given the use of 'bulk' Ag optical constants [20] for modeling purposes, whereas thin Ag films are expected to exhibit higher loss arising from roughness-induced scattering [17].

For many applications, such as the implementation of electromagnetic shields with visible-band transparency [12], the angular dependence of the transparency band is an important issue [17]. Figure 4.6 shows the polarization-averaged transmittance of samples AR1 and AR2, for incidence angles of 10, 30, and 40 degrees. In addition to higher transparency, sample AR2 is characterized by less variation in its pass-band as the incidence angle varies.

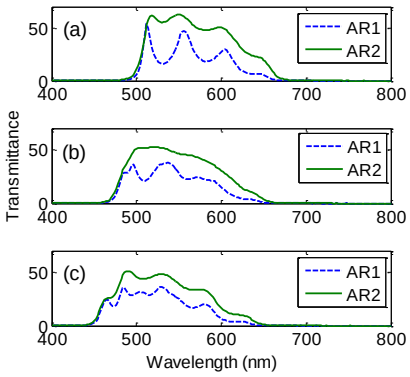

Figure 4.6 Plots of transmittance at different incidence angles are shown for samples AR1 and AR2: (a) 10 degrees, (b) 30 degrees, (c) 40 degrees. The measurements were taken using an unpolarized source, and thus represent the average of TE and TM transmittance in each case.

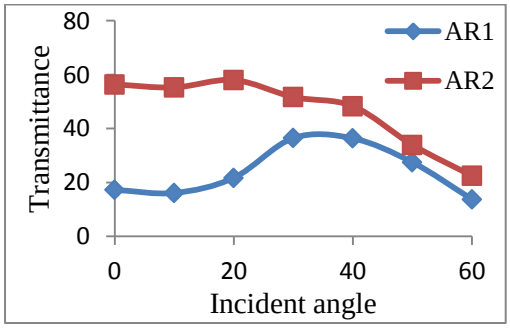

Figure 4.7 Polarization-averaged transmittance is plotted versus incident angles for samples AR1 and AR2 at 530 nm wavelength.

Furthermore, Figure 4.7 shows the polarization-averaged transmittance versus incident angles for samples AR1 and AR2 at 530 nm wavelength. The angle dependence for sample AR2 is relatively weak since the fluctuation in transmittance is less than 10% when incident angle is below 40 degrees. For sample AR1, the angle dependence is quite large as there is a transmittance peak located between 30 degree and 40 degrees. To further illustrate the angle dependence for each sample, Figure 4.8 shows a plot of percentage difference in transmittance for oblique angles of incidence relative to the normal incidence. Sample AR1 (i.e. Figure 4.8 (a)) again shows curves with large oscillations, indicating that the transmittance is relatively dependent on the incident angles. Sample AR2 (i.e. Figure 4.8 (b)) shows antisymmetric curves at ~ 530nm wavelength, beyond which the curves are relatively flat compare to sample AR1, indicating less dependency on the incident angles.

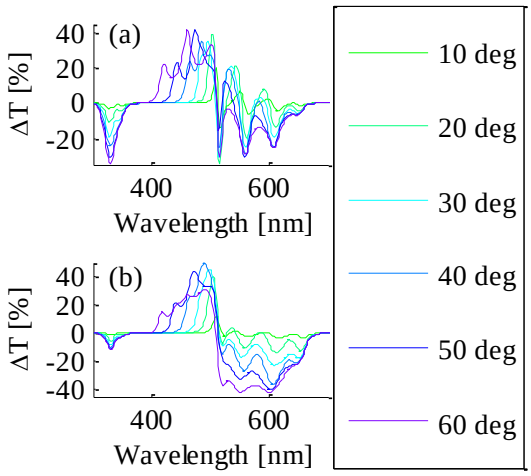

Figure 4.8 Angle dependence plot for sample AR1 (a) and AR2 (b). Note that the data is normalized with respect to scans of a blank slide and the transmittance is polarization-averaged for TM and TE.

Finally, Figure 4.9 shows the transmittance spectra for samples AR1 and AR2, as measured at 1 month, 2 years, and 3 years after deposition. The samples were stored at room temperature in air, and dust was removed prior to measurements by using a

pressurized nitrogen gun. Both samples exhibited a slight shift towards shorter wavelength with time. This might be attributable to densification of the thin films, assuming the decrease in layer thickness dominates over any attendant increase in refractive index. Both samples also exhibited slight reduction in transparency with time, possibly due to Ag oxidation and possibly due to contamination of the sample surface. Interestingly, the degradation for sample AR2 was not significantly greater than that for AR1, in spite of the change in appearance mentioned above (see Figure 4.4). Further improvement in stability might be possible by adding a thin inter-layer (such as Ti [12] or SiO_2) between the TiO_2 and Ag layers.

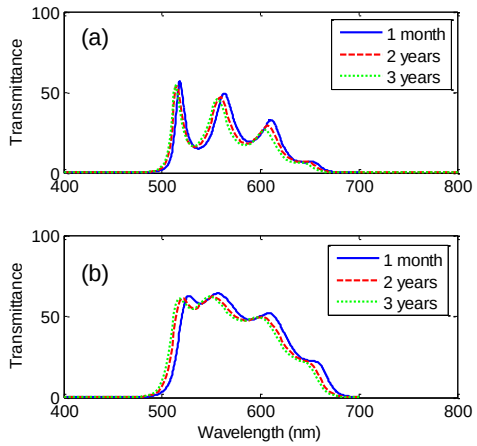

Figure 4.9 Plots of transmittance measured at various times after deposition, as indicated by the legend: (a) sample AR1, (b) sample AR2. The samples were stored in air at room temperature.

4.5 Summary and Conclusions

We considered the practically important case where a metal-dielectric stack employs low-index dielectric spacer layers (ex. Ag with SiO_2 spacers). Using a QWS-based (ex. TiO_2/SiO_2-based) matching assembly at each end of the multilayer, and in keeping with long-established procedures for the design of IT filters, the transparency at a given wavelength is limited only by the maximum potential transmittance of the metal layers.

While the IT design suffers from reduced transmission bandwidth and more demanding fabrication, it is nevertheless potentially useful for narrowband applications requiring optimal transparency. A simpler alternative, useful for applications requiring broadband transparency, is the addition of a single high-index matching layer at each end of the stack. Compared to the use of low-index (ex. SiO_2) matching layers, high-index (ex. TiO_2) matching layers significantly enhance the peak transmittance, spectral bandwidth, and angular bandwidth of the filter.

References

[1] P. W. Baumeister, "Radiant power flow and absorptance in thin films," *Appl. Opt.*, vol. 8, pp. 423-436, (1969).

[2] H. A. Macleod, "A New Approach to the Design of Metal-dielectric Thin-film Optical Coatings," *Optica Acta: International Journal of Optics,* vol. 25, pp. 93-106, (1978).

[3] H. A. Macleod, "Thin-Film Optical Filters," in *Chapter 8*, 3 ed., Institute of Physics Publishing, 2010.

[4] P. H. Berning and A. F. Turner, "Induced transmission in absorbing films applied to band pass filter design," *J. Opt. Soc. Am.,* vol. 47, pp. 230-239, (1957).

[5] P. H. Lissberger, "Coatings with induced transmission," *Appl. Opt.*, vol. 20, pp. 95-104, (1981).

[6] M. J. Bolemer and M. Scalora, "Transmissive properties of Ag/MgF2 photonic band gaps," *Appl. Phys. Lett.,* vol. 72, pp. 1676-1678, (1998).

[7] M. Scalora, M. J. Bloemer and C. M. Bowden, "Laminated photonic band structures

with high conductivity and high transparency: metals under a new light," *Optics and Photonics News*, vol. 10, pp. 24-27, (1999).

[8] G. Leftheriotis, P. Yianoulis and D. Patrikios, "Design and optical properties of optimized ZnS/Ag/ZnS thin films for energy saving applications," *Thin Sol. Films*, vol. 306, pp. 92-99, (1997).

[9] R. S. Bennink, Y. K. Yoon, R. W. Boyd and J. E. Sipe, "Accessing the optical nonlinearity of metals with metal- dielectric photonic bandgap structures," *Opt. Lett.*, vol. 24, pp. 1416-1418, (1999).

[10] M. J. Bloemer, G. D'Aguanno, N. Mattiucci, M. Scalora and N. Akozbek, "Broadband super-resolving lens with high transparency in the visible range," *Appl. Phys. Lett.*, vol. 90, p. 174113, (2007).

[11] C. S. Kee, K. Kim and H. Lim, "Optical resonant transmission in metal-dielectric multilayers," *J. Opt. A: Pure Appl. Opt.*, vol. 6, pp. 267-269, (1999).

[12] M. S. Sarto, R. L. Voti, F. Sarto and M. C. Larciprete, "Nanolayered lightweight flexible shields with multidirectional optical transparency," *IEEE Trans. Electromagn. Compat.*, vol. 47, pp. 602-611, (2005).

[13] Y. K. Choi, Y. K. Ha, J. E. Kim, H. Y. Park and K. Kim, "Antireflection film in one-dimensional metallo-dielectric photonic crystals," *Opt. Comm.*, vol. 230, pp. 239-243, (2004).

[14] T. W. Allen and R. G. DeCorby, "Assessing the maximum transmittance of periodic metal-dielectric multilayers," *JOSA B*, vol. 28, no. 10, pp. 2529-2536, (2011).

[15] T. W. Allen and R. G. DeCorby, "Conditions for admittance-matched tunneling through symmetric metal-dielectric stacks," *Optics Express*, vol. 20, no. 55, pp.

A578-A588, (2012).

[16] M. S. Sarto, F. Sarto, M. C. Larciprete, M. Scalora, M. D'Amore, C. Sibilia and M. Bertolotti, "Nanotechnology of transparent metals for radio frequency electromagnetic shielding," *IEEE Trans. Electromagn. Compat.,* vol. 45, p. 586, (2003).

[17] D. Owens, C. Fuentes-Hernandez and B. Kippelen, "Optical properties of one-dimensional metal-dielectric photonic band-gap structures with low-index dielectrics," *Thin Sol. Films,* vol. 517, pp. 2736-2741, (2009).

[18] S. Y. Kim, "Simultaneous determination of refractive index, extinction coefficient, and void distribution of titanium dioxide thin film by optical methods," *Appl. Opt.,* vol. 35, pp. 6703-6707, (1996).

[19] P. Yeh, Optical Waves in Layered Media, Wiley, 2005.

[20] A. D. Rakic, A. B. Djurisic, J. M. Elazar and M. L. Majewski, "Optical Properties of Metallic Films for Vertical-Cavity Optoelectronic Devices," *Applied Optics*, vol. 37, no. 22, pp. 5271-5283, (1998).

[21] A. Piegari and J. Buler, "Variable narrowband transmission filters with a wide rejection band for spectrometry," *Appl. Opt.,* vol. 45, pp. 3768-3773, (2006).

[22] H. C. Kim, T. L. Alford and D. R. Allee, "Thickness dependence on the thermal stability of silver thin films," *Appl. Phys. Lett.,* vol. 81, pp. 4287-4289, (2002).

[23] M. C. Zhang, T. W. Allen and R. G. DeCorby, "Experimental study of optimized surface-plasmon-mediated tunneling in metal-dielectric multilayers," *Appl. Phys. Lett.,* vol. 103, p. 071109, (2013).

Chapter 5 Tunneling of TE-polarized light through dielectric-metal-dielectric stacks

5.1 Introduction

Light propagation in periodic dielectric (or metal-dielectric) structures, often known as photonic crystals (PCs), has been extensively studied. This is motivated by the fact that the propagation, emission, and absorption of light can be significantly altered by such structures [1, 2, 3].The optical properties of PCs are investigated based on the photonic band structure, which is analogous to the electronic band structure in crystals. Furthermore, the analogy between photon and electron propagation has received much attention in the context of tunneling, where waves or particles may penetrate through classically impenetrable barriers. Historically, optical physicists have studied this analogy using structures that involve frustrated total internal reflection (FTIR).

In a typical FTIR system, two prisms are brought close to each other, such that the air gap (or other low-index layer) in between acts as a tunnel barrier. Metal layers can also act as tunnel barriers, because light within them decays exponentially with distance. In fact, there is an exact analogy between the lossless metal (in which fields exhibit pure exponential decay) and the dielectric tunnel barrier [4]. However, while the dielectric tunnel barrier requires angles of incidence beyond the critical angle for TIR, the (lossless) metal layer is a tunnel barrier for all angles of incidence. Thus, the DMD structures studied in Chapter 3 can be viewed as multiple barrier systems, also known as resonant tunneling structures [4]. Surface-plasmon mediated tunneling for such structures was discussed in Chapter 3. In this chapter, we focus on the tunneling by TE-polarized light, where the metal dielectric stack can be viewed as a series of coupled Fabry-Perot

cavities. We also describe preliminary experiments aimed at controlling the spatial and spectral emission profile for fluorescent dyes embedded within these MD stacks.

5.2 Sample design

Tunneling of TE-polarized light was studied by embedding the DMD (TiO_2-Ag-TiO_2) multilayers between two low-index prisms (ex. pellin broca prisms made from BK7) such that $n_1 > n_2$, enabling the incident propagating wave inside the prism to propagate via Fabry-Perot resonances within the DMD structure (see Figure 5.1).

As discussed in Chapter 2, admittance-matched tunneling for a given Ag layer thickness (d_m) and wavelength requires specific values for the dielectric index and thickness. However, since the imaginary part of the refractive index of a metal is very high, to perfectly match the admittance at normal incidence requires impractically large refractive index for the dielectric ($n_1 > 4$) [5]. Nevertheless, as discussed elsewhere [6], admittance-matched tunneling for TE-polarized light at off-normal incidence is possible with lower-index dielectrics. For a given value of n_1 and n_2, solutions to equations (2.6) – (2.10) predict specific values of incidence angle, dielectric index, and dielectric layer thickness for which admittance-matched tunneling occurs. In the theoretical work described below, we used a Forouhi-Bloomer model for TiO_2 from Kim *et al*. [7] (which gives $n_1 = 2.3594$ at 500 nm wavelength), and a standard Sellmeier expression for fused silica (which gives $n_2 = 1.4623$ at 500 nm wavelength). Ag optical constants were modeled using the Rakic model [8] described in Chapter 2. Based on this, the admittance matching equation predicts a match at 80.88^o, for a dielectric thickness of 52.76 nm, as shown in Figure 5.2 (a) and (b).

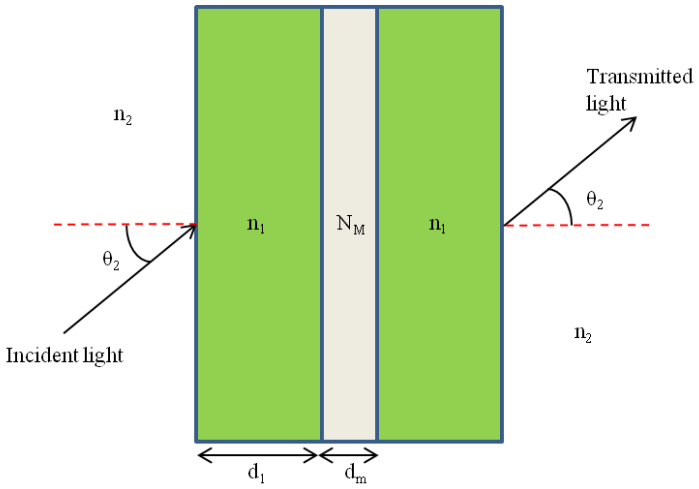

Figure 5.1 Schematic illustration of a one period DMD unit cell. The unit cell is composed of one thin metal film with index N_M embedded between two dielectric films with index n_1, and is surrounded by media with index n_2.

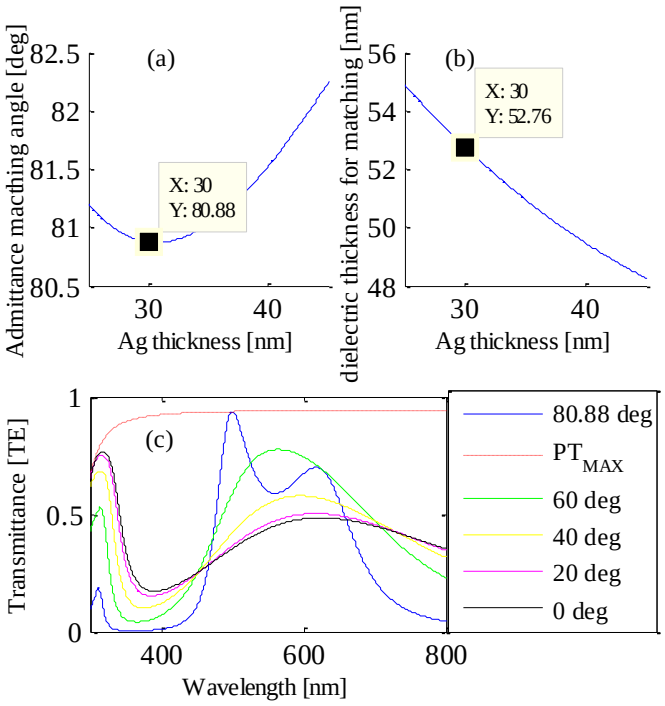

Figure 5.2 (a) The incident angle (inside the prism) required for admittance-matched tunneling of TE-polarized incident light at 500 nm wavelength through a one period DMD stack (with an Ag metal layer, TiO_2 dielectric layers, and BK7 prism ambient) is plotted versus metal thickness. (b) The minimum dielectric layers thickness that results in admittance-matched tunneling when combined with the incident angles in part (a). (c) Predicted transmittance versus wavelength for TE-polarized light at various incident angles and for the dielectric thickness (i.e. 52.76 nm) indicated in part (b), for a one

period DMD stack with d_m = 30 nm. Note that admittance-matched tunneling ($T = PT_{MAX}$) is verified for an incident angle of 80.88^o and at a wavelength of 500 nm, as predicted by the curve in (a).

Figure 5.2 (c) shows the transmittance plotted versus wavelength of TE-polarized incident light for the structure predicted by the admittance matching equations. The red dotted curve represents the PT_{MAX} for a structure containing a single 30 nm thick Ag layer. The transfer-matrix simulations verify that an admittance-match ($T = PT_{MAX}$) is achieved for the conditions predicted by the equations (i.e. d_1 = 52.76 nm, d_m = 30 nm, and for an incident angle of 80.88^o at 500 nm wavelength). This basic structure (i.e. d_m ~ 30 nm and d_1 ~ 50 nm) was used for the TE tunneling studies described below.

5.3 Experimental setup and results

1-, 2-, and 3-period TiO_2-Ag-TiO_2 samples were deposited on clean microscope slide substrates using a six-pocket electron-beam evaporator. For each sample, the layers were sequentially deposited in the evaporator without breaking vacuum. In keeping with the simulations described above, nominal layer thicknesses of d_m ~ 30 nm (for Ag) and d_1 ~ 50 nm (for TiO_2) were targeted. A more detailed description of the deposition parameters and procedures can be found in Appendix A.

A custom-built, double-prism system was used to measure the transmittance of TE-polarized light as a function of wavelength, at a fixed incident angle inside a spectrophometer (Perkin-Elmer Lambda 900), as shown in Figure 5.3 (b). The sample holder consisted of two BK7 glass pellin broca prisms (i.e. a trapezoidal prism with two adjacent 90^o corners and the third corner of ~ 78^o), where the long sides were aligned face-to-face, with the sample sitting in between. This arrangement is shown schematically in Figure 5.3 (a). An index matching fluid (Hydrogentaed Terphenyl, Cargille 1809Y) was used between the sample and the prisms. To facilitate incidence at

the near-grazing angles required by the admittance-matched solution (i.e. ~ 80^o inside the prism), light was made to be incident on the short side of the input coupling prism, as shown in Figure 5.3 (a). For example, normal incidence on this face of the prism corresponds to an incident angle of ~ 78^o on the DMD structure.

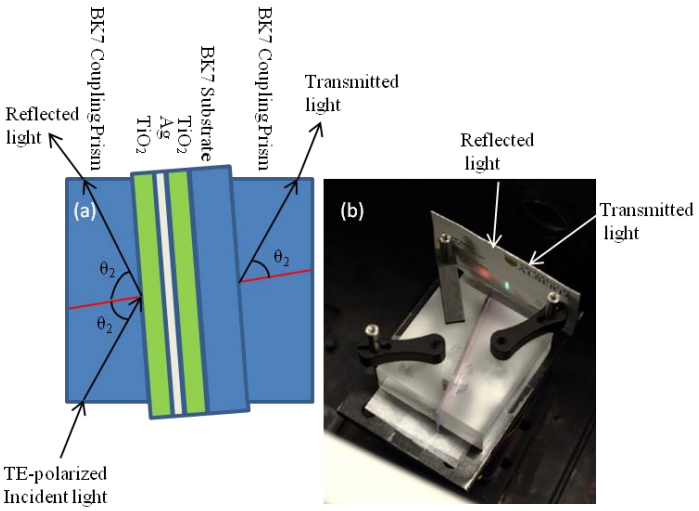

Figure 5.3 (a) A schematic illustration of the double-prism-coupler sample holder. (b) A picture of the experimental setup, including the double-prism-coupled sample illuminated inside a spectrophotometer. The reflected and transmitted light spots are visible in reflection from the white card held at the output side of the coupler.

All experimental data were calibrated before comparing to the simulated data. Transmittance scans for standalone samples were normalized with respect to a transmittance scan of the visible spectrum of a plain BK7 substrate. For measurements taken with the double-prism setup, transmittance scans were normalized with respect to the transmittance scan of the visible spectrum of a plain BK7 substrate mounted in the same double-prism setup.

Figure 5.4 shows the transmittance scan of the visible spectrum for both the standalone samples at normal incidence (left column) and for samples mounted in the double-prism setup at an incident angle near the matching angle (right column). As mentioned above, the targeted TiO_2 thickness was 50 nm. However, in the simulation

plots, we found that a better fitting was achieved by setting the TiO_2 thickness to be 50 nm, 45 nm, and 48nm for one-, two-, and three-period samples, respectively. This level of variation is well within the range (few percent) expected for the e-beam deposited layers. For the prism-coupled case (i.e. the right column of Figure 5.4), the simulation results show a perfect match near the design wavelength (i.e. 500 nm). Thinner dielectric layers result in a slight shift of the whole curve towards shorter wavelength, as can be seen by comparing plots for different period samples. For each sample, multiple scans (not shown) were taken at a series of incidence angles within a short range of the matching angle (i.e. the matching angle ± 6 degrees). It was found that the angle (inside the prism) of peak transmittance was ~ 81 degrees, which is very close to the predicted value above. Note that the uncertainty in the TiO_2 thickness also results in some uncertainty in the matching angle. Compared to the prism coupled case, the experimental results for the standalone samples at normal incidence (i.e. the left column of Figure 5.4) were found to be in better agreement with theoretical predictions, especially for the 1- and 3- period structure. This is probably due in part to greater scattering by the thin film interfaces in the case of near-grazing incidence. Generally speaking, the experimental results showed good agreement with the simulated results in terms of shape and location of the transparency band.

For further insight, transmission scans were also obtained at high incidence angles for the bare, 3-period sample (i.e. without prism coupling). As shown in Figure 5.5, better agreement between theory and experiment was obtained in this case. This suggests that the prism-coupled results might have been affected by additional experimental errors, such as imperfect contact between the prisms and the samples. The prism coupling experiments were difficult to reproduce, due to challenges associated with cleaning index-matching fluids from the samples without damaging the thin-film multilayers. In

future work, it is recommended that multiple, nominally identical samples should be grown to facilitate a greater number of experiments.

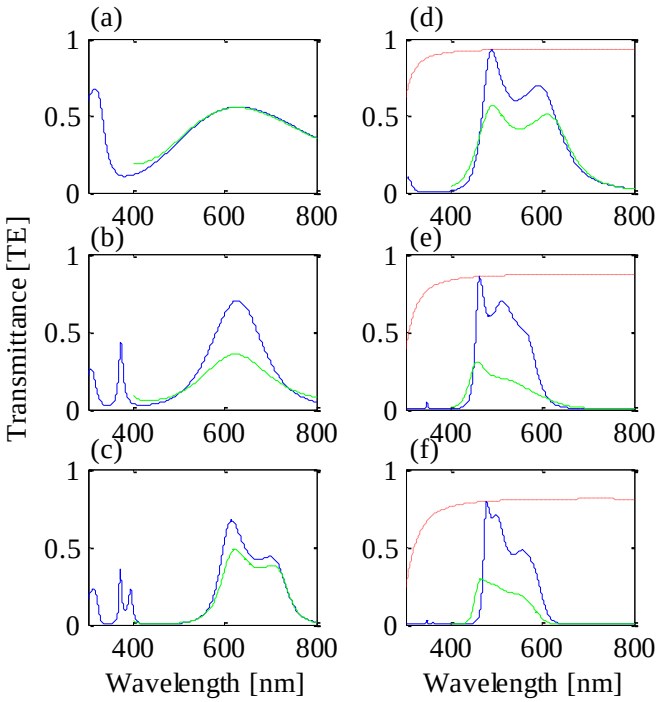

Figure 5.4 The experimental (green) and theoretical (blue) transmittance of TE-polarized light is plotted versus wavelength for one- (a), two- (b), and three- (c) period standalone samples at normal incidence, and for one- (d), two- (e), and three- (f) period samples mounted in the prism-coupled sample holder at an incident angle (i.e. θ_2) of ~ 81 degrees. The red dotted curve indicates PT_{MAX} for each case. Note that the TiO_2 thicknesses used in simulation (i.e. blue curves) are 50 nm, 45 nm, and 48 nm for one- (i.e. first row), two- (i.e. second row), and three-period samples (i.e. third row), respectively. Also note that for all theoretical plots, the Ag thickness was assumed to be 32 nm.

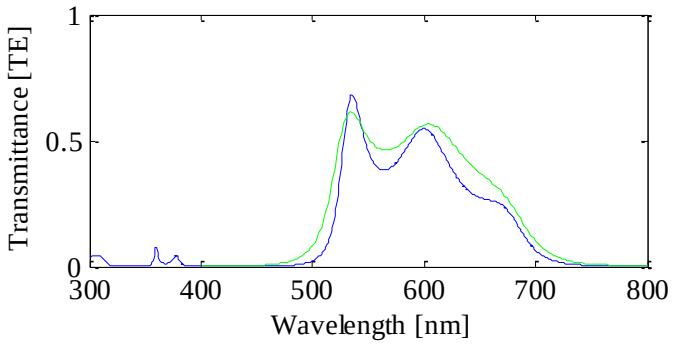

Figure 5.5 The experimental (green) and theoretical (blue) transmittance of TE-polarized light is plotted versus wavelength for the 3-period standalone sample at 80 degrees

incident angle in air. Note that the simulation parameters are identical to those used in Figure 5.4.

Figure 5.6 shows the spatial distribution of the field intensity (as predicted using transfer matrix simulations) for the 1-, 2- and 3-period samples under the admittance-matched conditions mentioned above. The field profiles reveal standing wave behavior in the TiO_2 layers, indicating that the tunneling is mediated by Fabry-Perot resonances. However, in contrast with the field profile in a conventional Fabry-Perot cavity, there is no build-up of field in the dielectric spacer layers (i.e. the peak intensity throughout the structure remains below the incident intensity). This is because the structure is admittance-matched (i.e. index-matched) to the external media under these tunneling conditions, such that reflections at each end of the structure are actually minimized [6]. Also note that the electric field is smallest at the positions of the metal films, as is necessary for low-loss tunneling through a metal-dielectric multilayer [9].

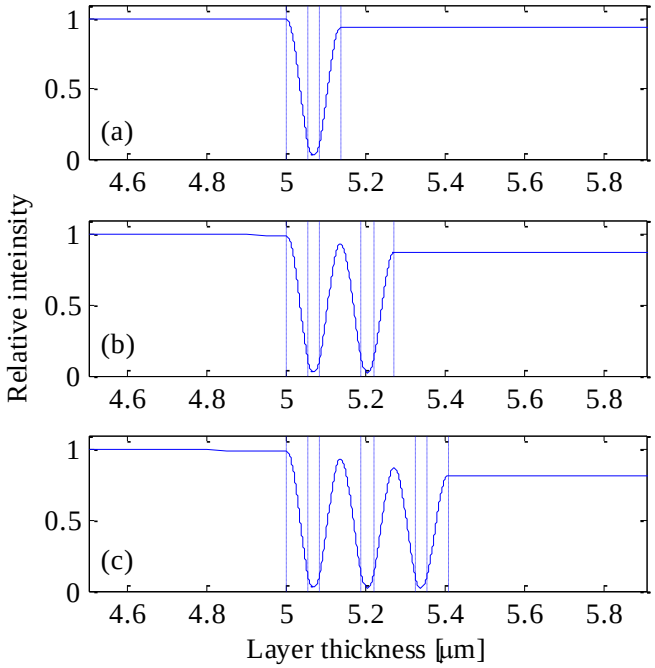

Figure 5.6 Theoretically predicted spatial intensity distribution for one (a), two (b), and three (c) period DMD multilayers, with n_2 = 1.4623, n_1 = 2.3594, N_m = 0.1321 – 2.7625i,

d_1 = 52.76 nm, d_m = 30 nm, for 80.88 degrees incident angle at 500 nm wavelength. The vertical dashed lines indicate the layer interfaces.

5.4 Preliminary studies on modification of spontaneous emission by DMD structures

It is clear from the results described in the previous section, and in earlier chapters, that periodic DMD structures exhibit unique spectral and spatial transmission properties. Over the past 2-3 decades, there has been considerable interest in using PCs to control or modify the spontaneous emission from embedded active emitters [10, 11, 12, 13]. Much of this work has employed 1-D periodic media, such as dielectric Bragg reflectors. For example, Tocci *et al.* [14] demonstrated the band-gap suppression and band-edge enhancement of spontaneous emission from a sandwiched active layer. It is worth noting that the transparency band of a periodic MD structures (i.e. 'transparent metals' [15]) is precisely located at the long-wavelength edge of the fundamental stop-band. This is apparent from the lower-left plot in Figure 5.4 above, for example. The stop-band of the 3-period DMD structure lies between ~ 400 and ~ 600 nm, and the main transparency band lies adjacent to this stop-band, on the long wavelength side. As incident angle increases (particularly for TE-polarized light), the stop-band (and therefore the band-edge transparency region) shifts to shorter wavelengths. Also, since the admittance-match for TE light improves with increasing angle, the peak transmittance increases, reaching a maximum at the matching angle described above (for example, compare the plots in Figure 5.4 (c) and (f)). This behavior is made clearer by the plots provided below.

While much of the work on spontaneous emission modification has used all-dielectric periodic structures, there are unique aspects of metal-dielectric structures that have also captured interest [16, 17]. First, metal-based mirrors are inherently omnidirectional, which in some cases enables greater control over the spectral emission profile. Second,

many important practical devices, such as organic LEDs [18], require semi-transparent conductive contacts. Third, recent work on so-called ‘hyperbolic metamaterials’ [19] has suggested that layered MD structures can in some cases lead to giant enhancement of spontaneous emission into a small number of propagating modes. This latter research might lead to new types of highly efficient and controllable light sources.

These facts prompted us to pursue a preliminary set of experiments using fluorescent dyes and the TE-polarized tunneling samples described above. A manual assembly process was used to embed nm-scale fluorescent beads (Fluospheres, Invitrogen) between pieces of the 3-period DMD structure, forming a sandwich structure as illustrated in Figure 5.7. The 3-period sample was chosen due to its distinct transparency band from normal incidence to near-grazing angles, as shown both in Figure 5.4 and Figure 5.5. The dyes were pumped using various laser sources, and their spatial and spectral emission properties were considered as described below.

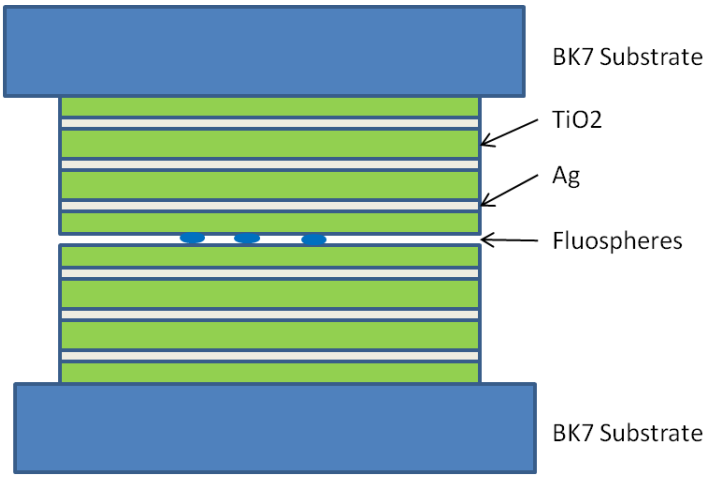

Figure 5.7 Schematic illustration of the manually assembled samples is shown. A small quantity of fluorescent beads (fluospheres, Invitrogen) were ‘sandwiched’ between two pieces of the three-period MD stack.

5.4.1 Sample fabrication and experimental setup

Two types of fluospheres (i.e. plastic microspheres embedded with fluorescent dyes) were used to construct samples. One was a 0.04 μm diameter yellow-green fluosphere (Invitrogen F-8795) that has a peak excitation wavelength of 505 nm and a peak emission wavelength of 515 nm. The other was a 0.02 μm diameter blue fluosphere (Invitrogen F-8781) with a peak excitation wavelength of 365 nm and a peak emission wavelength of 415 nm. The spectral plots provided by the manufacture for these two types of fluospheres are shown in Figure 5.8. The 3-period sample was cut into 1 inch square pieces using a diamond bladed dicing saw. A small drop of fluosphere in solution was placed near the center of one piece, the solvent was allowed to evaporate, and two square pieces were aligned so that the thin film sides were facing each other. The schematic of the sandwiched structure is illustrated in Figure 5.7. The samples were bonded at each corner using an optical adhesive (Norland NOA-61) and then cured with UV light for 15 minutes.

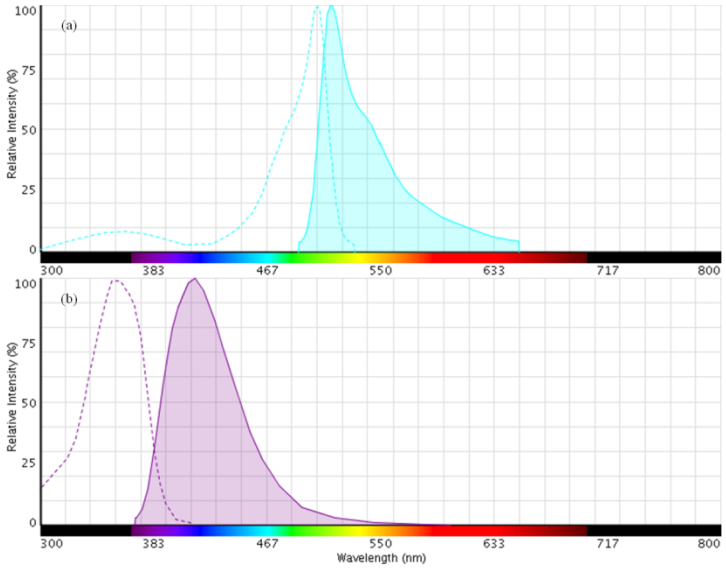

Figure 5.8 Fluorescence excitation (dotted line) and emission (solid line) spectra for the yellow-green fluosphere (a) and blue fluosphere (b) are shown. Note that these plots were taken from the Invitrogen website.

The bound samples were illuminated by laser sources with the incoming light beam perpendicular to the sample surfaces to excite the embedded fluospheres (see Figure 5.9). A 473 nm blue laser (LaserGlow, RS-0473-PFM-0050-10) was used to excite the sample containing the yellow-green fluospheres and a 375 nm UV laser (Coherent, Radius 375 1053595/AE) was used to excite the sample containing the blue fluospheres. Note that the metal-dielectric filter exhibits a partial transparency band near 375 nm at normal incidence (see Figure 5.4), but is relatively opaque to light at 473 nm. Nevertheless, the embedded fluospheres could be excited in both samples. Higher excitation power (up to ~ 50 mW) was available from the blue laser, and strong fluorescence was clearly visible from the yellow-green fluospheres, as described below. To facilitate collection of spontaneous emission, a 5x objective lens was used to focus on the fluospheres. Furthermore, long pass filters (with cutoff at either 395 nm or 495 nm) were used to suppress residual excitation light prior to the detection. For inspecting from the edges, a TE (or TM) polarizer was used to analyze the polarization of the emission guided by the sample. The schematic of the experiment setup is presented in Figure 5.9. At the detection points, fluorescence was collected using either a camera or the pick-up fiber of a spectrometer (OceanOptics, P1000-2-UV/VIS).

Note that the laser polarization was also controlled, although at normal incidence it always corresponds to in-plane (TE) polarization. The polarization of fluorescence emission is typically aligned with the polarization of the excitation source [20], especially when the dye molecules are bound in a solid plastic host and thus are not free to rotate. This means the fluorescence should result primarily from in-plane electric dipole moments under these experimental conditions. As explained in the literature [21, 22], in-plane (or horizontal) dipole emitters embedded within a planar multilayer will radiate light into both TE- and TM-polarized modes of the structure. The mix of TE and TM

depends on the viewing angle relative to the axis of the dipole and the plane of the multilayer, as illustrated in Figure 5.10. For a collection of in-plane dipoles with random orientation in the azimuthal direction (i.e. within the plane), the ratio of TE- to TM-polarized emission is expected to be 3:1 [22]. In the preliminary study described here, most of these details were neglected. Nevertheless, it was expected that the embedded fluospheres would emit mainly TE polarized light, even neglecting the effects of the MD stacks. In the treatment below, we consider mainly the emission and propagation of TE-polarized light within the samples.

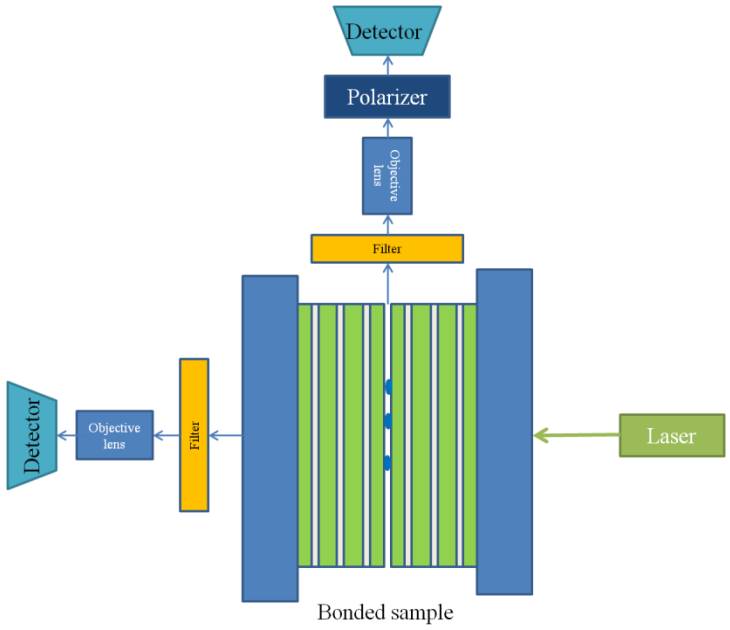

Figure 5.9 Schematic illustration of the experimental setup used to assess the spatial, spectral and polarization dependence of the fluorescence emitted by the fluospheres embedded in the 'sandwich' samples.

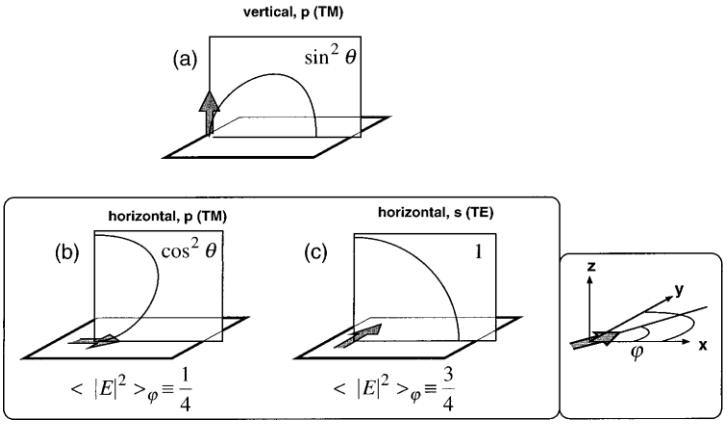

Figure 5.10 Vertical (a) and horizontal ((b) and (c)) dipole emission patterns in free space. Note that the rightmost figure on the second row is the azimuthal average for the horizontal dipoles. [22]

Figure 5.11 shows the predicted transmittance versus wavelength for the bonded samples without (a) and with (b) the assumption of a fluosphere 'spacer' layer in the center, and at various incident angles inside the glass substrate. Assuming intimate contact between the two 3-period samples, the sandwich structure is simply a 6-period DMD stack with the same matching conditions. Thus, as shown in Figure 5.11 (a), the transmittance of TE-polarized light increases with increasing incidence angle and reaches a maximum at ~80 degrees where the structure is admittance matched.

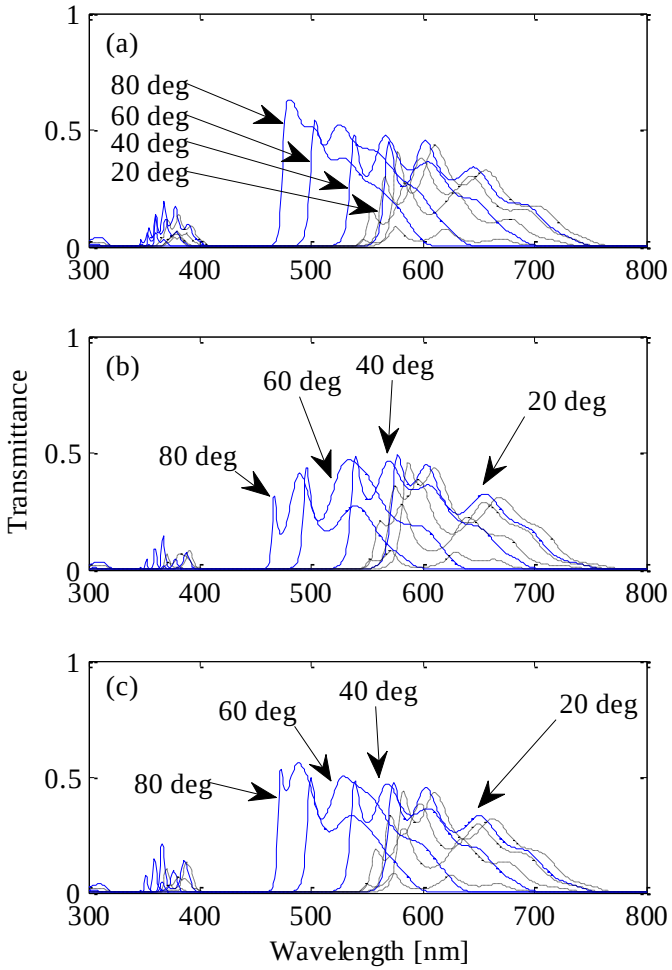

Figure 5.11 Transmittance is plotted versus wavelength for a bonded (see Figure 5.7) six period TiO_2-Ag-TiO_2 sample with 48 nm thick dielectric layer and 32 nm thick metal layer at 20, 40, 60, and 80 degrees incident angles (inside the glass substrate 'ambient' medium) for both TE (blue solid curves) and TM (black dotted curves) polarized incident light. Note that (a) is without an assumption of a fluosphere layer, (b) is with the assumption of a fluosphere layer with an index of 1 and 40 nm thickness representing the yellow-green fluosphere sample, and (c) is with the assumption of a fluosphere layer with an index of 1 and 20 nm thickness representing the blue fluosphere sample.

The possibility of non-intimate contact, which is likely the case in practice, was also considered. For simplicity, the 'spacer layer' was assumed to have the thickness of the fluospheres and a refractive index of 1. This is justified by the fact that individual fluospheres were expected to be surrounded by air in the actual samples, although

verification of this assumption is left for future work. With the presence of a fluosphere 'spacer' layer, the simulated transmittance is modified slightly as shown in Figure 5.11 (b) and (c): the secondary peaks are reduced and the overall curve is shifted towards shorter wavelength. Furthermore, theses shifts are larger for the thicker spacer layer.

Based on the angular and spectral dependence of the TE transmittance, some general comments can be made about the anticipated modification of the spontaneous emission from the embedded fluospheres (see Figure 5.12):

i. For emission into near-normal-incidence directions, the emitted light should have enhanced spectral content in the main transparency bands between ~ 600 nm and ~750 nm and just below ~400 nm, and reduced spectral content in the stop band between ~ 400 and ~ 550 nm. For both samples described above, the peak of the fluoshpere emission band lies within the stop-band of the multilayer. Thus, it is expected that the emission into near-normal directions should exhibit higher spectral content in the vicinity of the transparency bands mentioned, and reduced spectral content in the range of the stop band mentioned, compared to the native emission spectrum of the dye.

ii. For emission into off-normal directions and for increasing angles, the MD stack becomes increasingly transparent (i.e. for TE polarized light), and the transparency band shifts to shorter and shorter wavelengths (see Figure 5.11). Thus, it is expected that the off-normal light will be blue-shifted (i.e. contain a higher proportion of shorter-wavelength light) relative to the light emitted normal to the layers. Furthermore, any light emitted at angles higher than the critical angle for total internal reflection at the substrate-air interface (~40 degrees) is expected to be trapped inside the substrate and guided towards the

edge of the sample. At the edge of the sample, much of this substrate-guided light should be transmitted externally.

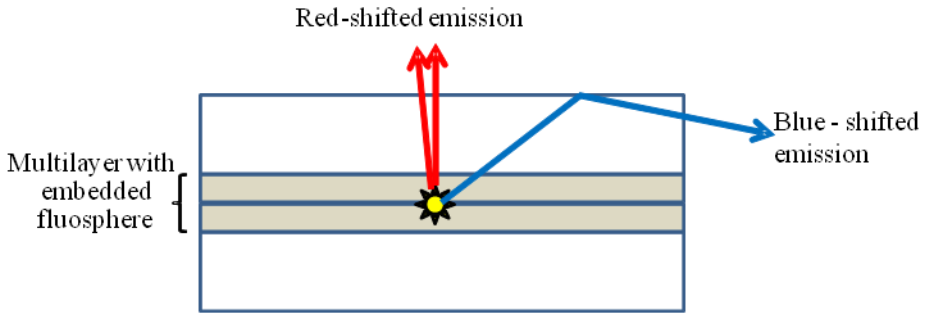

Figure 5.12 Schematic diagram showing the expected modification of the TE emission spectrum for the fluospheres sandwiched within the multilayer structure. It is assumed that the native fluorescence peak of the fluosphere lies within the normal-incidence stop-band of the periodic multilayer, as is the case for the samples described here. The edge emission is expected to be somewhat blue-shifted compared to the surface emission, and vice-versa.

In summary, we expected these samples to exhibit fluorescence that is modified by the available propagating modes (i.e. the transparency bands) of the DMD stacks. The experimental setup shown in Figure 5.9 was designed to enable a comparison of the light emitted into near-normal directions and the light emitted from the edge of the samples.

Another important issue that impacts the rate of spontaneous emission into a given mode (i.e. into a given direction and polarization state for the planar multilayer structure) is the magnitude of the normalized mode field at the location of the emitter [14]. As an example, Figure 5.13 plots the intensity profile for the 6-period 'sandwich' structure (i.e. neglecting a spacer layer), at the admittance-matched angle (~81 degrees inside the glass substrate) and for TE-polarized light. Because the field intensity is high at the center of the structure (i.e. the fluosphere is at an anti-node of the field), emission into this direction would be further favored. A complete treatment of these details is left for future work.

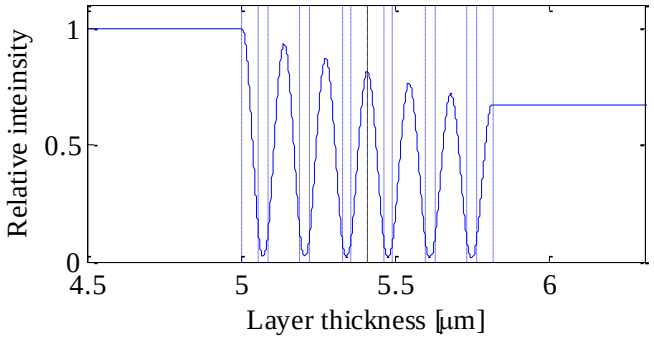

Figure 5.13 Theoretically predicted spatial intensity distribution for the bonded sample, neglecting the fluosphere layer. TE polarized light incident at the admittance-matched angle (~81 degrees) was assumed. Note that the black dashed line indicates the position of the fluosphere layer (assumed to have zero thickness) inside the sample.

5.4.2 Results

The experimental setup shown in Figure 5.9 was use to conduct a preliminary assessment of the fluorescence emitted by the two samples described above. The primary goal of this preliminary work was to test the predictions summarized in Figure 5.12.

5.4.2.1 Yellow-green fluospheres

As mentioned, the yellow-green fluosphere has an emission peak at 515 nm (see Figure 5.8 (a)), which lies within the stop-band of the DMD stacks at normal incidence. However, as shown in Figure 5.4, the stacks become quite transparent to light at this wavelength for TE polarization and angles higher than ~40 degrees. Thus, it was anticipated that the fluorescence emitted from the top surface of the sample (i.e. at near-normal directions) would exhibit a red-shift relative to the fluorescence of the 'free' fluosphere. Furthermore, it was expected that significant fluorescence would be emitted at high angles through the DMD stack, become trapped in the substrate by TIR, and thus be visible as light transmitted from the edges of the glass substrate. Camera images (Figure 5.14 and Figure 5.15) verified that fluorescence was emitted from both the surface and the edges of the sample. Bright green fluorescence could be excited using

either a visible (473 nm wavelength) or UV (374 nm wavelength) laser. This fluorescence was visible as a bright spot emanating from the sample surface, and as a relatively less bright band of light emanating from the edges of the glass substrate.

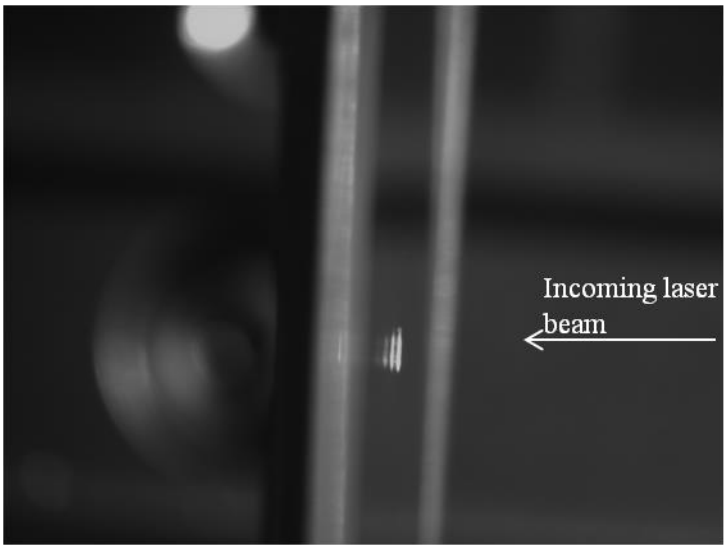

Figure 5.14 A monochromatic camera picture taken from the top of the sample with the excitation of the fluospheres using a 374 nm laser. The bright series of short lines in the center of the image is attributed to emission of fluorescence from the surface of the sample. The multiple lines are believed to be due to the light experiencing multiple reflections between the substrate and DMD multilayer interfaces. Note that the laser was incident from the right side of the image. The edges of the glass substrate on the right are clearly illuminated by fluorescent light, both at the top and bottom edges. The glass substrate on the left appears dark, but this is due to the angle of the camera relative to the sample edges. Note that the manual assembly process results in imperfect alignment of the edges of the two substrates. Also note that the partial transparency of the sample at near-grazing viewing directions is apparent; the black line running across the upper portion of the image is in the background.

The image shown in Figure 5.15 was captured under excitation by the blue laser, and without a laser blocking filter in front of the camera. It illustrates a couple interesting facts:

i. The laser is incident from the left, and scattered laser light causes the left substrate to be illuminated brightly in blue. However, the light emanating from the right side of the sample (obliquely facing the camera) is green, arising from

the fluorescence of the embedded fluospheres. As above, green fluorescence is clearly emanating from both the surface and the edges of the sample.

ii. The absence of blue light on the right-hand side of the sample is due to the strong suppression of light by the DMD multilayer at this wavelength (see Figure 5.4). Related to this, it is expected that only a small portion of the incident laser light actually reaches the fluospheres embedded within the DMD stack. Nevertheless, it is sufficient to excite significant green fluorescence.

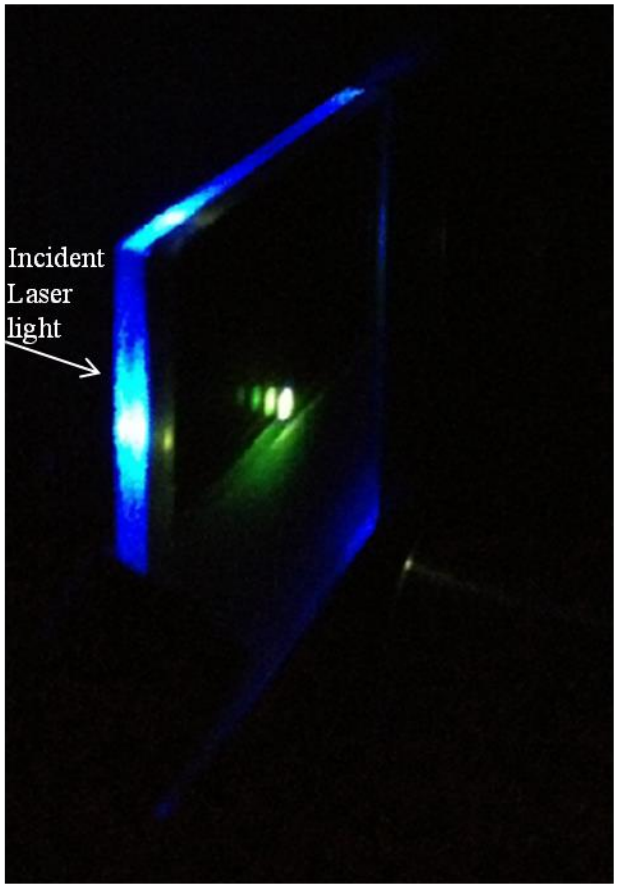

Figure 5.15 A camera picture of the sample with the excitation of the fluospheres using a 473 nm (blue) laser. The laser is incident from the left, and the image is captured from an oblique viewpoint to the right of the sample. Scattered blue laser light illuminates the edges of the glass substrate on the incident side.

Subsequently, the spectral emission properties of the sample were studied. To facilitate this study, a reference sample was created by depositing a small quantity of the

yellow-green fluospheres onto a plain glass slide. After allowing the solvent to evaporate, the fluospheres were excited using the blue laser and their fluorescence was collected by the spectrometer mentioned above. A laser blocking filter was used to suppress scattered excitation light prior to the spectrometer. The captured reference spectrum is shown by the dashed line in Figure 5.16, and is in good agreement with the spectrum provided by the manufacturer (Figure 5.8). The experimental data exhibits a slight red-shift of the peak emission wavelength, which is likely due to the high concentration of fluorescent dye molecules [20], since the sample is essentially a 'clump' of fluospheres on a bare substrate.

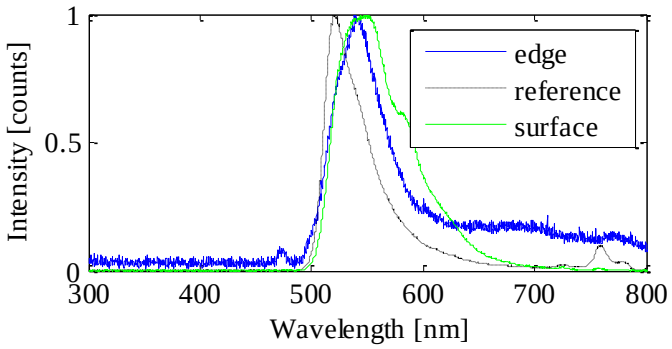

Figure 5.16 Spectral scans of the emitted yellow-green fluorescence perpendicular to the sample surface (green solid line) and sample edge (blue solid line) are shown, normalized to their own peaks. Note that the black dashed line represents the fluospheres on a plain substrate as a reference.

Fluorescence spectra were subsequently collected from both the surface and the edges of the 'sandwich' sample. Figure 5.16 shows a comparison of the spectral shapes for each case, on a normalized scale. The normalized scale was used because it is extremely challenging to account for differences in excitation power, etc., between the reference and DMD samples. The data corroborated the predictions from the previous section, as follows:

i. The fluorescence spectrum of the DMD sample is clearly red-shifted relative to that of the reference sample. Furthermore, the red-shift is larger for the fluorescence collected from the surface of the sample.

ii. The surface emission from the DMD sample exhibited a distinct secondary peak at ~590 nm wavelength. This is possibly due to the enhancement of fluorescence at the edge of the stop band (see Figure 5.4).

Note that the spectrum detected from the edge is relatively noisy. This is because the intensity of collected fluorescence is relatively weak in this case, compared to the detection from the surface. The edge fluorescence is emitted in all directions, but the pick-up fiber of the spectrometer is only collecting a small fraction of this emission. Note also that there is a small peak at ~ 475 nm in the edge spectrum, which is possibly due to the residual laser light transmitted through the filter and detected by the spectrometer.

To further illustrate the modification of the spontaneous emission by the DMD structure, Figure 5.17 shows the surface-emitted (normalized) spectrum of the DMD sample divided by the normalized reference spectrum. This type of plot draws out the spectral enhancement or suppression of emission caused by embedding the fluospheres inside the DMD multilayer. It is clear that the emission is enhanced at the stop band edge (i.e. ~590 nm), which is in agreement with the band edge enhancement described for similar structures in the literature [23, 14].

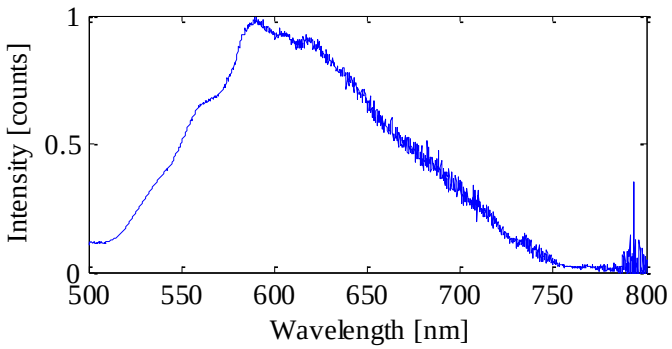

Figure 5.17 Normalized 'enhancement' spectrum obtained by dividing the surface emission spectrum of the DMD sample by the reference spectrum. The peak 'enhancement' of the spectrum at ~590 nm is consistent with the location of the edge of the stop band for the DMD multilayer.

5.4.2.2 Blue fluospheres

The spectrum detection for the sample containing the blue fluospheres was more challenging. This was due to the fact that these fluospheres require the UV laser for excitation (see Figure 5.8), and the available laser-blocking filter (with a cut-off near 395 nm wavelength to allow the blue fluorescence to pass) could not block the laser light completely. In fact, spectra collected by the Ocean Optics spectrometer were typically dominated by the UV laser line in these experiments. As shown in Figure 5.18 (see the green blue solid line), when attempting to collect fluorescence from the surface, the residual power from the UV laser was high enough to saturate the Ocean Optics detector over the range from ~ 350 nm to ~ 440nm. This is partly due to the poor spectral purity of the available UV laser, which emits significant power outside its main lasing line at ~376 nm. Future work would be benefit from a better excitation source and filters with better rejection.

Nevertheless, a preliminary study of the edge and surface emission was conducted, to parallel the results for the yellow-green fluospheres. As above, a reference spectrum was collected from a clump of blue fluospheres on a plain microscope slide. The reference

spectrum is plotted as the black dotted line in Figure 5.18, and is in good agreement with the data supplied by the manufacturer (Figure 5.8). The anomalous peaks in the reference spectrum (at ~480 and ~550 nm) were due to the fluorescent lights in the laboratory, as confirmed by separate measurements (not shown).

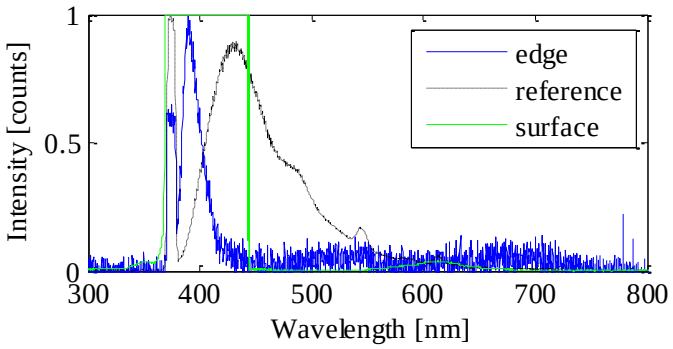

Figure 5.18 Spectral scans of the emitted fluorescence collected from the surface (green solid line) and edge (blue solid line) of the samples, normalized with respect to their own peaks. Note that the black dashed line is a reference scan for the fluospheres deposited on a plain substrate.

Due to the saturation of the detector mentioned above, no further analysis of the surface emission was conducted. However, it is interesting to note that there is a slight increase in the surface emission near 600 nm wavelength, as expected from the location of the normal-incidence transparency band. For the edge emission, the data seems to suggest enhanced emission just below 400 nm wavelength, which would be consistent with the location of the short-wavelength edge of the stop band (see Figure 5.4). This is made clearer by the 'enhancement plot' shown in Figure 5.19, which is simply the edge emission data divided by the reference spectrum and normalized to a peak value of 1. This plot suggests detected strong suppression of the emission within the stop band (between ~400 and ~600 nm wavelength). Moreover, the emission is apparently enhanced at the band edges. However, the apparent enhancement at the short-wavelength band-edge might be partly attributable to the laser spectral noise mentioned above, and

the enhancement at the long-wavelength-edge is difficult to assess due to the low emission of the blue fluospheres in this range (which makes the data relatively noisy).

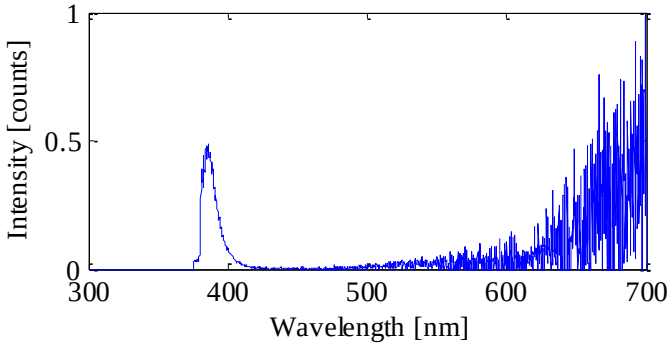

Figure 5.19 The normalized 'enhancement' spectrum of the spontaneous emission emitted from the edge of the blue fluosphere sample. The plot was obtained by dividing the edge emission data by the data for the reference spectrum.

This preliminary data is promising and in reasonable agreement with predictions, suggesting there is strong potential for interesting future work in this area.

5.5 Conclusion

In this chapter, DMD samples were designed specifically for TE-polarized tunneling mediated by Fabry-Perot resonances. We verified that it is possible to design structures that have a nearly perfect admittance match at high incidence angles, using practical material such as TiO_2 and Ag. Experimental results were compared to the simulated results, showing a good agreement in terms of shapes and trends. Some reduction in transmittance for the experimental results is possibly due to the oxidation of the Ag layers, as discussed previously in Chapter 4.

A preliminary study of the modification of the spontaneous emission was also given based on the 3-period sample assembled with various fluorescent beads in the center. It was found that the emitted fluorescence was modified by the transparent bands of the samples. Both enhancement and suppression of the emission were obtained by using

fluospheres with different emission spectra. However, further research is required to achieve a more accurate understanding of the modification.

References

[1] E. Yablonovitch, "Inhibited Spontaneous Emission in Solid-State Physics and Electronics," *Phys. Rev. Lett.,* vol. 58, p. 2059, (1987).

[2] S. John, "Strong localization of photons in certain disordered dielectric superlattices," *Phys. Rev. Lett.*, vol. 58, p. 2486, (1987).

[3] E. Yablonovitch, "Photonic band-gap structures," *J. Opt. Soc. Am. B,* vol. 10, no. 2, p. 283, (1993).

[4] S. Hayashi, H. Kurokawa and H. Oga, "Observation of resonant photon tunneling in photonic double barrier structures," *Optical Review,* vol. 6, pp. 204-210, (1999).

[5] T. W. Allen and R. G. DeCorby, "Conditions for admittance-matched tunneling through symmetric metal-dielectric stacks," *Optics Express,* vol. 20, no. 55, pp. A578-A588, (2012).

[6] T. W. Allen and R. G. DeCorby, "Assessing the maximum transmittance of periodic metal-dielectric multilayers," *JOSA B,* vol. 28, no. 10, pp. 2529-2536, (2011).

[7] S. Y. Kim, "Simultaneous determination of refractive index, extinction coefficient, and void distribution of titanium dioxide thin film by optical methods," *Appl. Opt.,* vol. 35, pp. 6703-6707, (1996).

[8] A. D. Rakic, A. B. Djurisic, J. M. Elazar and M. L. Majewski, "Optical Properties of Metallic Films for Vertical-Cavity Optoelectronic Devices," *Applied Optics,* vol. 37,

no. 22, pp. 5271-5283, (1998).

[9] B. H. Liao, C. C. Kuo, P. J. Chen and C. C. Lee, "Fluorine-doped tin oxide films grown by pulsed direct current magnetron sputtering with an Sn target," *Applied Optics,* vol. 50, no. 9, pp. C106-C110, (2011).

[10] T. D. Happ, I. I. Tartakovskii, V. D. Kulakovskii, J. P. Reithmaier, K. Kamp and A. Forchel, "Enhanced light emission of InxGa1−xAs quantum dots in a two-dimensional photonic-crystal defect microcavity," *Phys. Rev. B,* vol. 66, p. 041303, (2002).

[11] T. Yoshie, A. Scherer, J. Hendrickson, G. Khitrova, H. M. Gibbs, G. Rupper, C. Ell, O. B. Shchekin and D. G. Depps, "Vacuum Rabi splitting with a single quantum dot in a photonic crystal nanocavity," *Nature,* vol. 432, pp. 200-203, (2004).

[12] A. Badolato, K. Hennessy, M. Atature, J. Dreiser, E. Hu, P. M. Petroff and A. Imamoglu, "Deterministic coupling of single quantum dots to single nanocavity modes," *Science,* vol. 308, p. 1158–1161, (2005).

[13] T. Kuroda, N. Ikeda, T. Mano, Y. Sugimoto, T. Ochiai, K. Kuroda, S. Ohkouchi, N. Koguchi, K. Sakoda and K. Asakawa, "Acceleration and suppression of photoemission of GaAs quantum dots embedded in photonic crystal microcavities," *Appl. Phys. Lett.,* vol. 93, p. 111103, (2008).

[14] M. D. Tocci, M. Scalora, M. J. Bolemer, J. P. Dowling and C. M. Bowden, "Measurement of spontaneous-emission enhancement near the one-dimensional photonic band edge of semiconductor heterostructures," *Phy.Rev. A,* vol. 53, no. 4, pp. 2799-2803, (1996).

[15] C. Sibilia, M. Scalora, M. Centini, M. Bertolotti, M. J. Bloemer and C. M. Bowden,

"Electromagnetic properties of periodic and quasi-periodic one-dimensional, metallo-dielectric photonic band gap structures," *J. Opt. A,* vol. 1, p. 490–494, (1999).

[16] G. Winter and W. L. Barnes, "Emission of light through thin silver films via near-field coupling to surface plasmon polaritons," *Appl. Phys. Lett.,* vol. 88, p. 051109, (2006).

[17] H. Rigneault, C. Amra, C. Begon, M. Cathelinaud and C. Picard, "Light emission from sources located within metallodielectric planar microcavities," *Applied Optics,* vol. 38, no. 16, pp. 3602-3609, (1999).

[18] P. A. Hobson, S. Wedge, J. A. Wasey, I. Sage and W. L. Barnes, "Surface Plasmon Mediated Emission from Organic Light-Emitting Diodes," *Adv. Mater.,* vol. 14, no. 19, pp. 1393-1396, (2002).

[19] W. D. Newman, C. L. Cortes and Z. Jacob, "Enhanced and directional single-photon emission in hyperbolic metamaterials," *J. Opt. Soc. Am. B,* vol. 30, no. 4, pp. 766-775, (2013).

[20] J. R. Lakowicz, Principles of Fluorescence Spectroscopy, 3 ed., Springer, 2006.

[21] D. Delbeke, R. Bockstaele, P. Bienstman, R. Baets and H. Benisty, "High-efficiency semiconductor resonant-cavity light-emitting diodes: a review," *IEEE Journal on Selected Topics in Quantum Electronics,* vol. 8, no. 2, pp. 189 - 206, (2002).

[22] H. Benisty, R. Stanley and M. Mayer, "Method of source terms for dipole emission modification in modes of arbitrary planar structures," *JOSA A,* vol. 15, no. 5, pp. 1192-1201, (1998).

[23] K. Kuroda, T. Sawada, T. Kuroda, K. Watanabe and K. Sakoda, "Doubly enhanced

spontaneous emission due to increased photon density of states at photonic band edge frequencies," *Optics Express*, vol. 17, no. 15, pp. 13168-13177, (2009).

Chapter 6 Conclusion

6.1 Summary and results

This thesis concludes an experimental study of metal-dielectric (MD) thin-film multilayers. Admittance-matching concepts and potential transmittance (PT) theory were used to design multilayers with transparency optimized for either propagating or evanescent waves. For evanescent waves, SiO_2-Ag-SiO_2 multilayers were studied and the overall agreement between the experimental and theoretical results was very good. For propagating waves, good agreement between experimental and theoretical results was obtained using TiO_2-Ag-TiO_2 multilayers. Preliminary studies on modification of spontaneous emission by the 3-period TiO_2-Ag-TiO_2 multilayers were also described, and the results suggest that this is a promising avenue for future research. Finally, alternative techniques for improving the transparency (i.e. the admittance match) of SiO_2-Ag-SiO_2 multilayers at normal incidence were studied.

6.1.1 Optimized surface-plasmon-mediated tunneling in MD multilayers

Surface-plasmon-mediated tunneling was experimentally studied using a symmetric DMD unit cell consisting of one 40 nm Ag layer sandwiched between two 180 nm SiO_2 layers. Key results obtained from the experiments on the surface-plasmon-mediated tunneling studied in Chapter 3 include:

- The work provided experimental verification that PT theory and admittance-matching concepts can be used to optimize the tunneling efficiency of evanescent waves (mediated by surface plasmon resonances) through DMD stacks.

- Samples containing ~120 nm total thickness of silver, equivalent to ~10 skin depths, were shown to exhibit peak transmittance ~0.7 at the 632 nm design wavelength.

6.1.2 Transparency and stability of Ag-based MD multilayers

MD bandpass filters are historically of interest because they provide excellent out of band rejection over a large spectral range. It is known that higher-index dielectric layers are able to provide an improved admittance match (thus typically higher transparency in the pass-band), but at the expense of certain practical challenges. In Chapter 4, we considered both the high-index (i.e. TiO_2) and low-index (i.e. SiO_2) films, and significant results include:

- MD stacks containing low-index (i.e. SiO_2) films were found to be more stable and predictable compared to MD stacks containing high-index (i.e. TiO_2) films. This was attributed to oxidation of the metallic (i.e. Ag) layers in the latter case.
- Proper termination of the low-index (i.e. SiO_2)-based periodic MD multilayers can reduce the admittance mismatch and thereby enhance the optical properties. A single film, high-index (i.e. TiO_2) matching layer was shown to significantly enhance the peak transmittance, spectral bandwidth, and angular bandwidth of the SiO_2-based filter.
- The classical IT design applied to periodic multilayers was shown to be potentially useful for narrowband applications requiring optimal transparency, since the transparency at a given wavelength is limited only by the maximum potential transmittance of the structure.

6.1.3 Tunneling of TE-polarized light through DMD stacks

In Chapter 5, we focused on the tunneling by TE-polarized light, and designed a symmetric TiO_2-Ag-TiO_2 unit cell to be admittance matched at 500 nm wavelength for an incident angle of ~80 degrees inside a glass ambient medium. Furthermore, we studied the modification of spontaneous emission using two 3-period DMD multilayers bonded with a fluosphere (fluorescent beads) 'spacer' layer in the center. Although this study was of a preliminary nature, it produced some promising results including:

- Further evidence of the oxidation of the Ag layers in the DMD multilayers that employ TiO_2 as the dielectric.
- Evidence for modification of spontaneous emission for laser dyes embedded in DMD structures. The emitted fluorescence spectrum showed clear band-edge enhancement effects, and suppression of the fluorescence emission at wavelengths inside the stop band of the DMD stack.

6.2 Future work

As discussed in Chapter 5, DMD stacks were manually assembled with various fluorescent beads. A complete treatment of the detailed theoretical aspects of the bound structure was not given. Nevertheless, the experimental results are promising in light of the basic theoretical predictions that were considered and should offer significant scope for future work. Some suggested steps that can be taken for future study are summarized below:

i. It would be useful to verify the actual physical structure of the bonded samples. For example, it is likely that an air gap remains between the two multilayers. Careful optical experimentation might be able to ascertain these details. This is important since the local physical environment of the embedded fluospheres can greatly affect their emission spectrum.

ii. Accurate modeling prediction of the ‘sandwich’ samples will require a careful consideration of the polarization effects and other details. For example, the polarization of the excitation laser is expected to determine the dominant in-plane polarization of the emitting dye molecules. Furthermore, the polarization of the emitting dye molecules will have a direct impact on the amount of TE and TM polarized modes that are excited along a given direction inside the DMD multilayer. These details were mostly neglected in the present study, but must be considered in order to understand the enhancement or suppression of spontaneous emission into different modes.

A more general topic for future work would be a study of techniques for reducing oxidation in Ag-TiO_2 based multilayers. This is an important goal because TiO_2 is widely used as a high-index film in MD multilayers. Possible solutions include introducing a wetting layer (i.e. Ti or SiO_2) in between the Ag and TiO2 layers.

Appendix A: Deposition Details

As mentioned in previous chapters, SiO_2, TiO_2, and Ag were deposited using a six-pocket electron beam evaporator. Source materials were contained in liner, which was put into the hearth inside the evaporator for the electron beam to melt the source. Since the evaporator has six pockets (i.e. six hearths), all source materials can be loaded at once so that samples can be deposited without breaking the vacuum. To ensure an accurate monitor of the film thickness, two thickness monitors (i.e. STM-100/MF and STC-2000A) were used and the thickness was determined to be the average value of the readings from the two monitors. Table A.1 lists the material profiles and parameters for the thickness monitors that must be set up correspondingly. Since the thickness monitors are not perfectly aligned with the substrate holder (i.e. they are not perfectly sitting on the same surface level), a calibration step must be done to offset the difference in thickness. This calibration step was performed by first depositing a sample with a specific thickness shown in the thickness monitors (i.e. 20 nm), and then measuring the actual thickness deposited on the sample by using some measurement equipment (i.e. Alpha Step IQ). A calibration number can thus be obtained by dividing the targeted-thickness (i.e. readings from thickness monitors) and the as-deposited thickness (i.e. the actual thickness measured). This calibration number can be improved by taking multiple calibration steps with different thicknesses, but normally one calibration step is accurate enough.

Table A.1 Material profiles and parameters for the thickness monitors

	Profile number		Material parameters	
	STM 100	STC 2000	Density	Z-factor
TiO_2	1	23	4.26	0.4
SiO_2	3	3	2.2	1.07
Ag	2	4	10.5	0.529

For SiO_2 deposition, the deposition rate was found to be ~3 Åm/s to ensure the stoichiometry and optical performance. Since this rate is relatively rapid, the electron beam profile must be set to "sweep" in order not to quickly drill a hole through the source and burn the liner. For TiO_2 deposition, external oxygen supply was added to ensure stoichiometry. The amount of oxygen should be added until the chamber pressure was $5x10^{-5}$ Torr. Note that during deposition the chamber pressure must be maintained at $5x10^{-5}$ Torr by frequently adjusting the input of the oxygen. In addition, the deposition rate should be 0.5~0.6 Åm/s for TiO_2. For Ag deposition, a small graphite plate was inserted beneath the liner to reduce the thermal conduction between the liner and the hearth (i.e. reduce the cooling of the Ag source), otherwise the system may not be able to supply a sufficiently high power to melt the Ag source in order to reach a proper deposition rate. With the placement of the plate, current must be brought up very slowly (i.e. make take ~ 5 minutes to heat up the source) to avoid sudden jump of the deposition rate. Similarly, when a deposition was finished, the current should be slowly brought down and user should wait for approximately 5 minutes to let the Ag source cool down before switching to another source. The proper deposition rate for Ag should be ~ 1 Åm/s. Table A.2 shows the calibration numbers found for our sample preparations under the similar deposition parameters recorded in Table A.3 and Table A.4. Note that this calibration number may vary for different depositing conditions (i.e. heated substrate, different deposition rate, etc).

Table A.2 Calibration table for deposition source materials

	Targeted thickness [nm]	Calibrated/deposited thickness [kÅm]	Calibration number
TiO_2	50	0.341	1.4663
SiO_2	180	1.519	1.185
Ag	40	0.34	1.1765

Table A.3 and Table A.4 show two examples for the recorded deposition. Note that in these two tables, there were no graphite plates used for Ag source, thereby the current used to generate electron beam were very high. Also note that the current required to reach a specific deposition rate may vary each time during deposition depending on the voltage set up for the evaporator.

Table A.3 Deposition table an 180nm-40nm-180nm SiO_2-Ag-SiO_2 unit cell

	Pressure	Time	Thickness [k Åm]			Dep. rate	Current
	[Torr]	[min]	Left (STM)	Right (STC)	Average	[Åm/s]	[A]
SiO_2	$2.5x10^{-6}$	8:13	1.513	1.52	1.5165	2.8~3	0.04
Ag	$4.5x10^{-6}$	5:06	0.356	0.324	0.34	1.2	0.26
SiO_2	$2x10^{-6}$	8:13	1.619	1.441	1.53	3.2	0.04

Table A.4 Deposition table a 50nm-30nm-50nm TiO_2-Ag-TiO_2 unit cell

	Pressure	Time	Thickness [k Åm]			Dep. rate	Current
	[Torr]	[min]	Left (STM)	Right (STC)	Average	[Åm/s]	[A]
TiO_2	$5x10^{-5}$	12:58	0.453	0.438	0.446	0.6	0.13
Ag	$4x10^{-6}$	3:57	0.259	0.253	0.256	1.1	0.23
TiO_2	$5x10^{-5}$	9:24	0.352	0.328	0.34	0.6	0.13

Appendix B: MatLab code

In this section five files are included. The first two are the admittance matching calculation codes for TE and TM polarized incident light. These two files use an iteration technique to search for the best value of the admittance-matched case. Note that the precision of the final solutions can be manipulated by adding while loops or changing the condition for the last while loop.

The rest three files are the simulation codes for symmetric dielectric-metal-dielectric (DMD) stacks. I have parameterized all the input values (i.e. input wavelength, incident angles, dielectric index, metal index, substrate index, and ambient medium index) by having a function file that does all the calculation, a '.txt' format structure file that contains the structure of the DMD stack, and an execution file that calls the previous two files and plots the figures.

Admittance matching for TE

```
% This file calculates the incidence angles that enable admittance matching
% correspond to a given range of metal thicknesses, given n1 and n2 values.
% This file is only valid for TE-POLARIZED wave
clear all
lambda0=500e-9;   %free space wavelength

%define metal thickness range
Ag_left_bound=25e-9;
Ag_right_bound=45e-9;
metal_thickness=Ag_left_bound:0.1e-9:Ag_right_bound;

TiO2OpCon; %m-file that calculates the optical constants of TiO2
AgOpCon;
NAg=nAgv-1i*kAgv; %metal (Ag) refractive index

nFS=sqrt(0.6961663.*(lambda0*1e6).^2./((lambda0*1e6).^2-
0.0684043^2)+0.4079426.*(lambda0*1e6).^2./((lambda0*1e6).^2-
0.1162414^2)+0.8974794.*(lambda0*1e6).^2./((lambda0*1e6).^2-9.896161^2)+1);
%n2=nSF11;      %air/prism ambient
%n1=nFS;    %dielectric index
```

```
n2=nFS;
%n2=1.5;      %air/prism ambient
%n1=2.35;    %dielectric index
n1=ntio2;

ang=zeros(1,length(metal_thickness));
dielectric_thickness=zeros(1,length(metal_thickness));
for i=1:1:length(metal_thickness)
   dm=metal_thickness(i);      %setup current metal thickness
   theta=0*pi/180;            %setup intial incidence angle

   fun=5;            %intialize function value for iteration
   Xopa=1i;          %initialize Xop value for iteration
   % Algorithm to find incidence angle given n1, n2, dm that enables
   % admittance matching
   %=========================================================
   % Step 1: make sure Xop calculated from admittance matching equation is
   % always a real number so it can be equate to the Xop calculated from
   % the general Xop equation
   while abs(imag(Xopa))>1e-10
      theta1=asin(n2*sin(theta)/n1);      %incidence angle in dielectric layer
      thetam=asin(n1*sin(theta1)/NAg);    %incidence angle in metal layer
      NM=NAg*cos(thetam);   %for TE
      NR=real(NM);
      NI=-imag(NM);
      eta2=n2*cos(theta);   %for TE
      eta1=n1*cos(theta1);  %for TE
      % Find Xop form general equation
      alpha=real((2*pi/lambda0)*NAg*dm*cos(thetam));
      beta=-imag((2*pi/lambda0)*NAg*dm*cos(thetam));

term1=(NR^2+NI^2)*(NR*sinh(beta)*cosh(beta)+NI*sin(alpha)*cos(alpha))/(NR*sinh(
beta)*cosh(beta)-NI*sin(alpha)*cos(alpha));

term2=(NR^2*NI^2)*((sin(alpha)^2*cosh(beta)^2+cos(alpha)^2*sinh(beta)^2)/(NR*sinh
(beta)*cosh(beta)-NI*sin(alpha)*cos(alpha)))^2;
      Xop=(term1-term2)^0.5;

Zop=(NR*NI)*(sin(alpha)^2*cosh(beta)^2+cos(alpha)^2*sinh(beta)^2)/(NR*sinh(beta)*
cosh(beta)-NI*sin(alpha)*cos(alpha));
      % Find Xop from impedence matchinig equation
      Xopa=2*eta2/(-cos(asin(2*Zop/(Xop*(eta1/eta2-eta2/eta1))))*(1-
eta2^2/eta1^2)+(1+eta2^2/eta1^2));
      theta=theta+1*pi/180;
   end
   theta=theta-1*pi/180;
   %Step 2: find an approximate value of angle that the two calculated Xop
   %are close to each other
   while abs(fun)>1
```

```
        theta1=asin(n2*sin(theta)/n1);
        thetam=asin(n1*sin(theta1)/NAg);
        NM=NAg*cos(thetam);
        NR=real(NM);
        NI=-imag(NM);
        eta2=n2*cos(theta);
        eta1=n1*cos(theta1);
        alpha=real((2*pi/lambda0)*NAg*dm*cos(thetam));
        beta=-imag((2*pi/lambda0)*NAg*dm*cos(thetam));

term1=(NR^2+NI^2)*(NR*sinh(beta)*cosh(beta)+NI*sin(alpha)*cos(alpha))/(NR*sinh(
beta)*cosh(beta)-NI*sin(alpha)*cos(alpha));

term2=(NR^2*NI^2)*((sin(alpha)^2*cosh(beta)^2+cos(alpha)^2*sinh(beta)^2)/(NR*sinh
(beta)*cosh(beta)-NI*sin(alpha)*cos(alpha)))^2;
        Xop=(term1-term2)^0.5;

Zop=(NR*NI)*(sin(alpha)^2*cosh(beta)^2+cos(alpha)^2*sinh(beta)^2)/(NR*sinh(beta)*
cosh(beta)-NI*sin(alpha)*cos(alpha));
        Xopa=2*eta2/(-cos(asin(2*Zop/(Xop*(eta1/eta2-eta2/eta1))))*(1-
eta2^2/eta1^2)+(1+eta2^2/eta1^2));
        fun=Xopa-Xop;
        theta=theta+0.01*pi/180;
    end
    theta=theta-0.01*pi/180;
    %Step 3: find the exact incidence angle that will enable the admittance
    %matching (i.e. two calculated Xop's can be approximated as same)
    while abs(fun)>0.0001
        theta1=asin(n2*sin(theta)/n1);
        thetam=asin(n1*sin(theta1)/NAg);
        NM=NAg*cos(thetam);
        NR=real(NM);
        NI=-imag(NM);
        eta2=n2*cos(theta);
        eta1=n1*cos(theta1);
        alpha=real((2*pi/lambda0)*NAg*dm*cos(thetam));
        beta=-imag((2*pi/lambda0)*NAg*dm*cos(thetam));

term1=(NR^2+NI^2)*(NR*sinh(beta)*cosh(beta)+NI*sin(alpha)*cos(alpha))/(NR*sinh(
beta)*cosh(beta)-NI*sin(alpha)*cos(alpha));

term2=(NR^2*NI^2)*((sin(alpha)^2*cosh(beta)^2+cos(alpha)^2*sinh(beta)^2)/(NR*sinh
(beta)*cosh(beta)-NI*sin(alpha)*cos(alpha)))^2;
        Xop=(term1-term2)^0.5;

Zop=(NR*NI)*(sin(alpha)^2*cosh(beta)^2+cos(alpha)^2*sinh(beta)^2)/(NR*sinh(beta)*
cosh(beta)-NI*sin(alpha)*cos(alpha));
        Xopa=2*eta2/(-cos(asin(2*Zop/(Xop*(eta1/eta2-eta2/eta1))))*(1-
eta2^2/eta1^2)+(1+eta2^2/eta1^2));
```

```
        fun=Xopa-Xop;
        theta=theta+0.0001*pi/180;
        % check if theta is greater than 90 deg
        if theta>91*pi/180
            theta=pi;   %indicating there is no solution for such thickness
            break
        end
    end
    ang(i)=theta*180/pi;
    % Calculate the thickness that enables admittance matching. Note this
    % thickness is different from the SP case because it resulted in a
    % different quadrent
    dielectric_thickness(i)=abs(lambda0/(4*pi*n1*cos(theta1))*(pi-
asin(2*Zop/(Xop*(eta1/eta2-eta2/eta1)))))*1e9;
end
subplot(2,1,1)
hold on
plot(metal_thickness*1e9, ang)
xlabel('Ag thickness [nm]')
ylabel('Admittance macthing angle [deg]')
title(['Incident light at ', num2str(lambda0*1e9), ' nm wavelength'])
hold off
subplot(2,1,2)
hold on
plot(metal_thickness*1e9, dielectric_thickness)
xlabel('Ag layer thickness [nm]')
ylabel('dielectric thickness for matching [nm]')
hold off
```

Admittance matching for TM

```
% This file calculates the incidence angles that enable admittance matching
% correspond to a given range of metal thicknesses, given n1 and n2 values.
% This file is only valid for TE-POLARIZED wave
clear all
lambda0=632.8e-9;   %free space wavelength

%define metal thickness range
Ag_left_bound=30e-9;
Ag_right_bound=50e-9;
metal_thickness=Ag_left_bound:0.1e-9:Ag_right_bound;

AgOpCon;
%AgOpConPalik;
NAg=nAgv-1i*kAgv; %metal (Ag) refractive index
```

```
nSF11=sqrt(1.73759695.*(lambda0*1e6).^2./((lambda0*1e6).^2-
0.013188707)+0.313747346.*(lambda0*1e6).^2./((lambda0*1e6).^2-
0.0623068142)+1.89878101.*(lambda0*1e6).^2./((lambda0*1e6).^2-155.23629)+1);
nFS=sqrt(0.6961663.*(lambda0*1e6).^2./((lambda0*1e6).^2-
0.0684043^2)+0.4079426.*(lambda0*1e6).^2./((lambda0*1e6).^2-
0.1162414^2)+0.8974794.*(lambda0*1e6).^2./((lambda0*1e6).^2-9.896161^2)+1);
%n2=1.515;      %air/prism ambient
%n1=1.38;    %dielectric index
n2=nSF11;      %air/prism ambient
n1=nFS;    %dielectric index
%n2=1.778;
%n1=1.487;

ang=zeros(2,length(metal_thickness));
dielectric_thickness=zeros(2,length(metal_thickness));
for i=1:1:length(metal_thickness)
   dm=metal_thickness(i);      %setup current metal thickness
   %setup intial incidence angle to the truncated closest integer crytical angle
   theta=floor(asin(n1/n2))*pi/180;
   %theta=65*pi/180;

   fun=5;           %intialize function value for iteration
   Xopa=1i;          %initialize Xop value for iteration
   % Algorithm to find incidence angle given n1, n2, dm that enables
   % admittance matching
   %============================================================
   % Step 1: make sure Xop calculated from admittance matching equation is
   % always a real number so it can be equate to the Xop calculated from
   % the general Xop equation
   while abs(imag(Xopa))>1e-10
      theta1=asin(n2*sin(theta)/n1);      %incidence angle in dielectric layer
      thetam=asin(n1*sin(theta1)/NAg);    %incidence angle in metal layer
      NM=NAg/cos(thetam);   %for TM
      NR=real(NM);
      NI=-imag(NM);
      eta2=n2/cos(theta);   %for TM
      eta1=n1/cos(theta1);  %for TM
      % Find Xop form general equation
      alpha=real((2*pi/lambda0)*NAg*dm*cos(thetam));
      beta=-imag((2*pi/lambda0)*NAg*dm*cos(thetam));

term1=(NR^2+NI^2)*(NR*sinh(beta)*cosh(beta)+NI*sin(alpha)*cos(alpha))/(NR*sinh(
beta)*cosh(beta)-NI*sin(alpha)*cos(alpha));

term2=(NR^2*NI^2)*((sin(alpha)^2*cosh(beta)^2+cos(alpha)^2*sinh(beta)^2)/(NR*sinh
(beta)*cosh(beta)-NI*sin(alpha)*cos(alpha)))^2;
      Xop=(term1-term2)^0.5;
```

```
Zop=(NR*NI)*(sin(alpha)^2*cosh(beta)^2+cos(alpha)^2*sinh(beta)^2)/(NR*sinh(beta)*
cosh(beta)-NI*sin(alpha)*cos(alpha));
      % Find Xop from impedence matchinig equation
      Xopa=2*eta2/(cos(asin(2*Zop/(Xop*(eta1/eta2-eta2/eta1))))*(1-
eta2^2/eta1^2)+(1+eta2^2/eta1^2));
      theta=theta+1*pi/180;
   end
   theta=theta-1*pi/180;
   %Step 2: find an approximate value of angle that the two calculated Xop
   %are close to each other
   while abs(fun)>1
      theta1=asin(n2*sin(theta)/n1);
      thetam=asin(n1*sin(theta1)/NAg);
      NM=NAg/cos(thetam);
      NR=real(NM);
      NI=-imag(NM);
      eta2=n2/cos(theta);
      eta1=n1/cos(theta1);
      alpha=real((2*pi/lambda0)*NAg*dm*cos(thetam));
      beta=-imag((2*pi/lambda0)*NAg*dm*cos(thetam));

term1=(NR^2+NI^2)*(NR*sinh(beta)*cosh(beta)+NI*sin(alpha)*cos(alpha))/(NR*sinh(
beta)*cosh(beta)-NI*sin(alpha)*cos(alpha));

term2=(NR^2*NI^2)*((sin(alpha)^2*cosh(beta)^2+cos(alpha)^2*sinh(beta)^2)/(NR*sinh
(beta)*cosh(beta)-NI*sin(alpha)*cos(alpha)))^2;
      Xop=(term1-term2)^0.5;

Zop=(NR*NI)*(sin(alpha)^2*cosh(beta)^2+cos(alpha)^2*sinh(beta)^2)/(NR*sinh(beta)*
cosh(beta)-NI*sin(alpha)*cos(alpha));
      Xopa=2*eta2/(cos(asin(2*Zop/(Xop*(eta1/eta2-eta2/eta1))))*(1-
eta2^2/eta1^2)+(1+eta2^2/eta1^2));
      fun=Xopa-Xop;
      theta=theta+0.01*pi/180;
   end
   theta=theta-0.01*pi/180;
   %Step 3: find the exact incidence angle that will enable the admittance
   %matching (i.e. two calculated Xop's can be approximated as same)
   while abs(fun)>0.0001
      theta1=asin(n2*sin(theta)/n1);
      thetam=asin(n1*sin(theta1)/NAg);
      NM=NAg/cos(thetam);
      NR=real(NM);
      NI=-imag(NM);
      eta2=n2/cos(theta);
      eta1=n1/cos(theta1);
      alpha=real((2*pi/lambda0)*NAg*dm*cos(thetam));
      beta=-imag((2*pi/lambda0)*NAg*dm*cos(thetam));
```

```
term1=(NR^2+NI^2)*(NR*sinh(beta)*cosh(beta)+NI*sin(alpha)*cos(alpha))/(NR*sinh(
beta)*cosh(beta)-NI*sin(alpha)*cos(alpha));

term2=(NR^2*NI^2)*((sin(alpha)^2*cosh(beta)^2+cos(alpha)^2*sinh(beta)^2)/(NR*sinh
(beta)*cosh(beta)-NI*sin(alpha)*cos(alpha)))^2;
      Xop=(term1-term2)^0.5;

Zop=(NR*NI)*(sin(alpha)^2*cosh(beta)^2+cos(alpha)^2*sinh(beta)^2)/(NR*sinh(beta)*
cosh(beta)-NI*sin(alpha)*cos(alpha));
      Xopa=2*eta2/(cos(asin(2*Zop/(Xop*(eta1/eta2-eta2/eta1))))*(1-
eta2^2/eta1^2)+(1+eta2^2/eta1^2));
      fun=Xopa-Xop;
      theta=theta+0.0001*pi/180;
      % check if theta is greater than 90 deg
      if theta>91*pi/180
         theta=pi;   %indicating there is no solution for such thickness
         break
      end
   end
   ang(1,i)=theta*180/pi;

dielectric_thickness(1,i)=abs(lambda0/(4*pi*n1*cos(theta1))*asin(2*Zop/(Xop*(eta1/eta
2-eta2/eta1))))*1e9;
   %Step 4: find the second solution by repeating above process
   fun=5;          %initialize function value for iteration again
   Xopa=1i;         %initialize Xop value for iteration again
   theta=89.9999*pi/180;   %initialize incidence angle again
%    while theta~=ang(1,i)
      if abs(imag(Xopa))>1e-10
         while abs(imag(Xopa))>1e-10
            theta1=asin(n2*sin(theta)/n1);      %incidence angle in dielectric layer
            thetam=asin(n1*sin(theta1)/NAg);    %incidence angle in metal layer
            NM=NAg/cos(thetam);   %for TM
            NR=real(NM);
            NI=-imag(NM);
            eta2=n2/cos(theta);   %for TM
            eta1=n1/cos(theta1);  %for TM
            % Find Xop form general equation
            alpha=real((2*pi/lambda0)*NAg*dm*cos(thetam));
            beta=-imag((2*pi/lambda0)*NAg*dm*cos(thetam));

term1=(NR^2+NI^2)*(NR*sinh(beta)*cosh(beta)+NI*sin(alpha)*cos(alpha))/(NR*sinh(
beta)*cosh(beta)-NI*sin(alpha)*cos(alpha));

term2=(NR^2*NI^2)*((sin(alpha)^2*cosh(beta)^2+cos(alpha)^2*sinh(beta)^2)/(NR*sinh
(beta)*cosh(beta)-NI*sin(alpha)*cos(alpha)))^2;
            Xop=(term1-term2)^0.5;
```

```
Zop=(NR*NI)*(sin(alpha)^2*cosh(beta)^2+cos(alpha)^2*sinh(beta)^2)/(NR*sinh(beta)*
cosh(beta)-NI*sin(alpha)*cos(alpha));
            % Find Xop from impedence matchinig equation
            Xopa=2*eta2/(cos(asin(2*Zop/(Xop*(eta1/eta2-eta2/eta1))))*(1-
eta2^2/eta1^2)+(1+eta2^2/eta1^2));
            theta=theta-1*pi/180;
         end
         theta=theta+1*pi/180;
      end
      if abs(fun)>1
         while abs(fun)>1
            theta1=asin(n2*sin(theta)/n1);
            thetam=asin(n1*sin(theta1)/NAg);
            NM=NAg/cos(thetam);
            NR=real(NM);
            NI=-imag(NM);
            eta2=n2/cos(theta);
            eta1=n1/cos(theta1);
            alpha=real((2*pi/lambda0)*NAg*dm*cos(thetam));
            beta=-imag((2*pi/lambda0)*NAg*dm*cos(thetam));

term1=(NR^2+NI^2)*(NR*sinh(beta)*cosh(beta)+NI*sin(alpha)*cos(alpha))/(NR*sinh(
beta)*cosh(beta)-NI*sin(alpha)*cos(alpha));

term2=(NR^2*NI^2)*((sin(alpha)^2*cosh(beta)^2+cos(alpha)^2*sinh(beta)^2)/(NR*sinh
(beta)*cosh(beta)-NI*sin(alpha)*cos(alpha)))^2;
            Xop=(term1-term2)^0.5;

Zop=(NR*NI)*(sin(alpha)^2*cosh(beta)^2+cos(alpha)^2*sinh(beta)^2)/(NR*sinh(beta)*
cosh(beta)-NI*sin(alpha)*cos(alpha));
            Xopa=2*eta2/(cos(asin(2*Zop/(Xop*(eta1/eta2-eta2/eta1))))*(1-
eta2^2/eta1^2)+(1+eta2^2/eta1^2));
            fun=Xopa-Xop;
            theta=theta-0.01*pi/180;
         end
         theta=theta+0.01*pi/180;
      end
      while abs(fun)>0.0001
         theta1=asin(n2*sin(theta)/n1);
         thetam=asin(n1*sin(theta1)/NAg);
         NM=NAg/cos(thetam);
         NR=real(NM);
         NI=-imag(NM);
         eta2=n2/cos(theta);
         eta1=n1/cos(theta1);
         alpha=real((2*pi/lambda0)*NAg*dm*cos(thetam));
         beta=-imag((2*pi/lambda0)*NAg*dm*cos(thetam));
```

```
term1=(NR^2+NI^2)*(NR*sinh(beta)*cosh(beta)+NI*sin(alpha)*cos(alpha))/(NR*sinh(
beta)*cosh(beta)-NI*sin(alpha)*cos(alpha));

term2=(NR^2*NI^2)*((sin(alpha)^2*cosh(beta)^2+cos(alpha)^2*sinh(beta)^2)/(NR*sinh
(beta)*cosh(beta)-NI*sin(alpha)*cos(alpha)))^2;
        Xop=(term1-term2)^0.5;

Zop=(NR*NI)*(sin(alpha)^2*cosh(beta)^2+cos(alpha)^2*sinh(beta)^2)/(NR*sinh(beta)*
cosh(beta)-NI*sin(alpha)*cos(alpha));
        Xopa=2*eta2/(cos(asin(2*Zop/(Xop*(eta1/eta2-eta2/eta1))))*(1-
eta2^2/eta1^2)+(1+eta2^2/eta1^2));
        fun=Xopa-Xop;
        theta=theta-0.0001*pi/180;
        % check if theta is smaller than critical angle or first
        % solution
        if theta==ang(1,i)
           theta=pi;   %indicating there is no solution for such thickness
           break
        elseif theta<floor(asin(n1/n2))*pi/180
           theta=pi;   %indicating there is no solution for such thickness
           break
        end
     end
%    end
   ang(2,i)=theta*180/pi;

dielectric_thickness(2,i)=abs(lambda0/(4*pi*n1*cos(theta1))*asin(2*Zop/(Xop*(eta1/eta
2-eta2/eta1))))*1e9;
end
subplot(2,1,1)
hold on
plot(metal_thickness*1e9, ang(1,:),metal_thickness*1e9, ang(2,:))
xlabel('Ag layer thickness [nm]')
ylabel('Incidence angle for matching [deg]')
subplot(2,1,2)
hold on
plot(metal_thickness*1e9, dielectric_thickness(1,:),metal_thickness*1e9,
dielectric_thickness(2,:))
xlabel('Ag layer thickness [nm]')
ylabel('dielectric thickness for matching [nm]')
```

DMD Stack Simulation function file

```
function [Rte, Rtm, Tte, Ttm]=DMD_sim(lambda0, incidence_angle, nD, nM, n0, nSub)
thetain=(pi/180)*(incidence_angle); %Incidence angle
imp=376.8;  %Impedance of free space
AgOpCon;    %The Lorentz-Drude model for Ag optical constants from Rakic
```

```
%AgOpConPalik;    %The model for Ag optical constants from Pelik
%AgOpNanoHUB;%Ag optical constants from NanoHUB website
TiO2OpCon; %m-file that calculates the optical constants of TiO2
nSF11=sqrt(1.73759695.*(lambda0*1e6).^2./((lambda0*1e6).^2-
0.013188707)+0.313747346.*(lambda0*1e6).^2./((lambda0*1e6).^2-
0.0623068142)+1.89878101.*(lambda0*1e6).^2./((lambda0*1e6).^2-155.23629)+1);
nFS=sqrt(0.6961663.*(lambda0*1e6).^2./((lambda0*1e6).^2-
0.0684043^2)+0.4079426.*(lambda0*1e6).^2./((lambda0*1e6).^2-
0.1162414^2)+0.8974794.*(lambda0*1e6).^2./((lambda0*1e6).^2-9.896161^2)+1);
%nBK7=sqrt(1.28604141+1.07044083.*(lambda0*1e6).^2./((lambda0*1e6).^2-
1.00585997e-2)+1.10202242.*(lambda0*1e6).^2./((lambda0*1e6).^2-100));

% Get DMD structure from .txt file
R=textscan(fopen('DMD_Structure.txt'), '%f %f', 'headerLines', 4);
layerNumber=length(R{1,1});
layerT=R{1,2}*1e-9;

% Initiate inter-layer calculation matricies
n=zeros(layerNumber+2,1);   % refractive index matrix
ang=zeros(layerNumber,1);   % effective angle of plane wave
k=zeros(layerNumber,1);   %transverse phase thickness at current wavelength
yte=zeros(layerNumber,1);  %eff. admittance for TE
ytm=zeros(layerNumber,1);  %eff. admittance for TM

qL=length(lambda0);
for qt=1:length(thetain)
   angin=thetain(qt);
   for ql=1:qL
      lam0=lambda0(ql);
      k0=2*pi/lam0;

      % Check the refractive index of dielectric
      if strcmp(nD,'TiO2')==1
         nd=ntio2(ql);
      elseif strcmp(nD,'FS')==1
         nd=nFS(ql);
      elseif strcmp(nD,'BK7')==1
         nd=nBK7(ql);
      else nd=nD;
      end

      if nM=='Ag'
         nAg=nAgv(ql);
         kAg=kAgv(ql);
         %nAg=0.066;
         %kAg=4;
         NAg=nAg-1i*kAg;
      end
```

```
% Check the refractive index of substrate and ambience
if strcmp(n0,'SF11')==1
   nA=nSF11(ql);
elseif strcmp(n0,'FS')==1
   nA=nFS(ql);
else nA=n0;
end
if strcmp(nSub,'SF11')==1
   nS=nSF11(ql);
elseif strcmp(nSub,'BK7')==1
   nS=nBK7(ql);
elseif strcmp(nSub,'FS')==1
   nS=nFS(ql);
else nS=nSub;
end

% Set up index matrix for each layer of the the DMD structure
for i=1:2:layerNumber
   n(i+1)=nd;
   if i==1
      n(i)=nA;
   else n(i)=NAg;
   end
end

n(layerNumber+2)=nS;       %save substrate index into the last element
mte=[1 0;0 1];  %overall transfer matrix for the stack at current wavelength for TM
mtm=[1 0;0 1];  %overall transfer matrix for the stack at current wavelength for TM

%Hecht form transfer matrix calculation
for i=1:1:layerNumber
   %Intermediate layers of stack
   if i==1
      ang(i)=asin(sin(angin)*n(i)/n(i+1));
   else
      ang(i)=asin(sin(ang(i-1))*n(i)/n(i+1));
   end
   k(i)=n(i+1)*k0*cos(ang(i))*layerT(i);
   yte(i)=n(i+1)*cos(ang(i))/imp;
   ytm(i)=(cos(ang(i))*imp)/n(i+1);
   mlte=[cos(k(i)) 1i*sin(k(i))/yte(i); 1i*yte(i)*sin(k(i)) cos(k(i))];  %transfer matrix
for each type of layer at current wavelength for TE
   mltm=[cos(k(i)) 1i*sin(k(i))/ytm(i); 1i*ytm(i)*sin(k(i)) cos(k(i))];  %transfer
matrix for each type of layer at current wavelength for TM
   mte=mte*mlte;
   mtm=mtm*mltm;
end

%Substrate
```

```
        angS=asin(sin(ang(layerNumber))*n(layerNumber+1)/n(layerNumber+2));
%effective angle
        %effective admittance of input/exit media
        yote=n(1)*cos(angin)/imp;
        yotm=(cos(angin)*imp)/n(1);
        %effective admittance of substrate
        yste=n(layerNumber+2)*cos(angS)/imp;
        ystm=(cos(angS)*imp)/n(layerNumber+2);

        % calculate amplitude reflection and transmission coefficients at
        % current wavelength
        rte=(yote*mte(1,1)+yote*yste*mte(1,2)-mte(2,1)-
yste*mte(2,2))/(yote*mte(1,1)+yote*yste*mte(1,2)+mte(2,1)+yste*mte(2,2));
        rtm=(yotm*mtm(1,1)+yotm*ystm*mtm(1,2)-mtm(2,1)-
ystm*mtm(2,2))/(yotm*mtm(1,1)+yotm*ystm*mtm(1,2)+mtm(2,1)+ystm*mtm(2,2));
        tte=(2*yote)/(yote*mte(1,1)+yote*yste*mte(1,2)+mte(2,1)+yste*mte(2,2));
        ttm=(2*yotm)/(yotm*mtm(1,1)+yotm*ystm*mtm(1,2)+mtm(2,1)+ystm*mtm(2,2));
        % calculate and store reflectances at current
        % wavelength:
        Rte(qt,ql)=rte*conj(rte);
        Rtm(qt,ql)=rtm*conj(rtm);
        Tte(qt,ql)=tte*conj(tte)*nS*cos(angS)/(nA*cos(angin));
        Ttm(qt,ql)=ttm*conj(ttm)*nA*cos(angS)/(nS*cos(angin));
    end
end
```

DMD Stack Simulation structure file

```
This file includes the DMD layer structure specifications, the
number of layers, and the thickness of each layer

layer number      layer thickness
1                   50
2                   30
3                   50
```

DMD Stack Simulation executing file

```
% This file uses the following parameters to do a
% dielectric-metal-dielectric (DMD) simulation and plot the results

clear all
%Function input
lambda0=300e-9:1e-9:800e-9; %Free-space wavelengths
%lambda0=632.8e-9; %Free-space wavelengths
%incidence_angle=0:0.1:89;      %Incidence angle in deg
incidence_angle=81.52;      %Incidence angle in deg
```

```
nD='TiO2';   %dielectric layer close to ambience chemical name/index
%nD='BK7';   %SiO2 is BK7 type
%nD='FS';    %SiO2 is fused silica type
%nD=2.35;
nM='Ag';     %metal layer chemical name/index
n0='FS';        %Ambient input/output index (air/prism)
%n0='SF11';
%n0=1.5;
%nSub='SF11';    %sample substrate index
%nSub='FS';
%nSub=1;
nSub=n0;

%Main function calculates the simulation
[Rte, Rtm, Tte, Ttm]=DMD_sim(lambda0, incidence_angle, nD, nM, n0, nSub);

%Results generation
%if the lambda0 is a number and the angle is a vector
if length(lambda0)==1 && length(incidence_angle)>1
   %
plot(incidence_angle,abs(Ttm(:,1)),'b',incidence_angle,abs(Rtm(:,1)),'g',incidence_angle,
abs(Tte(:,1)),'r:', incidence_angle,abs(Rte(:,1)),'y:')
   %     legend('Ttm','Rtm','Tte','Rte')
   %    plot(incidence_angle,abs(Ttm(:,1)),'b',incidence_angle,abs(Rtm(:,1)),'g')
   %    legend('Ttm','Rtm')
   plot(incidence_angle,abs(Ttm(:,1)),'b')
   xlabel('Incidence angle [deg]')
   ylabel('Transmittance [TM]')
   %ylabel('Reflectance [TM]')
   %title(['wavelength is ', num2str(lambda0*1e9), ' in [nm]'])
   axis([incidence_angle(1) incidence_angle(length(incidence_angle)) 0 1])
%axis([xmin xmax ymin ymax])
end
%if the angle is a number and lambda0 is a vector
if length(incidence_angle)==1 && length(lambda0)>1
   %
plot(lambda0*10^9,abs(Ttm(1,:)),'b',lambda0*10^9,abs(Rtm(1,:)),'g',lambda0*10^9,abs(
Tte(1,:)),'r:', lambda0*10^9,abs(Rte(1,:)),'y:')
   %     legend('Ttm','Rtm','Tte', 'Rte')
   %    plot(lambda0*10^9,abs(Tte(1,:)),'r')
   plot(lambda0*10^9,abs(Tte(1,:)),'b')
   xlabel('Wavelength [nm]')
   ylabel('Transmittance [TE]')
   %title(['Incidence angle is ', num2str(incidence_angle), ' in [deg]'])
   axis([lambda0(1)*1e9 lambda0(length(lambda0))*1e9 0 1])    %axis([xmin xmax ymin
ymax])
end
%if the angle is a vector and lambda0 is a vector (3D plot)
```

```
if length(incidence_angle)>1 && length(lambda0)>1
%    subplot(2,2,1)
    mesh(incidence_angle,lambda0*1e9,abs(Ttm)');view(0,90),grid('on'),axis('tight')
    xlabel('wavelength [nm]'),ylabel('incidence angle [deg]'),zlabel('Ttm')
%     subplot(2,2,2)
%     mesh(lambda0*1e9,incidence_angle,abs(Rtm));view(3),grid('on'),axis('tight')
%     xlabel('wavelength [nm]'),ylabel('incidence angle [deg]'),zlabel('Rtm')
%     subplot(2,2,3)
%     mesh(lambda0*1e9,incidence_angle,abs(Tte));view(3),grid('on'),axis('tight')
%     xlabel('wavelength [nm]'),ylabel('incidence angle [deg]'),zlabel('Tte')
%     subplot(2,2,4)
%     mesh(lambda0*1e9,incidence_angle,abs(Rte));view(3),grid('on'),axis('tight')
%     xlabel('wavelength [nm]'),ylabel('incidence angle [deg]'),zlabel('Rte')
    [index_wavelength index_angle max_value]=find_max(Ttm, lambda0)
end
%if the angle is a number and lambda0 is a number
if length(incidence_angle)==1 && length(lambda0)==1
    Rte, Rtm, Tte, Ttm
    close
    error(sprintf('At least one of the incidence_angle or lambda0 has to be vector'));
end

hold on
%Compare with normalized experiment result
R=textscan(fopen('C:\Users\Carson\Dropbox\Grad\Sample data\Normalized
data\160812\Marked TE light scan with prism\0 deg.txt'), '%f %f');
wavelength_data=R{1,1};
T_data=R{1,2};
plot(wavelength_data(51:251),T_data(51:251),'g')
legend('simulation', 'normalized experiment')
hold off

% % Export to a txt file
% Export_file_name='C:\Users\Carson\Dropbox\Grad\Sample data\Simulated
data\260912 Nonmarked SF11 prism couple\80 deg.txt';
% fid = fopen(Export_file_name, 'w');  % open a file for writing
% % print values in column order
% % two values appear on each row of the file
% y=[lambda0*10^9; abs(Ttm(1,:))];
% fprintf(fid, '%f  %f\n', y);
% fclose(fid);
```